

# Production of Omega and Xi hyperons in proton-proton collisions at $\sqrt{s} = 13$ TeV using the ALICE detector at the Large Hadron Collider

---

Karatović, David

Doctoral thesis / Doktorski rad

2024

Degree Grantor / Ustanova koja je dodijelila akademski / stručni stupanj: **University of Zagreb, Faculty of Science / Sveučilište u Zagrebu, Prirodoslovno-matematički fakultet**

Permanent link / Trajna poveznica: <https://um.nsk.hr/um:nbn:hr:217:532859>

Rights / Prava: [In copyright](#) / [Zaštićeno autorskim pravom.](#)

Download date / Datum preuzimanja: **2025-03-25**



Repository / Repozitorij:

[Repository of the Faculty of Science - University of Zagreb](#)





University of Zagreb  
Faculty of Science  
Department of Physics

David Karatović

**Production of Omega and Xi hyperons in  
proton-proton collisions at  $\sqrt{s} = 13$  TeV  
using the ALICE detector at the Large  
Hadron Collider**

DOCTORAL THESIS

Zagreb, 2024





University of Zagreb  
Faculty of Science  
Department of Physics

David Karatović

**Production of Omega and Xi hyperons in  
proton-proton collisions at  $\sqrt{s} = 13$  TeV  
using the ALICE detector at the Large  
Hadron Collider**

DOCTORAL THESIS

Supervisor:  
prof. Mirko Planinić

Zagreb, 2024



Sveučilište u Zagrebu  
Prirodoslovno-matematički fakultet  
Fizički odsjek

David Karatović

**Proizvodnja Omega i Ksi hiperona u  
sudarima protona pri  $\sqrt{s} = 13$  TeV-a  
proučavana pomoću detektora ALICE na  
Velikom Hadronskom Sudarivaču**

DOKTORSKI RAD

Mentor:  
prof. dr. sc. Mirko Planinić

Zagreb, 2024

# Acknowledgements

I extend my gratitude to all individuals at CERN who contributed significantly to my PhD research. I am particularly thankful to Livio, David, Lee, Marek, Chiara, and Nicolo for their invaluable guidance and insightful comments throughout my analysis. Their expertise and encouragement were instrumental in shaping this thesis.

Zahvaljujem se svom mentoru prof. Mirku Planiniću na prilici da se priključim njegovoj grupi i izradim ovaj doktorski rad. Uz njegovo mentorstvo sam stekao ogromno iskustvo, stekao nova poznanstva i prijateljstva, i napredovao koliko profesionalno, toliko i osobno.

Zahvalio bih se radnim kolegama Blažu, Filipu, Marku, Antoniji i Nini, koji su kroz razgovore i druženja učinili rad na ovom doktoratu puno ugodnijim. Posebno bih se zahvalio Nikoli na beskonačnoj pomoći koja se ne može sažeti u sklopu ovih zahvala.

Konačno, zahvalio bih se svojoj obitelji i prijateljima na svoj pruženoj ljubavi i podršci. Najviše se želim zahvaliti svojoj ženi Magdaleni, kojoj ujedno i posvećujem ovaj rad.

# Abstract

Investigation of the production of strange particles in high-energy collisions is one of the ways to study quark-gluon plasma (QGP). One of the first suggested signatures of QGP was the phenomenon of strangeness enhancement. It was long considered that it is only possible to have QGP in heavy ion collisions, and that the proton-proton system is too small to produce QGP. After strangeness enhancement was observed in heavy ion collisions, with an increase in collision energy at the LHC, it was also observed in proton-proton collisions, in which we didn't expect to find quark-gluon plasma, together with some of the other QGP signatures. With higher LHC energies, the question arises: will the production of strangeness continue with a growing trend, as it does for other systems, or will saturation occur for smaller systems, as it does in lead-lead collisions?

This study analyses data collected by the ALICE detector at the LHC from 2016-2018 during 13 TeV proton-proton collisions. The analysis investigates the dependence of Xi and Omega hyperon yields on their transverse impulse, as well as on the multiplicity of collisions. The main analysis is done on highest multiplicity events. This fills a gap in multiplicity in which there are currently few results available for collisions of protons. The data used is comparable to data from proton-lead and peripheral lead-lead collisions and the aim is to see if the results agree, or if there is a saturation in strangeness production in pp collisions. As a consequence, certain models that try to explain strangeness enhancement would be either confirmed or disproved.

The results show great agreement with results from collisions of other systems, namely lead-lead and proton-lead, and different collision energies. This confirms that strangeness enhancement is present in high multiplicity proton-proton collisions. The number of produced strange particles in the final state of the collision depends on the final multiplicity of the collision, and not on the energy or the type of particles colliding.

**Keywords:** Quark-gluon plasma, strangeness enhancement, strange quark, hyperon, Xi, Omega, proton-proton collision, high multiplicity, ALICE detector

# Sažetak

Istraživanje proizvodnje stranih čestica pri visokoenergetskim sudarima jedan je od načina proučavanja kvarkovsko-gluonske plazme. Jedan od prvih potpisa kvarkovsko-gluonske plazme je bio fenomen povećanja stranosti. Dugo vremena je znanstveni konsenzus bio da je kvarkovsko-gluonsku plazmu moguće stvoriti samo u sudarima teških iona, jer je sustav u sudarima protona premalen. Nakon što je povećanje stranosti primijećeno u sudarima teških iona, povećanjem energije sudara na LHC-u primijetilo se i u proton-proton sudarima, u kojima nismo očekivali postojanje kvarkovsko-gluonske plazme. Sa sve većim energijama sudara na LHC-u postavlja se pitanje: hoće li se trend povećanja stranosti nastaviti kao za druge sustave, ili će doći do zasićenja u sustavu protona kao što se dogodi u sudarima teških iona?

U ovom istraživanju analiziraju se podaci prikupljeni ALICE detektorom na LHC-u 2016.-2018. u sudarima protona na energijama centra mase 13 TeV-a. U analizi se određuje ovisnost broja proizvedenih Ksi i Omega hiperona o njihovu transverzalnom impulsu, kao i o multiplicitetu sudara. Glavna tema istraživanja je područje najvišeg multipliciteta. Time se popunjuje područje u kojem za protone trenutno ima malo dostupnih rezultata. Ono je usporedivo s podacima iz perifernih Pb-Pb sudara te je cilj vidjeti slažu li se rezultati međusobno ili dolazi do zasićenja proizvodnje stranosti u proton-proton sudarima. Iz toga bi se potvrdili ili opovrgnuli određeni modeli koji pokušavaju objasniti povećanu proizvodnju stranih čestica.

Rezultati su u odličnom slaganju s rezultatima dobivenim iz drugih tipova sudara, sudara proton-olovo i olovo-olovo, pri različitim energijama. Time je potvrđeno postojanje povećanja stranosti u sudarima protona pri najvišim multiplicitetima. Broj proizvedenih čestica ovisi samo o konačnom multiplicitetu sudara, a ne o energiji i tipu čestica koje sudaramo.

**Ključne riječi:** kvarkovsko-gluonska plazma, povećanje stranosti, strani kvark, hiperon, Ksi, Omega, proton-proton sudari, visoki multiplicitet, ALICE detektor

# Contents

<b>1</b>	<b>Introduction</b>	<b>1</b>
1.1	The Standard Model . . . . .	3
1.2	Quantum Chromodynamics . . . . .	5
1.3	The quark-gluon plasma . . . . .	8
1.3.1	Signatures of QGP . . . . .	10
1.4	High energy collisions . . . . .	13
<b>2</b>	<b>Physics of strangeness</b>	<b>16</b>
2.1	Hyperons . . . . .	17
2.2	Strangeness production . . . . .	19
2.2.1	Strangeness production in hadron gas . . . . .	20
2.2.2	Strangeness production in QGP . . . . .	21
2.3	Strangeness enhancement . . . . .	22
<b>3</b>	<b>Experiment</b>	<b>27</b>
3.1	The Large Hadron Collider . . . . .	28
3.1.1	The CERN accelerator complex . . . . .	30
3.1.2	Magnets . . . . .	32
3.1.3	Radiofrequency cavities . . . . .	33
3.1.4	Cryogenics . . . . .	34
3.1.5	Vacuum systems . . . . .	34
3.2	A Large Ion Collider Experiment . . . . .	35
3.2.1	Barrel detectors . . . . .	36
3.2.2	Particle Identification . . . . .	39
3.2.3	Calorimeters . . . . .	40
3.2.4	Forward detectors . . . . .	42
3.2.5	ALICE Cosmic Rays Detector (ACORDE) . . . . .	44
3.3	ALICE online systems . . . . .	44
3.4	ALICE offline software . . . . .	46
3.4.1	Grid . . . . .	46
3.4.2	AliRoot . . . . .	46
3.4.3	Reconstruction of events . . . . .	47

<b>4</b>	<b>Methodology</b>	<b>50</b>
4.1	Data selection . . . . .	51
4.1.1	Data and MC samples . . . . .	51
4.1.2	Event selection . . . . .	52
4.1.3	Multiplicity selection . . . . .	52
4.2	Cascade reconstruction . . . . .	53
4.2.1	Track selections . . . . .	54
4.2.2	Topological selections . . . . .	55
4.2.3	Candidate selections . . . . .	59
4.3	Analysis details . . . . .	60
4.3.1	Analysis cuts . . . . .	60
4.3.2	Signal extraction . . . . .	60
4.3.3	Acceptance x efficiency . . . . .	65
4.4	Comparison to the published results . . . . .	67
4.5	Systematic uncertainties . . . . .	69
4.5.1	Cut variations . . . . .	69
4.5.2	Signal extraction uncertainty . . . . .	79
<b>5</b>	<b>Results</b>	<b>80</b>
5.1	Corrected $p_T$ spectra . . . . .	81
5.2	Spectra fitting . . . . .	83
5.2.1	Total yield uncertainty . . . . .	85
5.3	Integrated yields . . . . .	87
5.4	The average transverse momentum . . . . .	89
5.5	$\Omega$ to $\Xi$ ratios . . . . .	90
5.6	Ratio to pions . . . . .	92
<b>6</b>	<b>Conclusion</b>	<b>94</b>
	<b>Prošireni sažetak</b>	<b>96</b>
	<b>References</b>	<b>110</b>
	<b>Supervisor information</b>	<b>114</b>
	<b>Curriculum vitae</b>	<b>115</b>

# List of Figures

1.1	Elementary particles of the Standard model. [3]	4
1.2	Summary of measurements of $\alpha_s$ as a function of the energy scale $Q$ . The respective degree of QCD perturbation theory used in the extraction of $\alpha_s$ is indicated in brackets (NLO: next-to-leading order; NNLO: next-to-next-to-leading order; NNLO+res.: NNLO matched to a resummed calculation; N <sup>3</sup> LO: next-to-NNLO). [13].	7
1.3	A simplified phase diagram of the nuclear phase transition from regular hadronic matter to the QGP phase. The anti-colours in mesons are shown by using (near) complementary colours ( $\bar{r}$ = cyan, $\bar{b}$ = yellow, $\bar{g}$ = purple). [14]	8
1.4	The Bjorken scenario foreseen for the collision of ultra-relativistic heavy ions. [16]	9
1.5	Phase diagram (temperature, net baryon density) of QCD matter, ranging from regular nuclear matter to Quark-Gluon Plasma. [17]	11
1.6	A schematic view of a heavy-ion collision. The impact parameter $b$ is shown as well as the spectator nucleons and the participant nucleons. [19]	14
1.7	The evolution of the collision of ultra-relativistic heavy ions. [16]	15
2.1	Combinations of light flavoured quarks forming baryons with a spin - 1/2 form the $uds$ baryon octet. [23]	17
2.2	Combinations of light flavoured quarks forming baryons with a spin - 3/2 form the $uds$ baryon decuplet. [23]	18
2.3	Examples of decay chains for some typically produced hyperons. The percentages next to the vertices represent the branching ratios of associated channels. [24]	20
2.4	Feynmann diagrams for $s\bar{s}$ production in QGP.	22
2.5	Simple visualization of $\Xi^-$ and $\bar{\Omega}^+$ hadronization from QGP.	23
2.6	$p_T$ -integrated yield ratios to pions as a function of multiplicity ( $dN_{ch}/d\eta$ ) measured in $ \eta  < 0.5$ . The values are compared to calculations from MC models and to results obtained in p-Pb and Pb-Pb collisions at the LHC. [2]	25
2.7	Particle yield ratios to pions normalized to the values measured in the inclusive INEL $> 0$ pp sample. [2]	26
3.1	Overall view of the LHC, including the ALICE, ATLAS, CMS and LHCb experiments. [39]	29



3.2	A graphic overview of all accelerators in operation at CERN during Run 2. [40]	31
3.3	Cross section of the LHC Main Dipole in its cryostat. [41]	33
3.4	Schematics of ALICE during Run 2. [42]	35
3.5	ITS schematics during Run 2. [42]	37
3.6	Illustration of one TPC readout segment. [44]	38
3.7	Illustration of different types of calorimeters and particles passing through them. [45]	41
3.8	Schematic view of ALICE data flow. [47]	45
3.9	Principles of tracking for an ALICE event using Kalman filter approach. [48]	49
4.1	The topology of the cascade decay for cascades and their antiparticles along with successive decays. [50]	54
4.2	Illustrations of topological selections used to reconstruct $\Xi^-$ . V0 daughters selection is shown in 1.a)-d), while the selections relevant to cascade are shown in 2.a)-d). [53]	57
4.3	Illustration of a $\Lambda$ decay with a pion passing close to a proton, which could result in misidentifying it as $\Xi$ . [49]	58
4.4	$\Omega$ invariant mass plots for MB data fitted with a Gaussian plus linear function.	63
4.5	$\Xi$ invariant mass plots for MB data fitted with a Gaussian plus linear function.	63
4.6	$\Omega$ invariant mass plots for HM data fitted with a Gaussian plus linear function.	64
4.7	$\Xi$ invariant mass plots for HM data fitted with a Gaussian plus linear function.	64
4.8	Acceptance times efficiency corrections as a function of multiplicity for $\Omega$ (left) and $\Xi$ (right) for the MB sample (rainbow) and the HM int. multiplicity sample (black). The ratio on the bottom panels is done wrt. integrated MB efficiency.	65
4.9	Ratio of $\Omega$ MB corrected $p_T$ spectra to the published results.	67
4.10	Ratio of $\Xi$ MB corrected $p_T$ spectra to the published results.	68
4.11	Signal loss with cut variation for $\Omega$ .	72
4.12	Signal loss with cut variation for $\Xi$ .	73
4.13	Ratio of $p_T$ spectra wrt. the default one for $\Omega$ .	74
4.14	Ratio of $p_T$ spectra wrt. the default one for $\Xi$ .	75
4.15	Maximum deviation for $\Omega$ .	76
4.16	Maximum deviation for $\Xi$ .	77
4.17	Total systematic uncertainty for $\Omega$ (blue line). The red line is the contribution from cut variation, the green line is the contribution from material budget and the yellow line the contribution from signal extraction. Pile-up (2 %) and int. multiplicity uncertainty (2 %) is not shown but is added to the total.	78
4.18	Maximum deviation for $\Xi$ . The red line is the contribution from cut variation, the green line is the contribution from material budget and the yellow line the contribution from signal extraction. Pile-up (2 %) and int. multiplicity uncertainty (2 %) is not shown but is added to the total.	78
4.19	Contribution to the systematic uncertainty from using different background fits.	79

5.1	$\Omega^- + \bar{\Omega}^+$ and $\Xi^- + \bar{\Xi}^+$ corrected $p_T$ spectra for different V0M multiplicity classes for HM (blue palette) and MB (rainbow palette). In the bottom panel, the ratios with respect to the integrated multiplicity case are shown. Only the statistical errors are shown. . . . .	82
5.2	$\Omega^- + \bar{\Omega}^+$ (left) and $\Xi^- + \bar{\Xi}^+$ (right) $\chi^2/ndf$ values for different multiplicity classes for the Levy-Tsallis fit. . . . .	83
5.3	$\Omega^- + \bar{\Omega}^+$ (left) and $\Xi^- + \bar{\Xi}^+$ (right) corrected $p_T$ spectra fitted with a Levy-Tsallis distribution. In the bottom panel the ratios of the measured spectra to the fitting function are shown. The error bars are statistical and the error boxes are systematic uncertainties. . . . .	84
5.4	Total relative systematic error for integrated yields of $\Omega$ (left) and $\Xi$ (right) for different multiplicity classes. . . . .	85
5.5	$\Omega^- + \bar{\Omega}^+$ (top) and $\Xi^- + \bar{\Xi}^+$ (bottom) spectra fitted with different fitting functions. The bottom panels show the ratio of spectra with respect to integrated multiplicity. The boxes represent the systematic uncertainties. . . . .	86
5.6	$\Omega^- + \bar{\Omega}^+$ (left) and $\Xi^- + \bar{\Xi}^+$ (right) integrated yields as a function of multiplicity. The black points are the three HM classes and the pink point is the integrated multiplicity. A 2nd degree polynomial is fitted to the results. The boxes represent the total systematic errors. . . . .	87
5.7	$\Omega^- + \bar{\Omega}^+$ (up) and $\Xi^- + \bar{\Xi}^+$ (down) normalized $p_T$ -integrated yields as a function of multiplicity for pp, pPb and PbPb. . . . .	88
5.8	$\Omega^- + \bar{\Omega}^+$ (left) and $\Xi^- + \bar{\Xi}^+$ (right) mean $p_T$ as a function of multiplicity. The black points are the three HM classes and the pink point is the integrated multiplicity. The boxes represent the total systematic uncertainties. . . . .	89
5.9	$\Omega$ and $\Xi$ ratio for different multiplicity classes: MB (left), HM (right) and both (bottom). . . . .	90
5.10	$\Omega$ and $\Xi$ ratio of integrated yields. . . . .	91
5.11	Integrated hadron-to-pion ratios as a function of multiplicity measured in pp, p-Pb, and Pb-Pb collisions at energies of 13 TeV and 5.02 TeV. The boxes represent the systematic uncertainties. . . . .	92
5.12	Ratio of $\Xi$ and $\Omega$ yields with pion yields for different systems, including Run I pp and PbPb data. . . . .	93
7.1	Pojednostavljeni prikaz prelaska obične hadronske materije u kvarkovsko-gluonsku plazmu. [14] . . . . .	97
7.2	Feynmannovi dijagrami koje prikazuju stvaranje $s\bar{s}$ parova. . . . .	98
7.3	Pojednostavljena vizualizacija stvaranja $\Xi^-$ i $\bar{\Omega}^+$ hiperona hadronizacijom iz QGP-a. . . . .	98
7.4	Omjer broja proizvedenih hiperona i broja proizvedenih nabijenih piona u ovisnosti u multiplicitetu ( $dN_{ch}/d\eta$ ) mjereni u području $ \eta  < 0.5$ . [2] . . . . .	99
7.5	Omjer proizvedenih hiperona i piona normaliziran na INEL $> 0$ slučaj. [2] . . . . .	100
7.6	Shematski prikaz ALICE detektora za vrijeme trajanja Run II. [42] . . . . .	101

7.7	Ovisnost broja proizvedenih $\Omega^- + \bar{\Omega}^+$ i $\Xi^- + \bar{\Xi}^+$ o transversalnoj količini gibanja $\Omega^- + \bar{\Omega}^+$ i $\Xi^- + \bar{\Xi}^+$ za različite multiplicitete. Na donjim grafovima su prikazani omjeri naspram integriranog multipliciteta (0-100%). Na slikama su prikazane statističke greške. . . . .	103
7.8	Spektri transversalne količine gibanja za $\Omega^- + \bar{\Omega}^+$ i $\Xi^- + \bar{\Xi}^+$ s prilagođenim Levy-Tsallis distribucijama. U donjim grafovima je omjer prilagođene funkcije i podataka. Statističke greške su prikazane linijama dok su sistematske greške prikazane pravokutnicima. . . . .	104
7.9	Integrirani broj proizvedenih hiperona $\Omega^- + \bar{\Omega}^+$ i $\Xi^- + \bar{\Xi}^+$ u ovisnosti o multiplicitetu. Pravokutnici predstavljaju sistematske greške dok su statističke prikazane linijama. . . . .	104
7.10	Integrirani broj proizvedenih hiperona $\Omega^- + \bar{\Omega}^+$ i $\Xi^- + \bar{\Xi}^+$ u ovisnosti o multiplicitetu za različite sustave: pp, pPb and PbPb. . . . .	105
7.11	Prosječna transversalna količina gibanja za $\Omega^- + \bar{\Omega}^+$ i $\Xi^- + \bar{\Xi}^+$ . Pravokutnici su sistematske greške. . . . .	105
7.12	Omjer spektara transversalnih količina gibanja za $\Omega$ i $\Xi$ (gore) za različite vrijednosti multipliciteta. Omjer integriranog broja proizvedenih čestica za $\Omega$ i $\Xi$ (dolje) u ovisnosti o multiplicitetu. . . . .	106
7.13	Omjer proizvedenih $\Xi$ i $\Omega$ naspram piona za različite tipove sudara. . . . .	107

# List of Tables

2.1	Table of hyperons with their measured rest mass, mean lifetime and most common decay modes. [13]	19
4.1	Multiplicity classes used for each particle in MB analysis.	53
4.2	Multiplicity classes used for each particle in HM analysis.	53
4.3	Track, topological and candidate selection criteria applied to charged $\Xi$ and $\Omega$ candidates.	61
4.4	$p_T$ bins used for each particle in MB analysis.	62
4.5	$p_T$ bins used for each particle in HM analysis.	62
4.6	Values of the selection cuts chosen for systematics estimation in the HM $\Omega$ analysis.	70
4.7	Values of the selection cuts chosen for systematics estimation in the HM $\Xi$ analysis.	71
5.1	Integrated yields with final statistical and total systematic errors.	87

# Chapter 1

## Introduction

The incredible fact that all matter in the known Universe is composed of only twelve elementary particles has been known for years. When we add to that that most of this matter is made of only three elementary particles, electrons, up and down quarks, the Universe should apparently be very easy to describe. Unfortunately, that is not the case.

The theory with which we describe these basic constituents of matter and most of their interactions is known as the Standard Model of particle physics (SM). Although the validity of the SM has been confirmed through many experiments, it is still incomplete. It does not include the gravitational interaction, which we currently describe with Einstein's general theory of relativity, and it does not offer an explanation for several phenomena, such as the accelerated expansion of the Universe, neutrino oscillations, etc. As such, scientists around the world are testing the theory and searching for new insights to improve it and deepen our understanding of how the Universe works.

To experimentally test the SM we use large accelerators that are capable of producing high energy collisions. In these collisions, an interesting state of matter can be produced, called the quark-gluon plasma (QGP), and we get a glimpse of what happened right after the Big Bang. In the QGP quarks and gluons are in a deconfined state which enables the study of their properties and leads to a better understanding of the force binding quarks into hadrons (the strong force). Understanding the properties of this plasma is key to understanding the behavior of matter in extreme conditions, so it is one of the main topics of research in particle physics. To be able to study QGP, we need to know how to spot it first. When QGP is produced in collisions, phenomena can be observed that would not normally occur. These phenomena are called QGP signatures. Some of the signatures of QGP are the ridge structure, jet suppression, suppression of heavy quarkonia, etc. As increasing collision energies are achieved at the LHC, it has been observed that most of these QGP signatures are also seen in the most central proton-proton (pp)

collisions.

One of the QGP signatures, which is the main topic of this research, is strangeness enhancement, which was recently observed in pp collisions at energy of 13 TeV. Strangeness enhancement was first observed in heavy ion collisions, but with an increase in proton collision energies and thus an increase in multiplicity (number of produced particles), it was noticed that in high multiplicity pp collisions there is an increase in hadron production containing strange quarks. [1]

At energies of 13 TeV in proton-proton collisions at the Large Hadron Collider (LHC), high multiplicity events become comparable to those in peripheral heavy-ion collisions. Thus, we can observe the trend of the production of strange hadrons from low-multiplicity pp collisions to central lead-lead collisions. The results show a growing trend until saturation occurs at very high multiplicities in more central lead-lead collisions. It has also been shown in [2], that the phenomenon of strangeness enhancement is more pronounced the more strange quarks a hadron contains. This means that increasing the multiplicity of events will increase the relative number of Omega hyperons formed (Omega has 3 strange quarks) versus the increase in the number of Xi hyperons (Xi has 2 strange quarks). The production of strange hadrons (number of strange hadrons per unit of pseudorapidity<sup>1</sup>) at different proton-proton, proton-lead and lead-lead (pp, p-Pb and Pb-Pb) collision energies gives similar results at equal multiplicities, which leads to the conclusion that the production of strange hadrons does not depend on the initial system or the energy of the collision itself but only on the final state of the system. In this study, the analysis will be done only for Xi's and Omega's where there is least processed data, because these are the heaviest hyperons and are therefore produced in smallest numbers.

As it can be seen in this brief introduction, the study and testing of the SM is extremely financially and time-consuming, but you cannot put a price on the human desire for knowledge. This is just one small part of the collective effort to understand how the world works.

This thesis is divided into six chapters. This chapter contains a description of the Standard Model and Quantum Chromodynamics. The second chapter contains a theoretical overview of strangeness production and strangeness enhancement. The experimental setup consisting of the LHC and the ALICE detector is described in Chapter 3. An overview of the analysis details is in the Chapter 4. The results are presented in Chapter 5. Finally, the conclusion of this thesis is presented in Chapter 6.

---

<sup>1</sup>Pseudorapidity describes the angle of a particles trajectory to the beam axis.

## 1.1 The Standard Model

The Standard Model is a theoretical framework in particle physics that describes the fundamental building blocks of matter and the fundamental forces that govern their interactions. The development of this model was a collective effort by many scientists around the world throughout the second half of the 20th century. Its final formulation was achieved in the mid-1970s after experimental confirmation of the existence of quarks. It is based on the idea that all matter is composed of elementary particles, which are the smallest units of matter that cannot be broken down any further. The SM incorporates three of the four fundamental forces of nature - the electromagnetic, weak, and strong nuclear forces - into a single unified theory. The fourth force, gravity, is not included in the Standard Model, and is described by Einstein's theory of General Relativity.

The elementary particles in the Standard Model are divided into two categories - fermions and bosons. Fermions are the building blocks of matter and include quarks and leptons, while bosons are the force carriers. There are a total of twelve fermions, six of them are quarks and six are leptons, and they have a spin of  $1/2$ . Quarks are particles that combine to form protons and neutrons, which make up the nucleus of an atom. The six types of quarks are up ( $u$ ), down ( $d$ ), charm ( $c$ ), strange ( $s$ ), top ( $t$ ), and bottom ( $b$ ), and each one has a different mass and charge. Leptons are particles that do not interact through the strong nuclear force and include electrons ( $e$ ), muons ( $\mu$ ), and tau ( $\tau$ ) leptons, as well as their corresponding neutrinos, electron neutrino ( $\nu_e$ ), muon neutrino ( $\nu_\mu$ ) and tau neutrino ( $\nu_\tau$ ). The SM also provides for the existence of the antimatter counterparts of all mentioned particles, which have the same properties except the opposite charge (electrical charge, weak charge, color charge etc.).

The pairs of quarks and leptons are grouped into three different generations exhibiting similar behavior (Figure 1.1). Each member of a generation has greater mass than the corresponding particle from lower generations. Only the particles of the first generation are stable, therefore all ordinary (baryonic) matter is made out of them. Specifically, all atoms consist of electrons orbiting an atomic nucleus, ultimately made up of up and down quarks. Second and third generation decays have very short half-lives and are observed only in extreme environments (high energy environments).

The interactions between elementary particles are described by the exchange of gauge bosons or equivalently, by a field. The three fundamental forces (fields) are each mediated by corresponding bosons. The electromagnetic force is carried by the photon, the weak nuclear force is carried by the weak bosons, and the strong nuclear force is carried by gluons. All of these bosons have a spin equal to one and are also known as vector bosons.

The models that describe these interactions are:

**Quantum Electrodynamics (QED)** describes the electromagnetic interaction between electrically charged particles. It was developed between 1946 and 1950 by Tomonaga Shinichiro, Julian S. Schwinger and Richard P. Feynman, and it was awarded the Nobel Prize in 1965 [4]. It is a field theory with  $U(1)$  gauge symmetry that causes the existence of a massless neutral gauge boson called a photon. Electrically charged particles interact by exchanging virtual photons and only neutrinos do not interact via the electromagnetic interaction.

**Electroweak interaction (EW)** is the unified description of two fundamental interactions: electromagnetism and the weak interaction. Sheldon Lee Glashow first experimented with introducing two different symmetries, and the theory was completed in 1967 by Abdus Salam and Steven Weinberg. All together, they received the Nobel Prize in 1979 [5]. A first measurement of the interaction bosons  $W^+$ ,  $W^-$  and  $Z^0$  was made in 1983, when these were directly observed in the collisions of the SppS at CERN. The following year, this experimental work won the Nobel Prize for Carlo Rubbia and Simon van der Meer [6]. The theory has a  $SU(2) \times U(1)$  gauge symmetry, so it has four gauge bosons: the  $W^\pm$  and the  $Z$  bosons, for the weak interaction, and the already mentioned photon for the electromagnetic interaction.

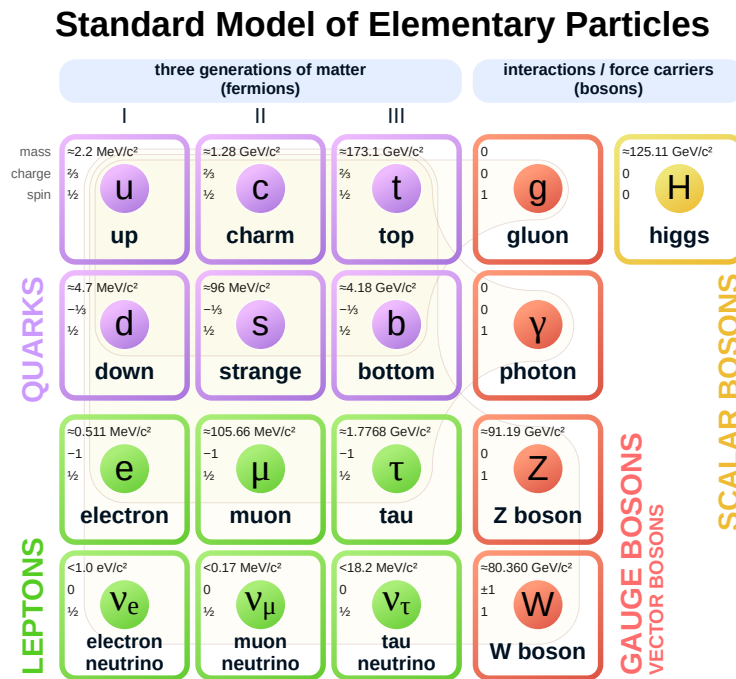


Figure 1.1: Elementary particles of the Standard model. [3]



**Quantum Chromodynamics (QCD)** describes the strong interaction between quarks and gluons, which make up the hadrons. In 1964, Murray Gell-Mann [7] and George Zweig [8] independently proposed the quark model, which suggested that protons, neutrons, and mesons were all made up of particles called quarks. QCD was developed by a number of physicists, including David Gross, Frank Wilczek, and H. David Politzer, who were awarded the Nobel Prize in Physics in 2004 for their contributions to the theory [9]. The theory has  $SU(3)$  symmetry and has 8 gauge bosons. It will be discussed in more detail in the next chapter.

One of the most important particles in the SM is the Higgs boson, which was discovered at the LHC in 2012 [10]. The Higgs boson is responsible for giving mass to all elementary particles. Without the Higgs boson, all elementary particles would be massless, and the Universe as we know it would not exist. The Higgs boson is a scalar boson because its spin equals zero.

The Standard Model has been tested and verified through numerous experiments, including those conducted at the LHC. It has successfully predicted the existence and behavior of many particles and interactions that were later discovered experimentally. However, the SM is not a complete theory of the Universe. It does not account for several phenomena, such as dark matter and dark energy, which make up a large portion of the Universe. Therefore, physicists continue to search for a more complete theory that can fully explain the fundamental nature of the Universe.

## 1.2 Quantum Chromodynamics

Starting in the 1950s, the increasing number of known particle species led to the notion that these particles were not necessarily the elementary constituents of matter, but rather composite objects made up of fewer, more fundamental particles.

Gell-Mann proposed in 1964 that hadrons could be constructed by combining three different flavours of quarks ( $u$ ,  $d$ ,  $s$ ) through the fundamental representation of an  $SU(3)$  group to form mesons ( $q\bar{q}$ ) and hadrons ( $qqq$ ). However, this approach encountered issues when cataloguing hadrons using the  $SU(3)$  group, as there were anomalous states like the  $\Omega^-$  ( $sss$ ) and the  $\Delta^{++}$  ( $uuu$ ), which contained three quarks of the same flavour in violation of the Pauli exclusion principle for fermions.

Moo-Young Han, Yoichiro Nambu, and Oscar W. Greenberg proposed a solution in 1965 by introducing an additional  $SU(3)$  gauge quantum number for quarks, known as colour charge (hence the name Quantum Chromodynamics) [11, 12]. This new quantum number, which can assume three states represented by the primary colours (red, green, and blue), explained why

$qq$ ,  $\bar{q}q$  and single quarks have never been observed directly. Moreover, the existence of colour charge gave rise to the possibility of various differently coloured states for each particle. However, the fundamental rule that resolved these contradictions was that all particle states observed in nature are „colourless” or „white” and unchanged under  $SU(3)$  rotations.

The strong interaction at its fundamental level is described by Quantum Chromodynamics (QCD). It is a theory based on a symmetry group of Special Unitary type,  $SU(3)$ . QCD is an invariant theory by local gauge transformation. It describes an unbroken symmetry, namely the conservation of the color quantum number. There are 8 different generators of the group  $SU(3)$ , so there must be eight gauge bosons. These bosons that mediate the strong nuclear force are called gluons, as already mentioned in the chapter. The Lagrangian density of the QCD is given by (1.1):

$$\mathcal{L}_{\text{QCD}} = \underbrace{i\bar{\psi}_q^i \gamma^\mu \partial_\mu \psi_{q,i}}_{\mathcal{L}_1} + \underbrace{g_s \bar{\psi}_q^i \gamma^\mu t_{ij}^a A_\mu^a \psi_q^j}_{\mathcal{L}_2} - \underbrace{m_q \bar{\psi}_q^i \psi_{q,i}}_{\mathcal{L}_3} - \underbrace{\frac{1}{4} G_{\mu\nu}^a G^{a\mu\nu}}_{\mathcal{L}_4}, \quad (1.1)$$

where the free gluon field  $G_{\mu\nu}^a$  is defined as:

$$G_{\mu\nu}^a = \partial_\mu A_\nu^a - \partial_\nu A_\mu^a + g_s f^{abc} A_\mu^b A_\nu^c. \quad (1.2)$$

In the Lagrangian density the index  $q$  iterates on all quark flavours, while  $i$  and  $j$  iterate on all quark colours. Quark and gluon fields are denoted with  $\psi$  and  $A_\mu^a$ , respectively, where the index  $a$  iterates over 8 different gluons.  $t^a$  are the  $3 \times 3$  Gell-Mann matrices, which are the  $SU(3)$  group generators, and  $\gamma^\mu$  are the Dirac matrices. The strong coupling constant  $\alpha_s$  is hidden in the parameter  $g_s$  ( $g_s^2 = 4\pi\alpha_s$ ) while  $f^{abc}$  is the structure constant of QCD. All the indices ( $q, i, \mu, \nu, a$ ) follow the Einstein summation convention.

The QCD Lagrangian is composed of four terms, where each term describes an aspect of the strong interaction. The first term  $\mathcal{L}_1$  corresponds to the kinetic energy of the quark field, while the last term  $\mathcal{L}_4$  defines the kinetic energy associated with the gluon field.  $\mathcal{L}_2$  is responsible for the interaction between quarks and gluons, and  $\mathcal{L}_3$  gives the mass of the quarks. Inside this one equation are summarized all the features of the strong interaction.

The third term in 1.2 implies that color charged gluons are allowed to mutually interact. This means that the force carriers interact with each other and that leads to some interesting phenomena. In other words, the coupling constant  $\alpha_s$  of QCD, which governs how strongly quarks and gluons interact (and gluons with other gluons), is not a constant at all, but is a function of the momentum transferred  $Q^2$  in the interaction. As the spatial separation between quarks grows ( $Q^2$  decreases), the coupling constant becomes larger and the energy of binding

increases, as seen in Fig. 1.2. This gives a strong interaction some unique properties compared to the other fundamental forces.

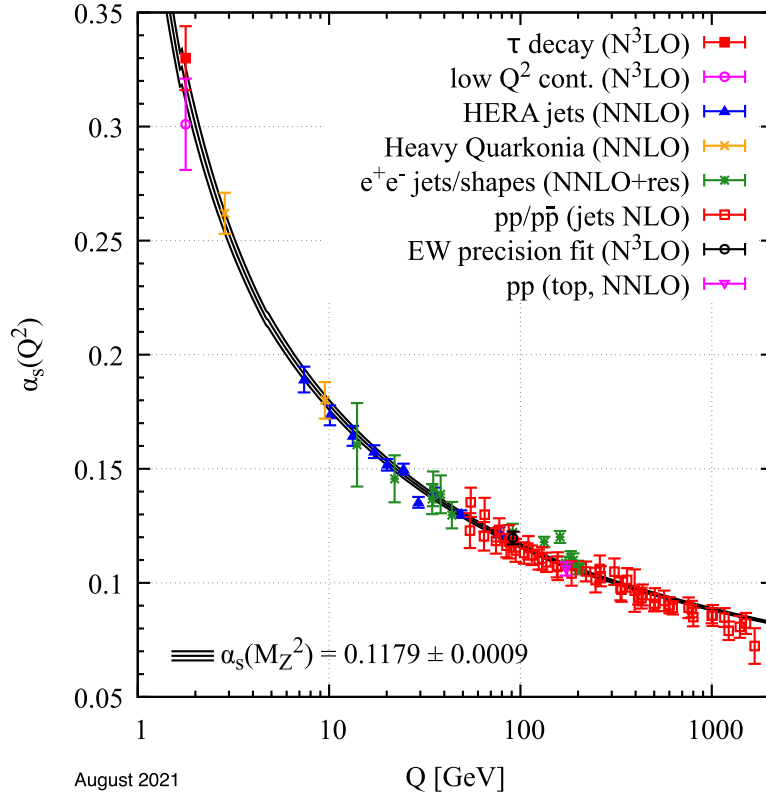


Figure 1.2: Summary of measurements of  $\alpha_s$  as a function of the energy scale  $Q$ . The respective degree of QCD perturbation theory used in the extraction of  $\alpha_s$  is indicated in brackets (NLO: next-to-leading order; NNLO: next-to-next-to-leading order; NNLO+res.: NNLO matched to a resummed calculation; N<sup>3</sup>LO: next-to-NNLO). [13].

The two main properties of the QCD that arise from this are:

**Colour confinement** states that individual quarks cannot exist freely by themselves as they must always be bound together to form color-neutral (also called „white”) hadrons (Fig. 1.3 left). When quarks are pulled apart, the energy stored in the field between them increases, and this energy is eventually sufficient to create a new quark-antiquark pair from the vacuum, which combines with the original quarks to form new hadrons. This is why it is called „confinement” and why all free particles are colour neutral.

**Asymptotic freedom** refers to the behavior of the strong force at very short distances, or at high energies, where the strong interaction becomes weaker as the distance between quarks

and gluons decreases and particles act like they are almost free from strong interaction. By reducing the distance between the quarks and gluons, the momentum transfer  $Q^2$  gets larger and the coupling constant becomes smaller (Fig. 1.2). This happens because gluons interact with each other. This phenomenon is known as „colour screening”.

The existence of asymptotic freedom suggests that under certain high energy conditions, quarks can move freely without strong interaction. When the density of hadrons becomes very high, „colour screening” becomes dominant and quarks become deconfined, meaning they are no longer bound to their original hadrons and are free to access the entire volume of the system. This state would be somehow similar to what we call plasma in QED, where ions and electrons are „deconfined”, so it was given a name quark-gluon plasma. The simplified diagram of the transition from the regular hadronic matter to the QGP is shown in Figure 1.3.

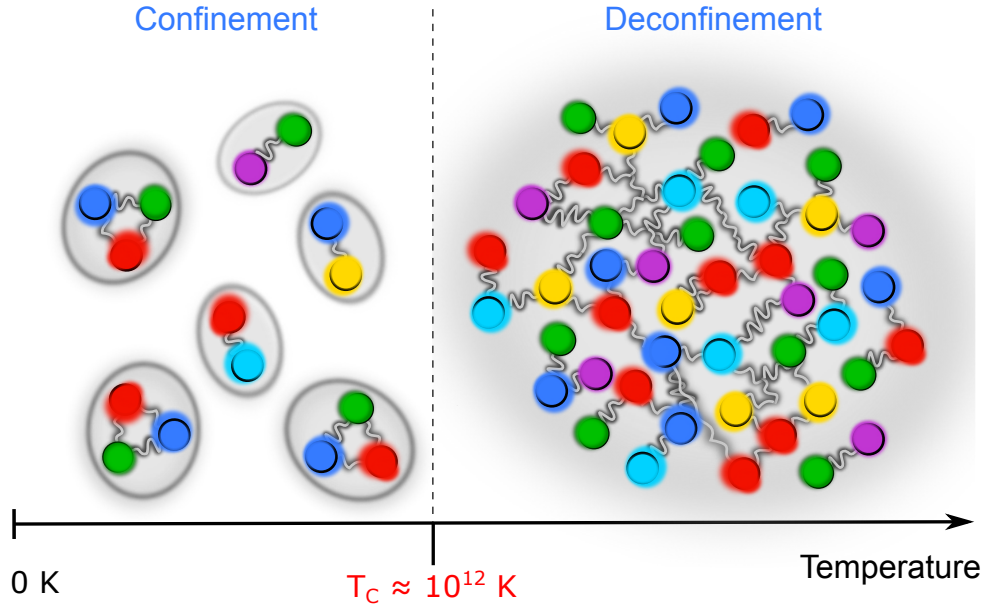


Figure 1.3: A simplified phase diagram of the nuclear phase transition from regular hadronic matter to the QGP phase. The anti-colours in mesons are shown by using (near) complementary colours ( $\bar{r}$  = cyan,  $\bar{b}$  = yellow,  $\bar{g}$  = purple). [14]

### 1.3 The quark-gluon plasma

The idea of quark-gluon plasma (QGP) was first proposed in the 1970s by theorists who were exploring the behavior of the strong force at very high temperatures and densities. At that time, the strong force was poorly understood, and there was much debate about whether quarks and

gluons could exist as free particles. It was not until the 1980s that the theory of QCD became well-established, and the idea of QGP became more widely accepted.

In the early 1990s, a series of experiments at the Relativistic Heavy Ion Collider (RHIC) and the Large Hadron Collider (LHC) aimed to create QGP in the laboratory by colliding heavy ions at very high energies, but it was not until the early 2000s that experimental confirmation was achieved [15]. They collided gold ions at very high energies and the collisions produced an extremely hot and dense fireball of quarks and gluons, which then rapidly expanded and cooled (Fig. 1.4). As the fireball expanded, the quarks and gluons recombined into hadrons, in a process called hadronization. The resulting recombined particles were detected by the RHIC detectors, and detailed analysis showed that the particles produced in the collisions had a collective behavior that was consistent with the formation of a new state of matter - QGP. Further experiments at RHIC and LHC have provided additional evidence for the existence of QGP, which behaves like a nearly-perfect liquid, with very low viscosity and other properties that are consistent with the predictions of QCD.

The most obvious reason to study the properties of QGP is to learn more about the nature of strong interaction and to test the predictions of QCD. This correlates with a better understanding of how physics works on the smallest scales. This is a good enough reason for every physicist to spend their life exploring this exotic state of matter. But, there is another reason to study QGP properties, which may sound even more exciting.

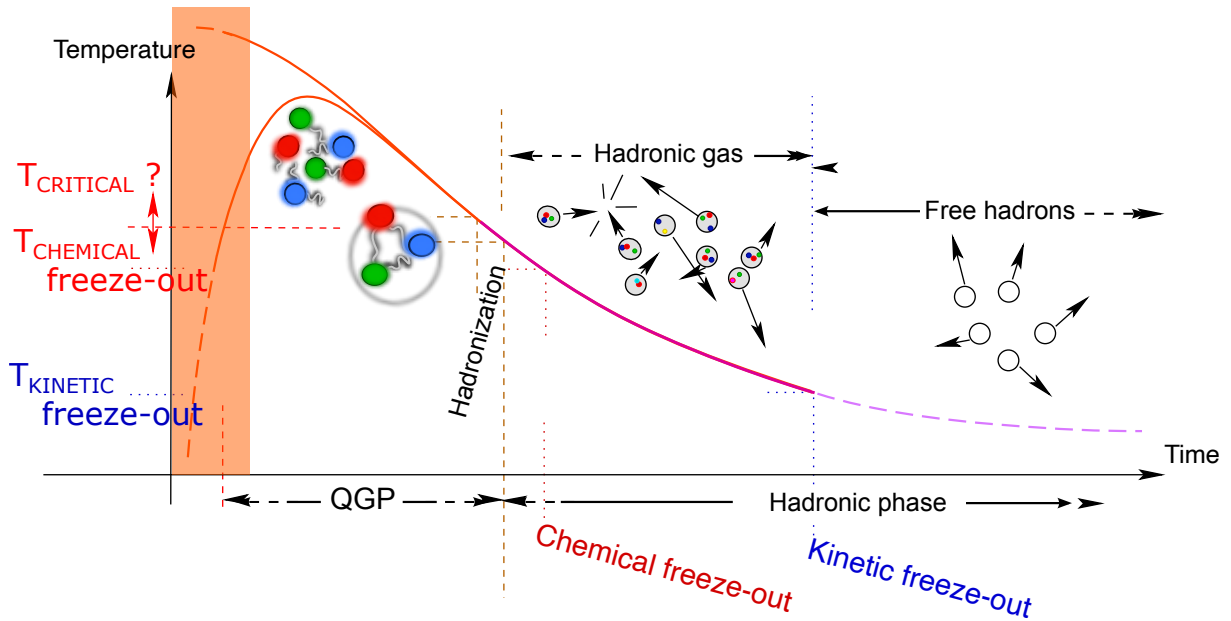


Figure 1.4: The Bjorken scenario foreseen for the collision of ultra-relativistic heavy ions. [16]

The Universe as we know it today started with the Big Bang, an explosive event that occurred around 13.8 billion years ago. In the first few microseconds after the Big Bang, the Universe was extremely hot and dense, with temperatures and pressures far beyond what can be achieved in any laboratory on Earth. In Figure 1.5, the Big Bang happens in the upper left corner (high temperature and low baryon density), and while it cools it passes from the QGP phase through hadronic gas into the „ordinary” state, which is the current state of the Universe. We can recreate some of the conditions that existed during the early period of the Universe by colliding heavy ions at high energies, which produces a tiny fireball of QGP that mimics the conditions that existed just after the Big Bang. This allows us to create QGP in a controlled environment where we can observe and study it. Studying its properties can help us understand the evolution of the early Universe, including how it expanded and cooled, how particles formed and interacted, and how the first structures and galaxies emerged. We can test and refine our understanding of the early Universe, and shed light on some of the deepest mysteries of cosmology.

The QGP generated by colliding heavy ions exists for only a short period of time (around  $10^{-23}$  seconds), as it quickly cools down and hadronization starts. As a result, it is not directly observable by our detectors. Instead, we can only observe the particles that are formed as a result of the hadronization (Fig. 1.4). By examining the properties of these particles, such as their types, energies, number, and flight direction, we can deduce the presence of QGP and even study some of its properties. When QGP is produced in collisions, the types of created particles and their properties are different compared to when there is no QGP. This leads to specific phenomena called QGP signatures, as their appearance indicates that QGP was created after the collision. Some of the signatures of QGP, both measured and theoretical, are discussed below.

### 1.3.1 Signatures of QGP

It has now been accepted for a long time as a fact that the QGP is produced in heavy ion collisions. It was also believed that QGP cannot be created in proton-proton collisions because the size of that system is too small. By comparing certain phenomena that were observed in collisions of heavy ions and not in pp collisions, certain properties of collisions are found unique when QGP is actually formed in a collision. With the increase in collision energies, in the last few years, QGP signatures began to appear in pp collisions as well. So the signatures were gradually removed when they were observed in pp collisions. As time passed and collision energies increased, more and more QGP signatures continued to appear in pp collisions. Does this mean that QGP is also created in pp collisions, or were our signatures wrong? This question

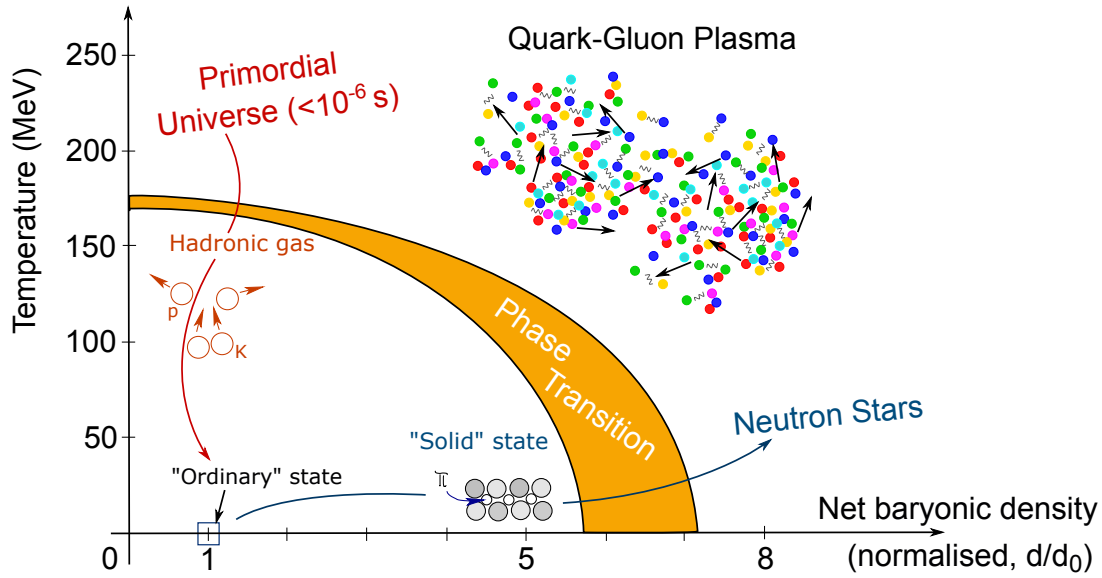


Figure 1.5: Phase diagram (temperature, net baryon density) of QCD matter, ranging from regular nuclear matter to Quark-Gluon Plasma. [17]

has not yet been fully answered, but the formation of a QGP droplet in pp collisions is now considered as a possible solution.

As signatures change over time, I will now list only some of them that are currently accepted, where the last one, the strangeness enhancement, is the main topic of this research [18]:

**Jet quenching** is a phenomenon that occurs because high-energy quarks or gluons pass through the dense and strongly interacting QGP and lose a part of their energy, which results in a jet with less energy than expected. The jets are formed when partons (quarks and gluons) hadronize after heavy-ion collisions and resulting hadrons form a narrow cone of particles, known as a jet. If there is QGP created after the collision, these partons pass through it, and lose some of their initial energy, so the jets created from hadronization have less energy. This phenomenon is the most obvious when there are two jets form from the same spot. The sum of momenta of both jets must be zero, but if one of the jets passes a longer distance through the QGP than the other, the two jets will carry different momenta or sometimes only one jet will be visible. Jet quenching is still not observed in pp collisions.

**Anisotropic flow** arises from the pressure gradients generated by the almond-shaped overlap region of the colliding nuclei. During the early stages of the collision, the pressure gradients cause the matter to expand preferentially in the direction perpendicular to the collision plane, resulting in an anisotropic distribution of matter. As matter continues to ex-

pand and cool, the pressure gradients decrease and the anisotropy gradually disappears. The initial spatial anisotropy of the almond shape is converted to momentum anisotropy observed as a phenomenon named elliptic flow. Flow studies have led to the understanding that the QGP behaves like a strongly-coupled liquid, rather than a weakly-interacting gas. This QGP signature is observed in high multiplicity events in small systems (pp and p-Pb collisions).

**Direct photons** can provide information on the temperature of the QGP, as the rate of direct photon production increases with increasing temperature. Additionally, the polarization of direct photons can also provide insights into the properties of the QGP, such as its viscosity and whether it behaves like a liquid or a gas. Transverse momentum distributions of direct photons have been measured at both RHIC and the LHC, where the enhancement at low transverse momentum ( $p_T$ ) in central heavy-ion collisions relative to the scaled pp data is well described by perturbative QCD. The excess indicates photon production due to thermal radiation from the QGP.

**Debye screening effect** is also known as suppression of heavy quarkonium. Heavy quarkonium (heavy quark and its own antiquark) such as charmonium or bottomonium is expected to dissolve in the QGP when the potential between the quarks is screened by copious color charges of quark and gluon in the plasma, i.e. the Debye screening effect. The suppression of heavy quarkonia in heavy-ion collisions is due to a combination of two effects. The first effect is colour screening. In the QGP, the heavy quark and its antiquark are surrounded by a cloud of color charges, which reduces the strength of the strong force between them. This makes it more difficult for the heavy quarkonia to form and survive. The second effect is the dissociation of pre-existing quarkonia as they travel through the QGP. The high temperature and density of the QGP can cause the quarkonium to break apart into its constituent quarks and gluons, a process known as dissociation.

**Strangeness enhancement** was long considered one of the most promising QGP signatures. Strange quarks have a larger mass than up and down quarks, so they are less likely to be produced in high energy collisions. But, if the QGP is formed after the collision, a gluon can dissolve into a pair of strange quark-antiquark, so there is a greater chance for a particle containing one or more strange quarks to appear after hadronization. With increasing collision energies, the strangeness enhancement was recently observed in pp collisions, so it remains to be found out if it is really a QGP signature or not. This phenomenon is the main interest of this thesis and it will be discussed in greater detail in the next chapter.



## 1.4 High energy collisions

The strong interaction can only be experimentally studied through high energy collisions of two nuclei. Due to the confinement of quarks and the short range of the strong nuclear force, it is impossible to research their interactions without breaking them apart. To achieve this, huge accelerators have been constructed, capable of colliding two nuclei at speeds approaching the speed of light. The nuclei, comprised of quarks, can be broken apart at sufficiently high energies, allowing for the study of quark interactions while they are free from their original hadrons. Of particular interest is the behavior of quarks within the QGP phase, where they behave asymptotically free.

Collisions in accelerators are divided into three main categories: proton-proton, proton-ion and ion-ion collisions. In proton-proton collisions, two protons are accelerated and then collide with each other. Since protons are relatively simple particles, the collisions produce a relatively small number of particles in the final state. The number of particles in the final state is called multiplicity. Most of pp collisions have low multiplicity and are therefore generally simpler and easier to analyze compared to heavy ion collisions. In contrast, heavy ion collisions involve the collision of two heavy ions, such as gold or lead, which have many more protons and neutrons than a single proton. So they produce a much larger number of particles in the final state than proton-proton collisions, i.e., have a higher multiplicity, making them more complex and difficult to analyze. They are also more memory consuming and lead to faster detector deterioration. With proper scaling of pp collisions and comparing them to heavy ion collisions, it is possible to spot differences indicating the formation of QGP after a heavy ion collision.

Multiplicity is directly correlated to the centrality of the collision. Centrality is the degree of overlap between two colliding ions and is characterised by the impact parameter. The impact parameter  $b$  is defined as the distance between the centers of the two nuclei (Fig. 1.6). The smaller impact parameter leads to larger overlap, which means that the average number of nucleons participating, so-called participants, will be higher. The nucleons that are not colliding are called spectators. With a larger number of participants, the final state of the collision will have a higher multiplicity.

The collision evolution starts with two bunches of nuclei approaching each other. In the ideal case, we could do a collision with only two nuclei, but in reality, the beam is injected with bunches of ions or protons. The bunches are flattened because of length contraction, as they move close to the speed of light (Fig. 1.6). As the bunches of nuclei traverse through one another, individual nucleons undergo collisions, resulting in production of different partons. The precise mechanism behind the creation of these partons remains incompletely understood,

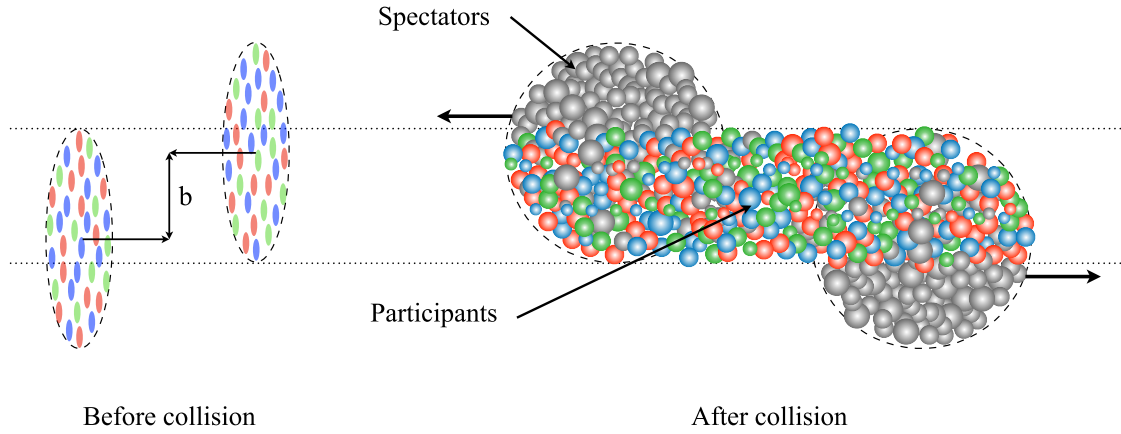


Figure 1.6: A schematic view of a heavy-ion collision. The impact parameter  $b$  is shown as well as the spectator nucleons and the participant nucleons. [19]

as their production processes cannot be calculated perturbatively. At this stage, the system exists in a pre-equilibrium state, where the partons have not yet had sufficient time to interact with neighboring particles and achieve thermal equilibrium.

As the partons interact with each other, they gradually thermalize, leading to the formation of a QGP. The QGP exhibits characteristics similar to those of a nearly perfect liquid, expanding in response to pressure gradients as dictated by hydrodynamic principles. This expansion gives rise to collective flow, wherein particles are propelled outward in a radial direction. As the system continues to expand, it gradually cools, eventually reaching temperatures and energy densities below the critical values required for the existence of the QGP.

Within the QGP, the partons start combining to form hadrons, resulting in a temporary mixed phase. This transition, known as chemical freeze-out, marks the point at which the system entirely transforms into a hadron gas. Although referred to as a hadron gas, the individual hadrons can still engage in elastic scatterings with one another, enabling the exchange of energy. After a certain time, the system becomes too sparse for significant interactions to occur between particles. This stage is referred to as kinetic freeze-out, beyond which the particles continue to propagate through the detector while preserving their trajectories and momenta. The schematic representation of the collision evolution is shown in Figure 1.7.

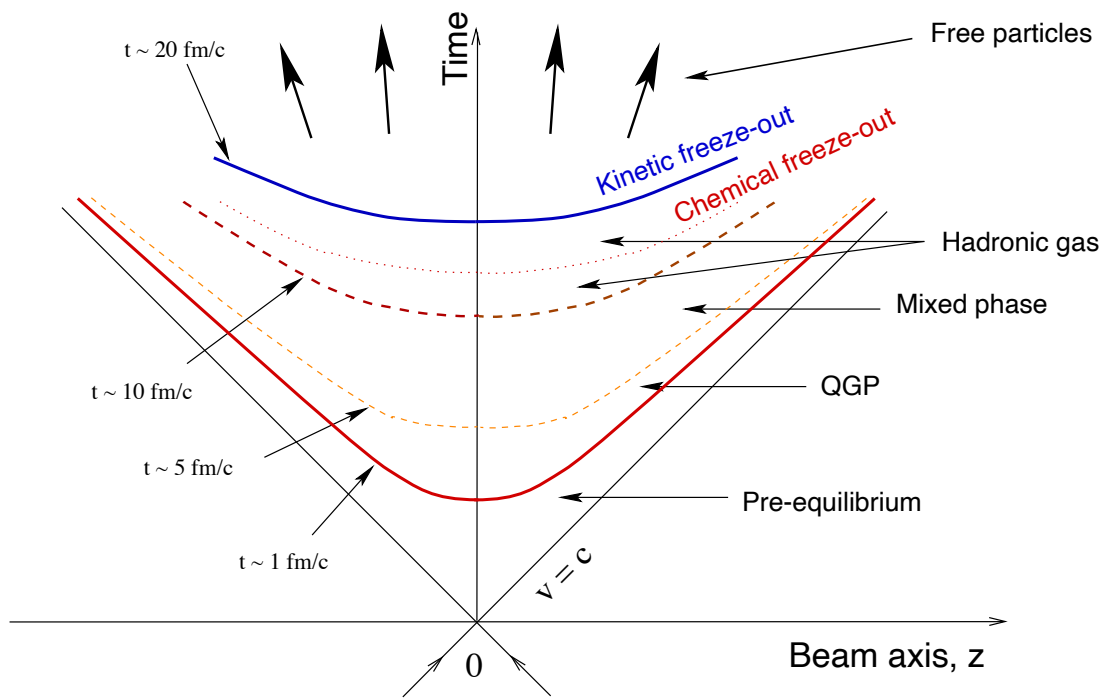


Figure 1.7: The evolution of the collision of ultra-relativistic heavy ions. [16]

## Chapter 2

### Physics of strangeness

In 1947, researchers studying cosmic rays observed  $K^-$  mesons for the first time. These particles exhibited longer lifetimes and unusual decay patterns and were initially named „strange” due to their peculiar behavior. The observation of strange mesons led scientists to speculate that there might be a new fundamental particle associated with their decay. Later, in 1953, these particles were made in the Cosmotron at the Brookhaven National Laboratory (BNL), and soon whole families of these particles were discovered.

In 1964, Murray Gell-Mann and Yuval Ne’eman independently proposed a mathematical scheme known as the Eightfold Way, which aimed to classify the various observed mesons and baryons based on their properties. They proposed that all baryons were composed of triplets of quarks (selected from  $u, d$  and  $s$ ) and the mesons were doublets formed by a quark and an antiquark. Gell-Mann’s formulation of the quark model gained wider acceptance, and he was awarded the Nobel Prize in Physics in 1969 for his contributions [20].

With the establishment of the quark model, scientists realized that the peculiar behavior of strange mesons could be explained by the existence of another type of quark, which was later named the strange quark. The strange quark was hypothesized to carry a fractional electric charge and possess certain unique properties. Experiments in the late 1960s and early 1970s [21, 22], including deep inelastic scattering, provided additional evidence supporting the existence of strange quarks. These experiments helped confirm the predictions of the quark model and establish the existence of strange quarks as an integral part of our understanding of particle physics. In 1974, the discovery of a new particle called the  $J/\Psi$  meson at the Stanford Linear Accelerator Center (SLAC) and at the Brookhaven National Laboratory (BNL) provided strong evidence for the existence of the charm quark. The observation of this particle’s properties, such as its mass and decay behavior, was consistent with the predictions of the quark model and the existence of the charm quark.

## 2.1 Hyperons

Hyperons are a group of subatomic particles that belong to the baryon family that contain one or more strange quarks within their quark composition but not any heavier quarks (like charm, top and bottom). As there are three different flavours of quarks ( $u, d, s$ ) used to make a hyperon, the previously mentioned quark model (eightfold way) can be used to determine all the possible configurations of hyperons. These quarks are the three lightest quarks in mass, so together they are called the light flavoured (LF) quarks. The properties of LF quarks can be seen in Figure 1.1.

Group representation theory provides a mathematical foundation for the organization of particles, known as the eightfold way. The technical aspects of this theory are not really necessary for understanding how it helps organize the particles. The categorization is based on the spin angular momentum of the particles. All quarks are fermions, which means they have a spin equal to one half, and if there are three quarks in a hyperon their spins can be organized in two ways: their total spin angular momentum can be equal to one half or to three halves.

When plotting the strangeness of particles against their electric charge, symmetrical patterns emerge. The symmetry observed in these patterns suggests the underlying symmetry of the strong interaction among the particles themselves. In the plots seen in Figures 2.1 and 2.2, particles lying along the same horizontal line share the same strangeness ( $S$ ), while those on the same left-leaning diagonals share the same electric charge ( $Q$ , given in terms of elementary charge multiples). Strangeness ( $S$ ) is a quantum number that corresponds to the number of strange quarks inside a hadron. By convention, the  $s$  quark has  $S = -1$ , while the antiquark  $\bar{s}$  has  $S = 1$ .

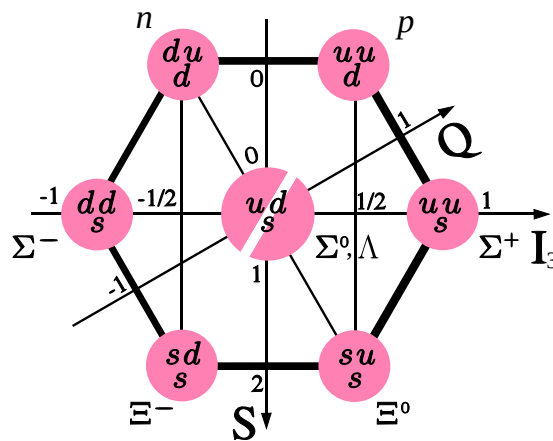


Figure 2.1: Combinations of light flavoured quarks forming baryons with a spin - 1/2 form the  $uds$  baryon octet. [23]

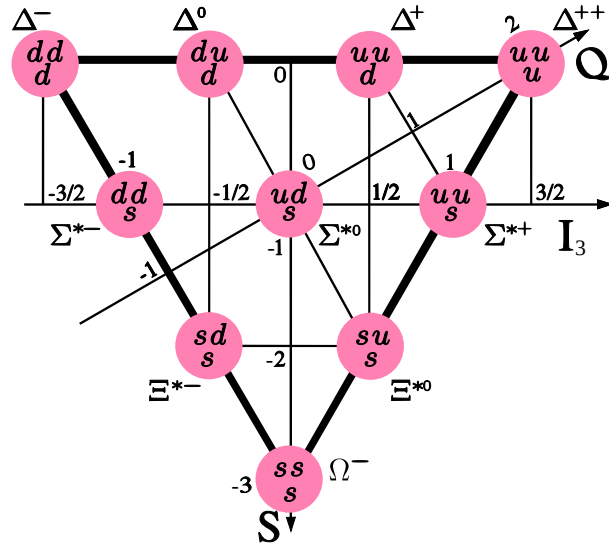


Figure 2.2: Combinations of light flavoured quarks forming baryons with a spin - 3/2 form the  $uds$  baryon decuplet. [23]

The third axis, marked as  $I_3$  represents the projection of isospin  $I$ . The isospin is a quantum number related to the up and down quark content of the particle. The  $u$  quark has  $I = 1/2$  while the  $d$  quark has  $I = -1/2$ . It is also important to mention that  $u$  and  $d$  can couple to two different states of isospin: zero or one. Hadrons with the same quark content but different total isospins can be distinguished experimentally, verifying that flavour is actually a vector quantity, not a scalar (up vs. down simply being a projection in the quantum mechanical  $z$  axis of flavour space). For example, a strange quark can be combined with an up and a down quark to form a baryon, but there are two different ways the isospin values can combine: either adding (due to being flavour-aligned) or canceling out (due to being in opposite flavour directions). The isospin-1 state (the  $\Sigma^0$ ) and the isospin-0 state (the  $\Lambda^0$ ) have different experimentally detected masses and half-lives. The difference is in their wave function and in the way they strongly interact. One way to think about this is that the  $\Sigma^0$  nucleus is just an excited state<sup>1</sup> of the  $\Lambda^0$  nucleus.

In Figures 2.1 and 2.2, all particles that contain one or more  $s$  quarks are hyperons ( $\Lambda_0$ ,  $\Sigma$ 's,  $\Xi$ 's and  $\Omega$ 's). The ones with the asterisk symbol (\*) have a really short lifetime and decay almost immediately after creation and are therefore called „resonances“. The remaining ones are more stable and are listed in table 2.1 where the superscript marks the charge of the particle.

To study the production of hyperons, they must not decay too quickly after the collision, and they must decay into something that detectors can identify. It is easier to identify charged

<sup>1</sup>Usually excited states refer to electron excitation in an atom, but here the nucleus is excited.

Table 2.1: Table of hyperons with their measured rest mass, mean lifetime and most common decay modes. [13]

Particle	Mass (MeV/ $c^2$ )	Mean lifetime (s)	Decay modes
$\Lambda^0$	1115.683(6)	$2.632 \pm 0.020 \times 10^{-10}$	$p\pi^-$ or $n\pi^0$
$\Sigma^+$	1189.37(7)	$0.8018 \pm 0.0026 \times 10^{-10}$	$p\pi^0$ and $n\pi^+$
$\Sigma^0$	1192.642(24)	$7.4 \pm 0.7 \times 10^{-20}$	$\Lambda^0\gamma$
$\Sigma^-$	1197.449(30)	$1.479 \pm 0.011 \times 10^{-10}$	$n\pi^-$
$\Xi^0$	1314.86(20)	$2.90 \pm 0.09 \times 10^{-10}$	$\Lambda^0\pi^0$
$\Xi^-$	1321.71(7)	$1.639 \pm 0.015 \times 10^{-10}$	$\Lambda^0\pi^-$
$\Omega^-$	1672.45(29)	$0.821 \pm 0.011 \times 10^{-10}$	$\Lambda^0 K^-$ or $\Xi^0\pi^-$ or $\Xi^-\pi^0$

particles as their track is curved by the magnetic field inside the detector. The best candidates for studying the production of hyperons are the  $\Lambda^0$ ,  $\Xi^-$ ,  $\Omega^-$  and their antiparticles.  $\Xi^-$  and  $\Omega^-$  are a logical choice as they contain two and three  $s$  quarks, are both charged and decay to at least one charged particle. The preference for  $\Lambda^0$  over  $\Sigma^0$  is because  $\Sigma^0$  decays pretty quickly to  $\Lambda^0$  ( $\Sigma^0 \rightarrow \Lambda^0 + \gamma$ ), and  $\Sigma^\pm$  always have one neutral particle in their decays compared to the dominant decay mode of  $\Lambda^0$  ( $\Lambda^0 \rightarrow p + \pi^-$ ).

This thesis will only look at the production of the multi-strange hyperons  $\Xi^-$ ,  $\Omega^-$  and their antiparticles. It can be seen in table 2.1 and Figure 2.3 that the multi-strange hyperons first decay to a hyperon with fewer  $s$  quarks, and then that hyperon decays into stable particles. This is why the  $\Xi$ 's and  $\Omega$ 's are called „cascades”, as they decay in steps to stable particles, that are then detected.

## 2.2 Strangeness production

Our world is mostly made of protons, neutrons and electrons. It is only when we observe radiation from the Universe that we notice some other particles. Protons and neutrons can be described by using only up and down quarks. Therefore, if we want to study other types of quarks, such as the strange quark, we first need to find a way to produce them. High-energy collisions are a common way to produce exotic particles. Depending on whether QGP is formed after the collision or not, strange quarks are produced through different mechanisms.

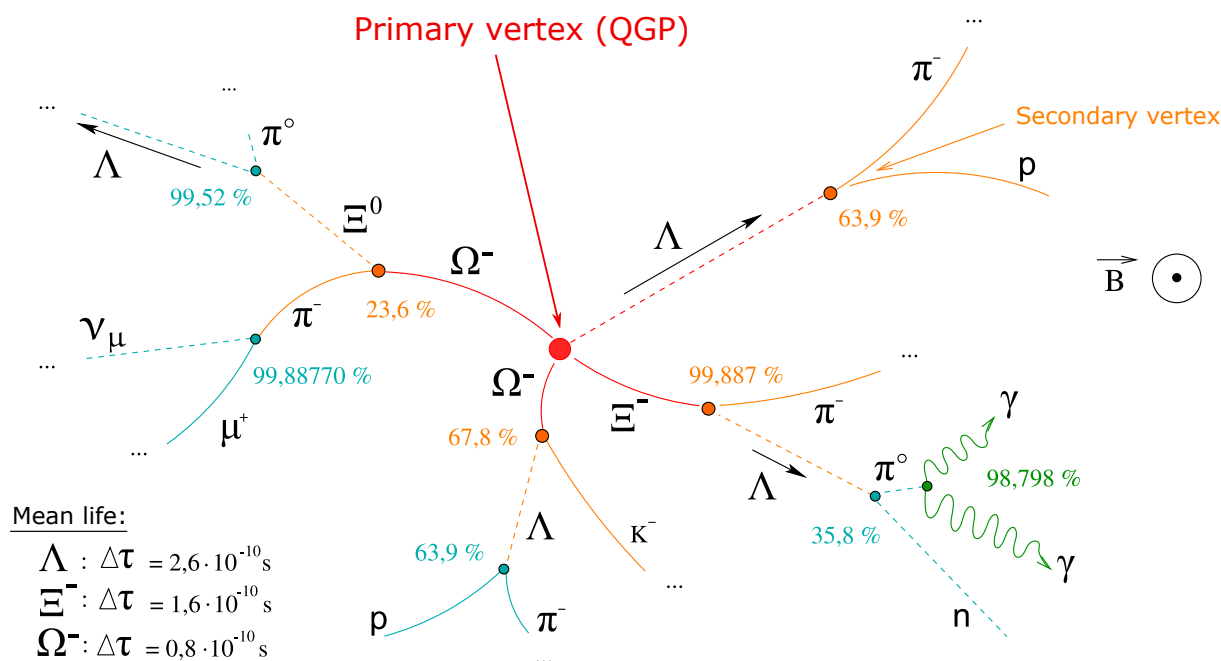


Figure 2.3: Examples of decay chains for some typically produced hyperons. The percentages next to the vertices represent the branching ratios of associated channels. [24]

### 2.2.1 Strangeness production in hadron gas

If there is no QGP, quarks remain confined inside hadrons. This state after the initial collision is called the hadron gas (HG). Inside the HG, hadrons collide with each other, leading to the formation of new particles through these collisions. Creating a hadron containing a strange quark within the HG is not an easy task. Direct production of a single strange hadron is not allowed due to strangeness conservation<sup>2</sup>. This means that strange and anti-strange particles must be created in the same interaction. For example, it is not possible to have an interaction between two nuclei  $N$  that goes like:  $N + N \rightarrow N + \Lambda$  because the strangeness on the left side is zero, while on the right side, it is minus one. Therefore, to create a strange hadron pair, the simplest process should look like this:

$$N+N \rightarrow N+N+\Lambda+\bar{\Lambda}, \quad (2.1)$$

where there are two nuclei on the right side, as the baryon number must be conserved<sup>3</sup> as well. This means that the minimal energy cost of creating the strange hadron pair equals to their

<sup>2</sup>Strangeness is conserved during the strong and the electromagnetic interactions. Conservation can be violated, but only through the weak force, and those processes occur on larger timescales, so they are not considered immediately after the collision.

<sup>3</sup>The baryon number is conserved in all the interactions of the Standard Model.



combined rest mass: 2642 MeV for the  $\Xi^- + \bar{\Xi}^+$  and 3344 MeV for the  $\Omega^- + \bar{\Omega}^+$ .

When there is indirect production, the energy cost is a bit lower, but there is also a lower chance of creating multi-strange hyperons. For the creation of a multi-strange hyperon, one would need to have two or three reactions in sequence. First, there is the production of a light hyperon:

$$N + N \rightarrow N + K + \Lambda. \quad (2.2)$$

The energy needed for the production of kaon and lambda is roughly equal to the difference in their masses and the mass of the nucleon (around 670 MeV). Then, to create a  $\Xi$  or an  $\Omega$ , the reaction (2.2) must be followed by one or two reactions:

$$\pi + \Lambda \rightarrow K + \Xi, \quad (2.3)$$

$$\pi + \Xi \rightarrow K + \Omega. \quad (2.4)$$

The additional energy needed to produce multi-strange hyperons is around 1100 MeV for the  $\Xi^-$  and 1810 MeV for the  $\Omega^-$ . This chain of reactions has a low probability and therefore takes a long time. In addition to this low probability, multi-strange hyperons can be destroyed in interactions with pions or nucleons.

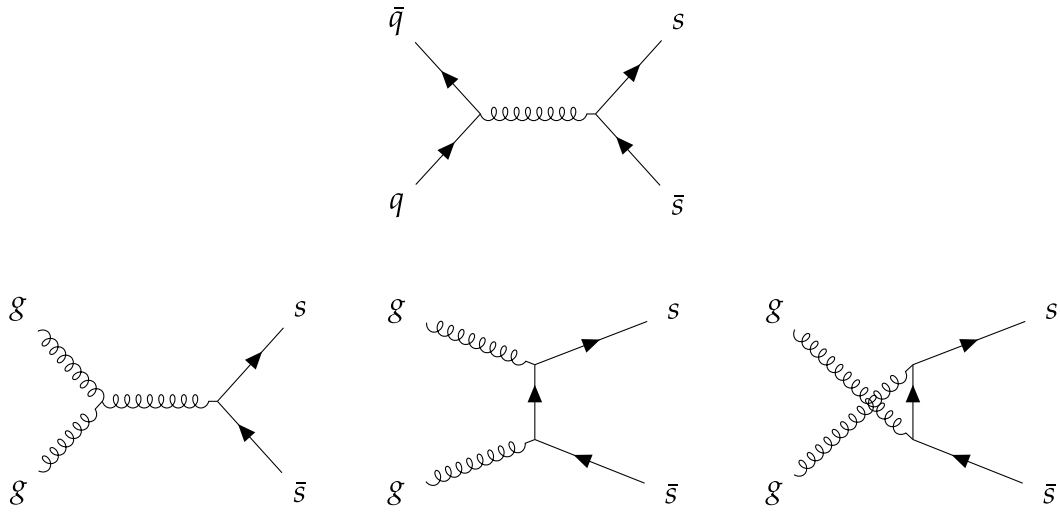
### 2.2.2 Strangeness production in QGP

If the QGP is created after the collision, strange quarks can be produced through quark pair annihilation or gluon fusion processes [25]. In the lowest order in perturbative QCD,  $s\bar{s}$  quark pairs can be created by the annihilation of light  $q\bar{q}$  pairs (upper diagram in Fig. 2.4) and in the collisions of two gluons (three lower diagrams in Fig. 2.4).

$$q + \bar{q} \rightarrow s + \bar{s}, \quad (2.5)$$

$$g + g \rightarrow s + \bar{s}. \quad (2.6)$$

The gluon fusion processes are dominant and produce most of the  $s\bar{s}$  inside the QGP. In these reactions, the energy needed to produce  $s\bar{s}$  is approximately equal to the mass of a pair, which is around 200 MeV. Compared to the production in the HG, these processes need an order of magnitude less energy to create the  $s$  quark, which will later form the hyperon.

Figure 2.4: Feynmann diagrams for  $s\bar{s}$  production in QGP.

Another important point is the difference in equilibration times between partonic reactions and hadronic reactions, particularly due to the gluon fusion process. In partonic scenarios, where quarks and gluons exist as an ideal gas at temperatures around 200 MeV, equilibration times of 10 fm/c can theoretically be achieved. This is comparable to the total duration of a heavy ion interaction, from initial collisions to the final freeze-out of hadrons. However, the duration of the QGP phase within this time span is even shorter, indicating that partonic processes alone may not be sufficient to fully establish chemical equilibrium in the system. [25]

On the other hand, it has been observed that in a gas of free hadrons [26], the time required to reach an equilibrium state strongly depends on the strange particle species. For particles with strangeness  $|S| = 1$ , such as  $K$  and  $\Lambda$ , chemical equilibrium may be achieved after approximately 30 fm/c and for rare (anti-)hyperons, the timescales for equilibration can be an order of magnitude longer. This suggests that producing large quantities of multi-strange particles in a hadron gas would be very challenging, while the presence of a QGP would lead to much higher production rates of these particles. In the latter case, the multi-strange particles would primarily form through quark hadronization, schematically shown in Figure 2.5, with their yields approaching the expectations of chemical equilibrium. [27]

## 2.3 Strangeness enhancement

In the previous chapter, it was argued that there should be an evident difference in the number of produced hyperons depending on whether QGP is created after the collision or not. This leads to the conclusion that hyperons, especially multi-strange ones, would be produced in

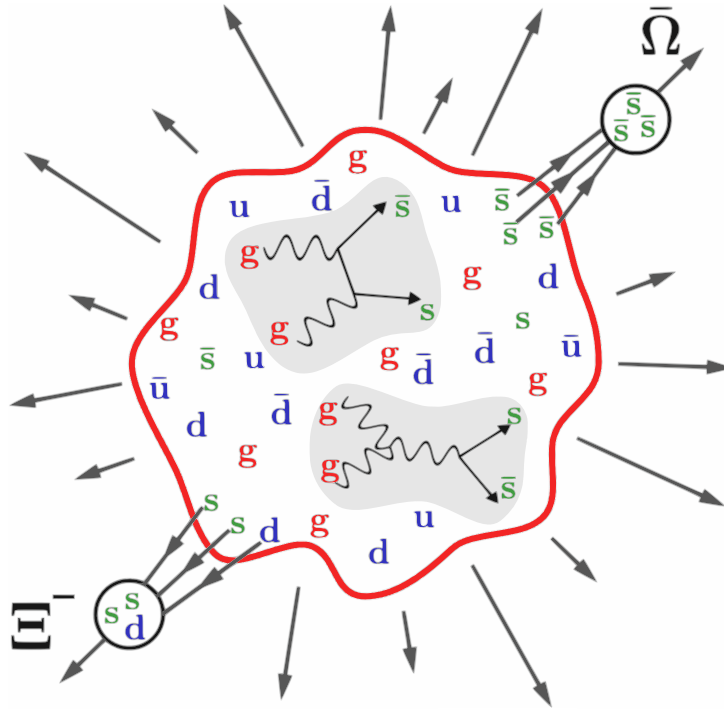


Figure 2.5: Simple visualization of  $\Xi^-$  and  $\bar{\Omega}^+$  hadronization from QGP.

greater numbers in the case where QGP is produced. This phenomenon of enhanced production of strange hadrons would indicate QGP formation, making it one of the first possible QGP signatures.

The theory was first proposed in 1982 by Rafelski and Muller [25]. After proposing the existence of strangeness enhancement, it was observed that in collisions of heavy ions with increasing multiplicity, there is an increase in the production of strange particles with respect to other particles [28]. As the reason for such a phenomenon was not known, the most accepted theory was that of Rafelski and Muller, that it was due to QGP being formed immediately after the heavy ion collision and it was long considered one of the signatures of QGP.

As high temperature and/or high density of matter is required to form QGP, it was expected that the enhancement would be achieved in heavy ion collisions, while in collisions of two protons, the number of participants is much lower and the formation of QGP was considered impossible. As increasing collision energies were achieved at the LHC, it has been observed that most QGP signatures are also seen in high-multiplicity pp collisions. The strangeness enhancement, which is the topic of this research, was recently observed in pp collisions at an energy of 13 TeV [1]. As the appearance of quark-gluon plasma was considered possible only in heavy ion collisions, this phenomenon is no longer a definite signature of QGP and the theory behind the phenomenon itself is no longer as accepted [29].

At energies of 13 TeV in pp collisions at the LHC, high multiplicity events become comparable to those in peripheral heavy ion collisions. In central Pb-Pb collisions, a maximum of about 20 000 charged particles are produced in the pseudorapidity range  $|\eta| < 0.5$ , while for peripheral Pb-Pb and pp collisions of high multiplicity, there is an order of magnitude of 100 such particles. Thus, we can observe the trend of the production of strange hadrons from low-multiplicity pp collisions to central Pb-Pb collisions. The results show a growing trend until saturation occurs at very high multiplicities in more central lead-lead collisions [30, 31, 32], as seen in Figure 2.6.

It has also been shown that the phenomenon of strangeness enhancement is more pronounced the more strange quarks a hadron contains. The ratios of produced strange hadrons<sup>4</sup> relative to produced pions are shown in Figure 2.7. This means that increasing the multiplicity of events will increase the relative number of  $\Omega$  hyperons formed versus the increase in the number of  $\Xi$  hyperons. The production of strange hadrons at different pp, p-Pb and Pb-Pb collision energies (for pp from 0.9 to 13 TeV, for p-Pb 5.02 and 8.16 TeV, Pb-Pb 2.76 and 5.02 TeV) gives similar results at equal multiplicities, which leads to the conclusion that the production of strange hadrons does not depend on the initial system or the energy of the collision itself but only on the final state of the system [2]. These measurements were made for hyperons:  $\Lambda(uds)$ ,  $K_0^S(ds)$ ,  $\Xi(dss)$  and  $\Omega(sss)$  and their antiparticles. In this study, the analysis will be done only for  $\Xi$ 's and  $\Omega$ 's where there is the least processed data, because these are the heaviest hyperons and are therefore produced in the smallest numbers.

Today, the production of strange particles in heavy ion collisions is described by statistical hadronic (thermal) models. In central heavy ion collisions, the production of strange hadrons is consistent with the production in hadronic gas in thermal and chemical equilibrium and can be described by a grand canonical ensemble [33, 34]. In peripheral collisions, the production of strange particles versus pions decreases and approaches the numbers obtained in pp collisions, for which statistical models are also used [35, 36]. Additional models are added to the pure grand canonical model, such as strangeness canonical suppression and core-corona superposition models, which successfully describe the suppression of strange particle formation in small systems [37, 38]. But this still doesn't describe the microscopic origins of strangeness enhancement, so improved statistics for small systems could contribute to a better understanding of the phenomenon.

As the growth trend of strangeness production is observed from low-multiplicity pp collisions all the way to central Pb-Pb collisions where saturation occurs, it could be concluded that in the background of strange particle production lies the same physical principle. The area of

<sup>4</sup>Number of strange hadrons per unit of pseudorapidity.

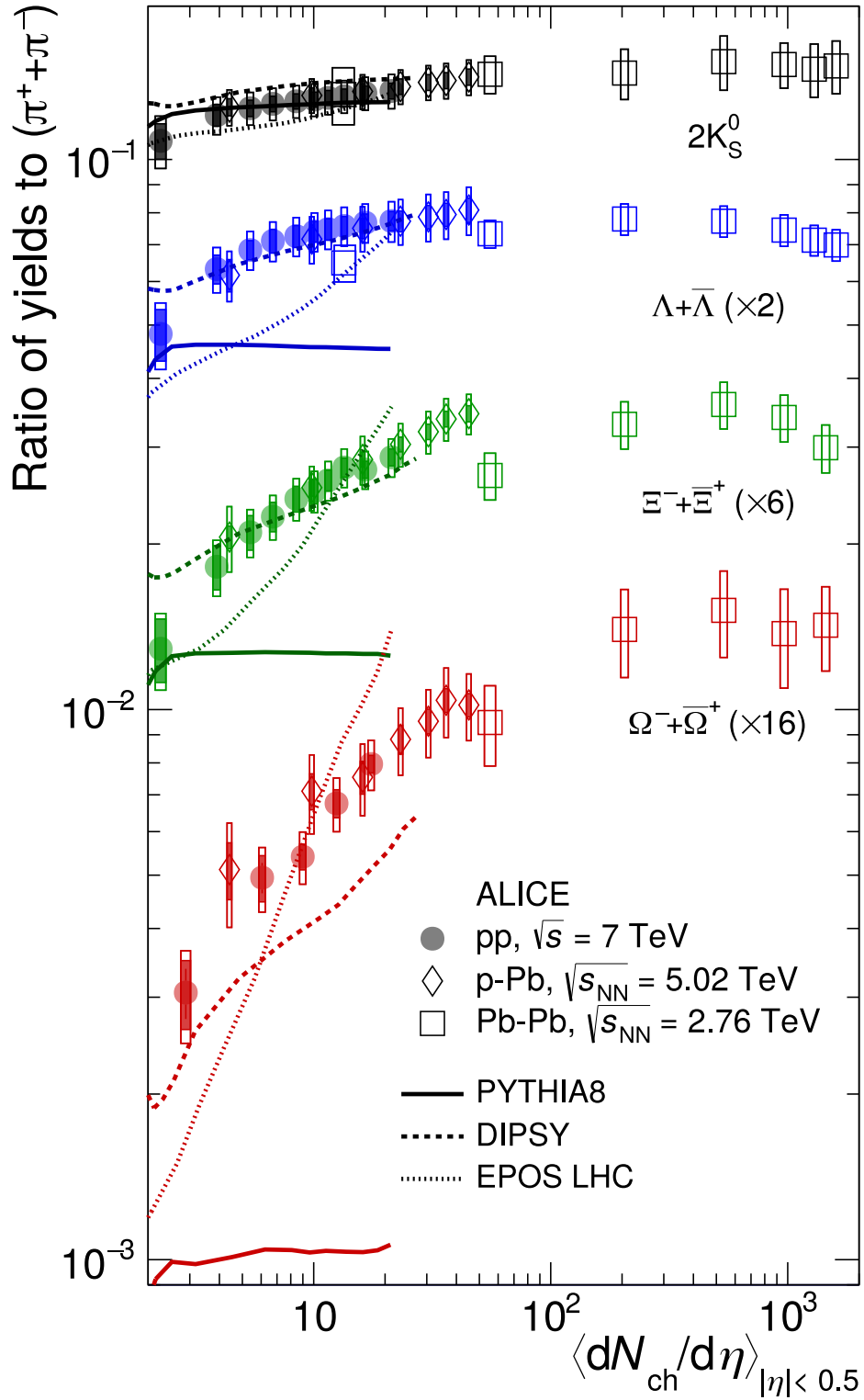


Figure 2.6:  $p_T$ -integrated yield ratios to pions as a function of multiplicity ( $dN_{ch}/d\eta$ ) measured in  $|\eta| < 0.5$ . The values are compared to calculations from MC models and to results obtained in p-Pb and Pb-Pb collisions at the LHC. [2]

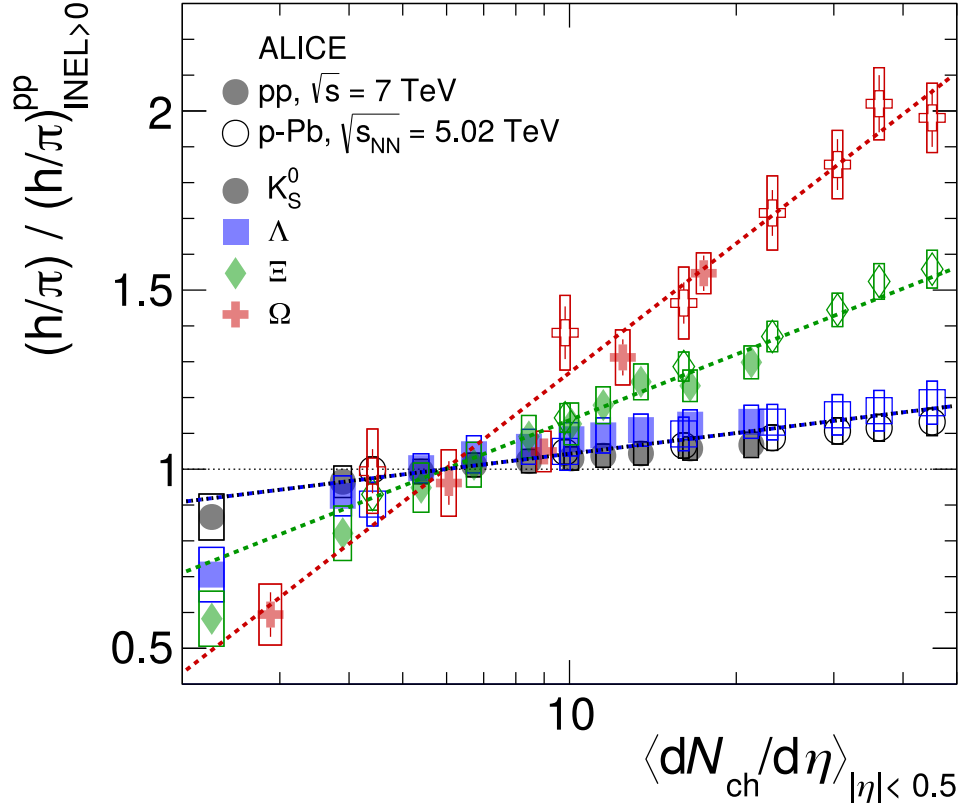


Figure 2.7: Particle yield ratios to pions normalized to the values measured in the inclusive  $INEL > 0$  pp sample. [2]

high-multiplicity pp collisions, where statistics are currently weak, needs to be explored to see if the growth trend will continue or saturation will occur as predicted by the grand canonical statistical model, as observed in the case of Pb-Pb collisions. Also, there is a remarkable similarity in the production of strange particles in pp, p-Pb and Pb-Pb collisions, which is explained by the existence of QGP and it is questioned whether QGP also occurs in proton collisions and not just in heavy ion collisions.

# Chapter 3

## Experiment

The connection between theory and experiment in science is a fundamental aspect of the scientific method and the process of knowledge generation. It is the dynamic interplay between developing theoretical models and conducting empirical experiments to validate, refine or challenge those theories.

Theoretical frameworks are constructed based on mathematical principles, fundamental laws and existing knowledge. These theories aim to explain observed phenomena, make predictions about new phenomena and provide a conceptual framework for understanding the natural world. Experiments, on the other hand, involve the systematic observation and measurement of physical phenomena. Scientists design and conduct experiments to test the predictions or implications of theoretical models. By carefully controlling variables and collecting empirical data, experiments provide evidence to validate or refute theoretical predictions. Experimental results can also uncover unexpected phenomena or inconsistencies that prompt the need for new theoretical developments. This interplay between theory and experiment leads to the advancement of scientific knowledge and a deeper understanding of the world.

The pursuit of knowledge in experimental particle physics is driven by a curiosity to uncover the deep secrets of the Universe. Through the application of fundamental physical principles, experimentalists design, build and operate massive particle accelerators and detectors. These powerful tools allow scientists to recreate and study conditions that mimic the early moments of the Universe, providing insights into the fundamental laws that govern its behavior. Particle accelerators play a central role in experimental particle physics. These colossal machines accelerate charged particles to high energies, enabling them to reach speeds close to the speed of light. By colliding particles at enormous energies, scientists can investigate the physics that governs their interactions, uncovering new particles and understanding their properties. These collisions often generate plenty of subatomic particles that are decaying and are difficult to

catch, requiring sophisticated detectors to capture and analyze them. Detectors are crucial components of particle physics experiments. These instruments are designed to detect and measure the properties of particles produced in high-energy collisions. Detectors come in various forms, employing different detection technologies such as scintillators, calorimeters, tracking devices, etc. By analyzing the particles' trajectories, energies and other characteristics, scientists can unravel the secrets of the subatomic world.

The collaboration between experimental and theoretical physicists is crucial to advancing our understanding of the subatomic world and developing a comprehensive framework that describes fundamental forces and particles. It is impossible to conclude that a theory is correct, if there is no experiment to confirm it. The discoveries made in experimental particle physics have profound implications not only for our understanding of the Universe but also for a wide range of other scientific and technological fields. Many modern technologies, such as medical imaging devices, rely on the advancements made in particle detection and imaging techniques.

### **3.1 The Large Hadron Collider**

The Large Hadron Collider (LHC) is the world's largest and most powerful particle accelerator. Located at the European Organization for Nuclear Research (CERN) near Geneva, Switzerland, the LHC has played a crucial role in advancing our understanding of particle physics since its inception.

The idea for the LHC originated in the 1980s as a response to the need for a more powerful accelerator to explore fundamental particles and the forces of nature. Construction of the LHC began in 1998, involving the collaboration of thousands of scientists, engineers, and technicians from around the world. It took nearly a decade to complete the underground tunnel, which has a circumference of 27 kilometers (Figure 3.1).

On September 10, 2008, a significant milestone was reached when the LHC successfully circulated its first proton beam around the entire accelerator ring. However, just days later, an incident occurred that delayed the full operation of the LHC. After more than a year of repairs and improvements, the LHC resumed operations in November 2009, achieving higher energy levels than any previous accelerator. The primary objective of the LHC was to search for the Higgs boson. On July 4, 2012, CERN announced the discovery of a particle consistent with the Higgs boson, marking a groundbreaking achievement and confirming the existence of this crucial component of the Standard Model. In addition to the Higgs boson, the LHC has been instrumental in the discovery and study of other particles, including the top quark and the pentaquark. It has also provided valuable insights into the properties of neutrinos and the



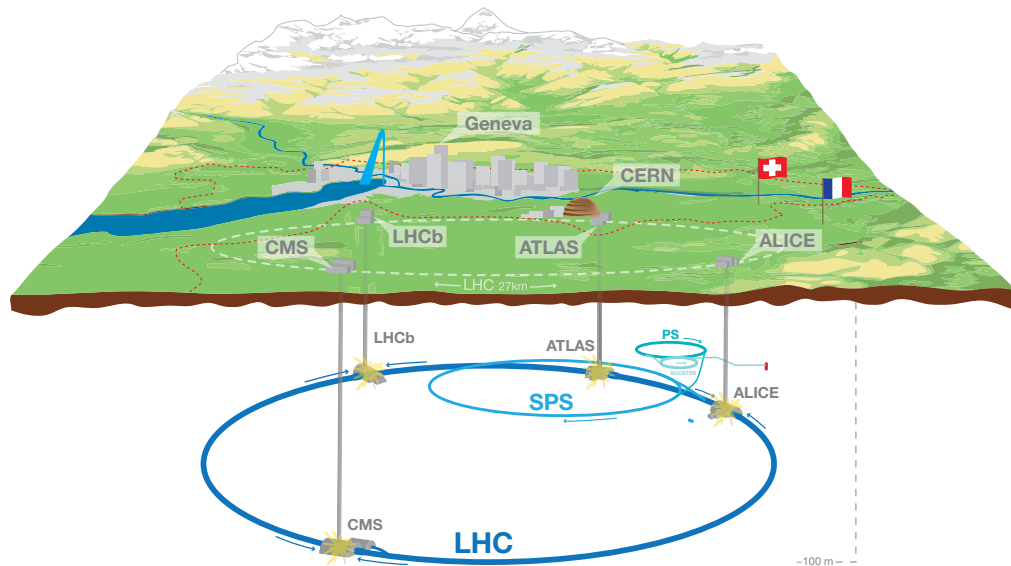


Figure 3.1: Overall view of the LHC, including the ALICE, ATLAS, CMS and LHCb experiments. [39]

behavior of matter at extreme temperatures and densities. Throughout its operation, the LHC has undergone several upgrades to increase its energy levels and particle collision rates. These upgrades have allowed scientists to explore new frontiers of particle physics and look deeper into the mysteries of the Universe.

The LHC operates by accelerating particles in opposite directions and then bringing them into collision at specific interaction points within the detector experiments. When the particles collide, the energy released can create new particles that are short-lived and quickly decay into other particles. Highly sophisticated detectors surrounding the collision points capture and record the characteristics and trajectories of the resulting particles, enabling scientists to analyze the data and draw conclusions about the underlying physics.

The four main experiments that are conducted at the LHC are:

**ATLAS (A Torodial LHC Apparatus)** is the largest general-purpose particle detector mainly studying pp collisions. It is designed to exploit the full potential of the LHC rather than focus on a particular physical process. This approach ensures that it can capture and ana-

lyze any new physical processes or particles that may emerge, enabling a comprehensive exploration of their properties within the framework of the LHC.

**CMS (The Compact Muon Solenoid)** is a general-purpose detector at the LHC. It is used to study a wide range of physical phenomena, from the Standard Model (including the Higgs boson) to searching for extra dimensions and particles that could make up dark matter. It has the same scientific goals as ATLAS, but it uses different detectors and a different magnet-system design.

**LHCb (The Large Hadron Collider beauty experiment)** specializes in investigating the slight differences between matter and antimatter by studying CP violation<sup>1</sup> in the interaction of  $b$  quarks.

**ALICE (A Large Ion Collider Experiment)** is a detector used to study strong interaction through heavy-ion collisions. One of the main topics of ALICE is QGP and its properties. It is the detector used in this work and will be discussed in detail in the next section.

Currently, there are five small experiments at the LHC: the TOTEM experiment (Total Elastic and Diffractive Cross Section Measurement), the LHCf (Large Hadron Collider forward), the MoEDAL (Monopole and Exotics Detector at the LHC), FASER (Forward Search Experiment), and the SND (Scattering and Neutrino Detector). TOTEM measures the total cross section, elastic scattering, and diffraction processes. MoEDAL's prime goal is to search for the magnetic monopole and other highly ionizing stable massive particles and pseudo-stable massive particles. FASER is designed to search for new light and weakly coupled elementary particles, and to detect and study the interactions of high-energy collider neutrinos. SND is built for the detection of collider neutrinos.

Today, the LHC continues to be at the forefront of scientific research, pushing the boundaries of knowledge in particle physics. Its experiments involve an international collaboration of scientists from various countries, fostering a global effort to unravel the mysteries of the Universe. The LHC stands as a testament to humanity's insatiable curiosity and our relentless pursuit of scientific understanding.

### 3.1.1 The CERN accelerator complex

The particle accelerator complex at CERN, schematically shown in Figure 3.2, consists of a series of machines that progressively increase the energy of particles. Each machine raises the

---

<sup>1</sup>CP-symmetry states that the laws of physics should be the same if a particle is interchanged with its antiparticle and the experiment is spatially reflected.

energy of a particle beam before transferring it to the next machine in the sequence. The final machine in this chain is the LHC, where particle beams achieve a remarkable energy of 6.5 TeV per nucleon per beam. The machines and the experiments are continuously upgraded, so this setup is relevant in the year of writing this thesis.

Starting in 2020, Linear accelerator 4 (Linac4) became the source of proton beams for the CERN accelerator complex<sup>2</sup>. It accelerates negative hydrogen ions ( $\text{H}^-$ ) to 160 MeV to prepare them for entry into the Proton Synchrotron Booster (PSB). During the injection from Linac4 to the PSB, the ions lose their two electrons, leaving only protons. These protons are then accelerated to 2 GeV for injection into the Proton Synchrotron (PS), which further boosts the beam's

<sup>2</sup>In the 2018, it was Linac2.

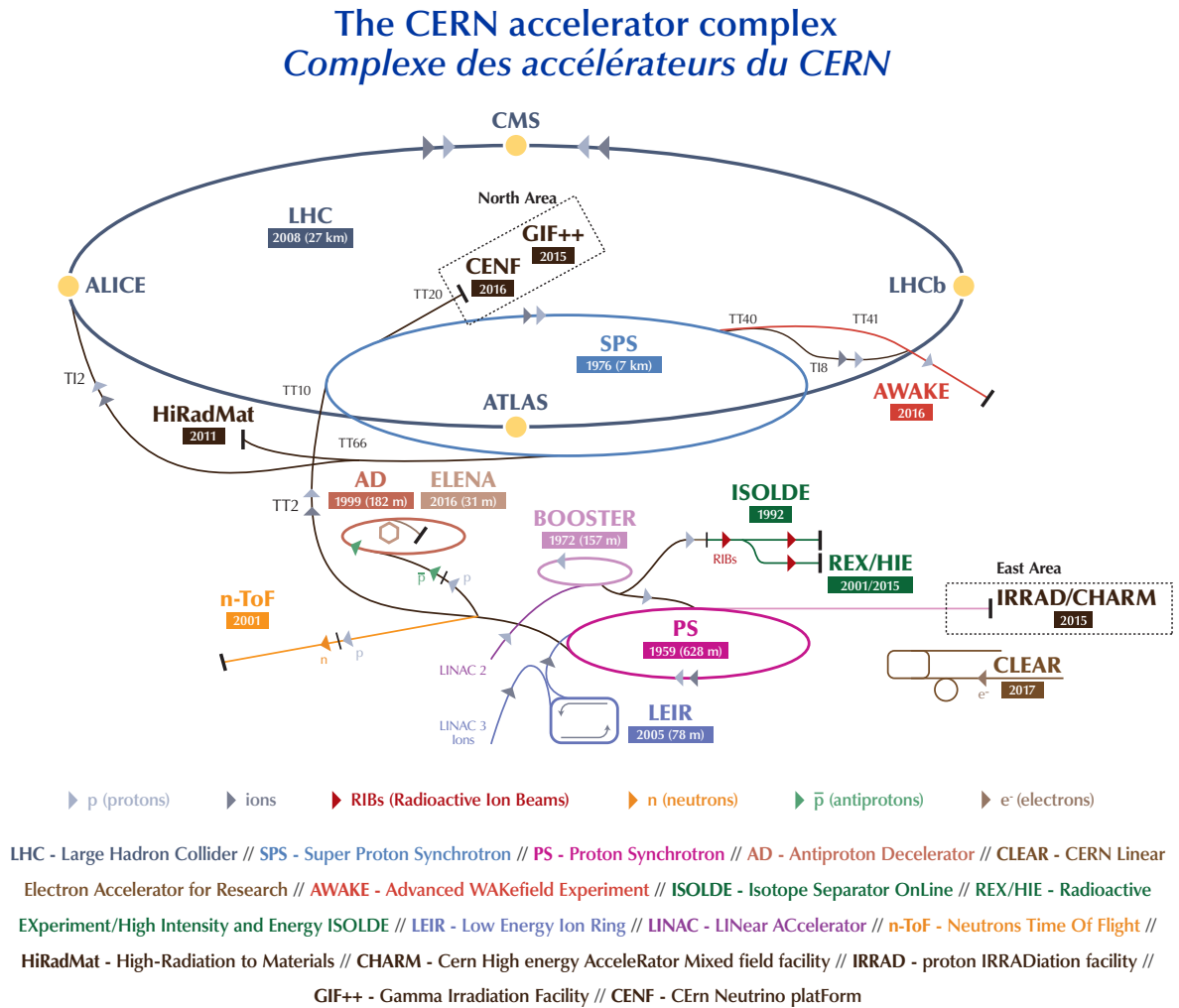


Figure 3.2: A graphic overview of all accelerators in operation at CERN during Run 2. [40]

energy to 26 GeV. The protons are subsequently directed to the Super Proton Synchrotron (SPS), where they reach an energy of up to 450 GeV. The protons are ultimately transferred to the two beam pipes of the LHC, with one beam circulating clockwise and the other anticlockwise. Filling each LHC ring takes approximately 4 minutes and 20 seconds, while it takes 20 minutes for the protons to achieve their maximum energy of 6.5 TeV. Under normal operating conditions, the beams circulate inside the LHC beam pipes for many hours. Inside the LHC, the two beams collide within four main detectors (ALICE, ATLAS, CMS, and LHCb) where the total collision energy amounts to 13 TeV. In addition to protons, the LHC also accelerates lead ions. The lead ions originate from vaporized lead and enter Linac3 before being collected and accelerated in the Low Energy Ion Ring (LEIR). They follow the same path as protons to reach their maximum energy in the LHC.

### 3.1.2 Magnets

Without external forces, the accelerated particles would disperse and continue in a straight line due to their momentum. To prevent this, over 50 types of magnets are employed to guide the particles along intricate paths while maintaining their speed. All magnets in the LHC are electromagnets. The primary dipoles produce magnetic fields of 8.3 T, which are more than 100,000 times stronger than Earth's magnetic field. These electromagnets utilize a current of 11,080 A to generate the magnetic field. By using a superconducting coil, the high currents can flow without any loss of energy due to electrical resistance. The standard cross section of the LHC dipole magnet can be seen in Figure 3.3.

The dipole magnets are responsible for bending the paths of the particles. They generate powerful magnetic fields that enable the beam to navigate turns. To enhance the chances of particle collisions within the LHC detectors, the particles are tightly grouped together. Quadrupole magnets aid in maintaining a compact beam. These magnets possess four magnetic poles symmetrically arranged around the beam pipe, enabling them to compress the beam either vertically or horizontally. Additionally, LHC is equipped with sextupole, octupole, and decapole magnets. These magnets address minor imperfections in the magnetic field at the ends of the dipoles, ensuring more precise control over particle trajectories.

Upon entering the detectors, insertion magnets take control of particle beams. These magnets are responsible for squeezing the particles closer together, allowing collisions with particles approaching from the opposite direction. To achieve this, three quadrupoles form an inner triplet system. There are eight inner triplets, with two located at each of the four primary LHC detectors. The inner triplets significantly narrow the beam, reducing its width from 0.2 mm to 16  $\mu\text{m}$ , making it 12.5 times narrower.

After the collision, dipole magnets separate the particle beams, while other magnets minimize the dispersion of particles resulting from the collisions. When it becomes necessary to dispose of the particles, they are deflected from the LHC along a straight path towards the beam dump. A „dilution” magnet reduces the beam intensity by a factor of 100 000 before the beam collides with a block made of concrete and graphite composite, bringing it to a final halt. Additionally, insertion magnets are responsible for beam cleaning operations, which ensure that stray particles do not come into contact with the LHC’s most sensitive components.

### 3.1.3 Radiofrequency cavities

Particle accelerators use metallic chambers called radiofrequency cavities (RF) to accelerate charged particles. These cavities contain an electromagnetic field generated by high-power klystrons, which are tubes with modulated electron beams. In the LHC, there are 16 RF cavities

#### LHC DIPOLE : STANDARD CROSS-SECTION

CERN AC/DI/MM - HE107 - 30 04 1999

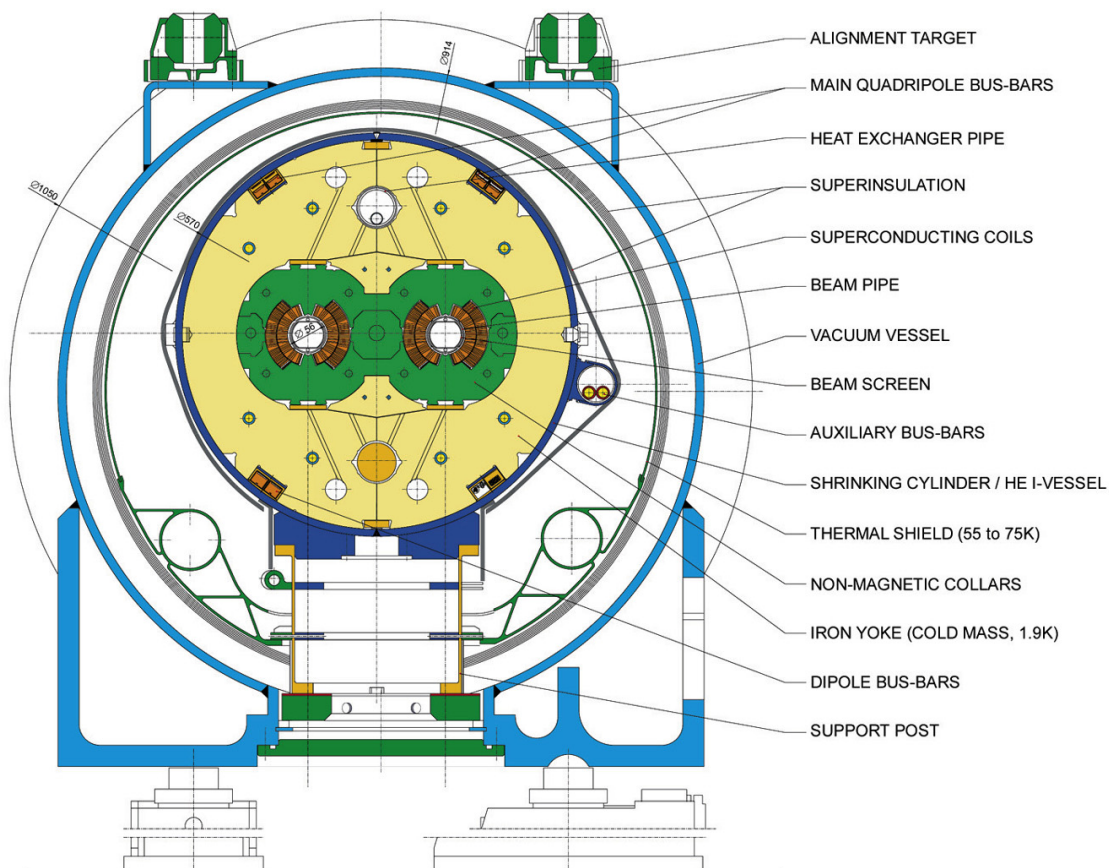


Figure 3.3: Cross section of the LHC Main Dipole in its cryostat. [41]

housed in superconducting cryomodules. The cavities operate at a frequency of 400 MHz and can reach a maximum voltage of 2 megavolts (MV), resulting in a total of 16 MV per beam. The design of the cavities ensures resonance and the buildup of electromagnetic waves' intensity. A waveguide directs energy from the klystrons to the cavities.

The RF cavities in the LHC increase the energy of particles from 450 GeV to 6.5 TeV. This energy increase occurs as the particles pass through the RF cavities more than 10 million times, reaching maximum energy in approximately 20 minutes. The RF cavities oscillate at a frequency of 400 MHz and precise timing of particle arrival is crucial. Protons with slightly different energies arriving earlier or later are either accelerated or decelerated to maintain proximity to the desired energy level. This sorting process organizes the particle beam into packs called „bunches”.

#### 3.1.4 Cryogenics

The use of superconducting materials has proven to be the best way of avoiding overheating in the coils and of keeping them as small as possible. To maintain a low temperature, the LHC relies on a cryogenic system that requires 40,000 leak-tight pipe seals and 120 tons of helium.

Cryogenic systems are essential for enabling superconductivity in the LHC. The niobium-titanium (NbTi) wires in the coils of the superconducting magnets require low temperatures to achieve a superconducting state. To maintain these low temperatures, the LHC utilizes a closed liquid-helium circuit, which keeps the superconducting magnets at 1.9 K. Cryogenic techniques not only cool the superconducting magnets but also serve other purposes in particle detectors. They are used to keep heavy gases like argon or krypton in a liquid state for detecting particles in calorimeters and other applications. Overall, cryogenic systems play a crucial role in maintaining the necessary conditions for superconductivity and particle detection in various components of the LHC.

#### 3.1.5 Vacuum systems

The LHC features three distinct vacuum systems: one for the beam pipes, one for insulating the cryogenically cooled magnets, and one for insulating the helium distribution line. The beam pipes require a vacuum environment to prevent collisions with gas molecules, maintaining a space as empty as interstellar space. In the cryomagnets and the helium distribution line, the vacuum serves as a thermal insulator. It helps minimize heat transfer from the surrounding room-temperature environment into the cryogenic components.

The pipes through which particle beams travel in the LHC require an ultra-high vacuum.

This includes 48 km of arc sections, maintained at 1.9 K, and 6 km of straight sections at room temperature, housing beam-control systems and experiment insertion regions. In the arc sections, an ultra-high vacuum is achieved through cryogenic pumping, which involves removing approximately 9000 cubic meters of gas. As the beam pipes are cooled to extremely low temperatures, gases condense and adhere to the pipe walls through adsorption. It takes nearly two weeks of pumping to reduce the pressures to below  $10^{-10}$  mbar. This meticulous process ensures a clean and particle-free environment for the particle beams to travel through the LHC.

## 3.2 A Large Ion Collider Experiment

In March 1993, a proposal was put forth for ALICE (A Large Ion Collider Experiment), which aimed to be a specialized experiment focused on studying heavy-ion collisions at the LHC. Its primary objective was to investigate the presence of QCD bulk matter and the QGP. As the only detector dedicated to QGP research, ALICE was designed to examine a wide range of specific observables across varying transverse momentum values. Its goal was to provide insights into the different stages of heavy-ion collisions, starting from the initial state and progressing through the QGP phase until the transition to hadronic matter. Additionally, from the very beginning, the ALICE program included aspects of pp physics, which gradually grew in significance.

### THE ALICE DETECTOR

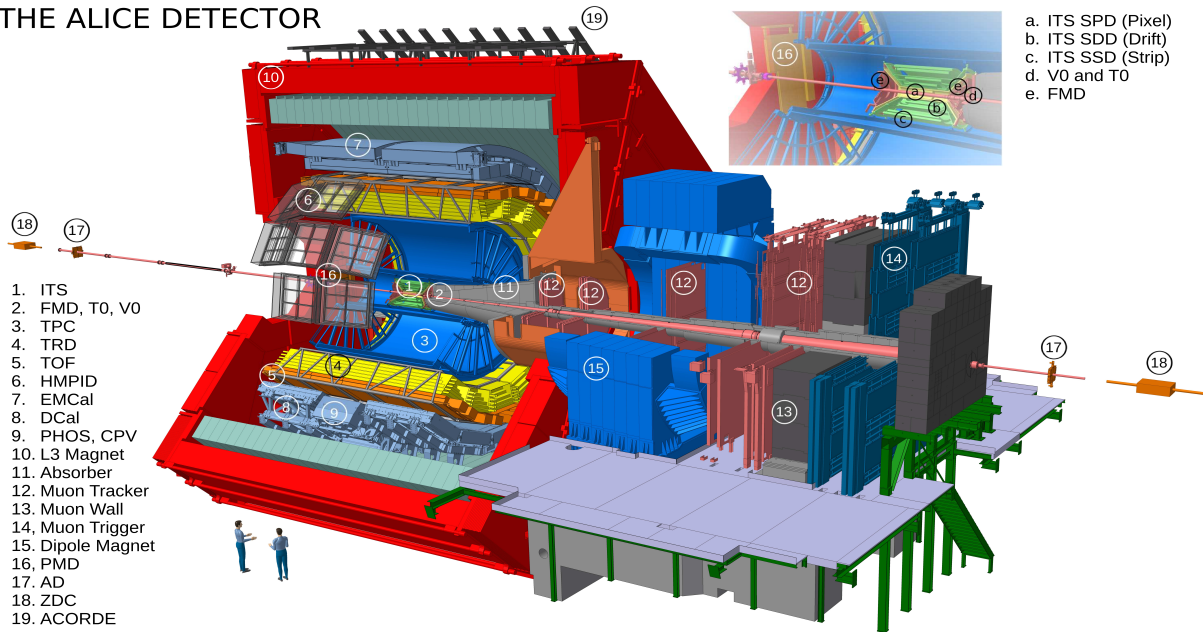


Figure 3.4: Schematics of ALICE during Run 2. [42]

ALICE initiated the collection of physics data in 2009, starting with the first LHC pp collisions at a center-of-mass energy of 0.9 TeV. Since then, it has gathered data from various collision systems and energies throughout Run 1 (2009-2013) and Run 2 (2015-2018). Notably, Pb-Pb collisions were conducted in 2010 and 2011 at a center-of-mass energy per nucleon pair of 2.76 TeV, as well as in 2015 and 2018 at 5.02 TeV. A brief run involving Xe-Xe collisions at 5.44 TeV was also carried out in 2017. Proton-proton collisions at the same energies as Pb-Pb were performed over the years, serving as a reference for nucleus-nucleus reactions and enabling specific QCD studies. To investigate the effects of cold nuclear matter, ALICE conducted p-Pb collisions in 2013 and 2016 at 5.02 and 8.16 TeV, following a preliminary run in 2012. Additionally, ALICE has gathered pp data at all other available collision energies over the years, extending up to 13 TeV. [43]

The ALICE detector is a 10 000 ton detector, located at the interaction point IP2 of the LHC. It consists of a central barrel that covers the full azimuth and the pseudorapidity region  $|\eta| \leq 0.9$ . This configuration enables the detector to offer reliable particle identification up to a transverse momentum of about 20 GeV/ $c$ . It also has a remarkably low momentum cut-off and exceptional abilities for reconstructing primary and secondary vertices. Its primary detectors for particle identification are the Inner Tracking System (ITS) and a sizable Time Projection Chamber (TPC). It is composed of many sub-detectors, as shown in Figure 3.4. The most important ones are going to be described in the text below. The detectors are described as they were in Run 2, when the data used in the thesis was collected.

### 3.2.1 Barrel detectors

To track the particles formed after the collision, a collection of cylindrical barrel detectors encloses the designated interaction point. These detectors, including the Inner Tracking System, the Time Projection Chamber, and the Transition Radiation Detector (TRD), capture multiple measurements along the path of each charged particle, enabling accurate trajectory analysis. The ALICE is positioned within a magnetic field of 0.5 T generated by an immense magnetic solenoid, where the bent trajectories of the charged particles are used to determine their momenta.

#### The Inner Tracking System (ITS)

The primary objective of this system is to detect and study the decay of short-lived heavy particles, which only travel a very short distance before decaying. To accomplish this, the system employs precise measurements of the decay location with an accuracy of one-tenth of a mil-



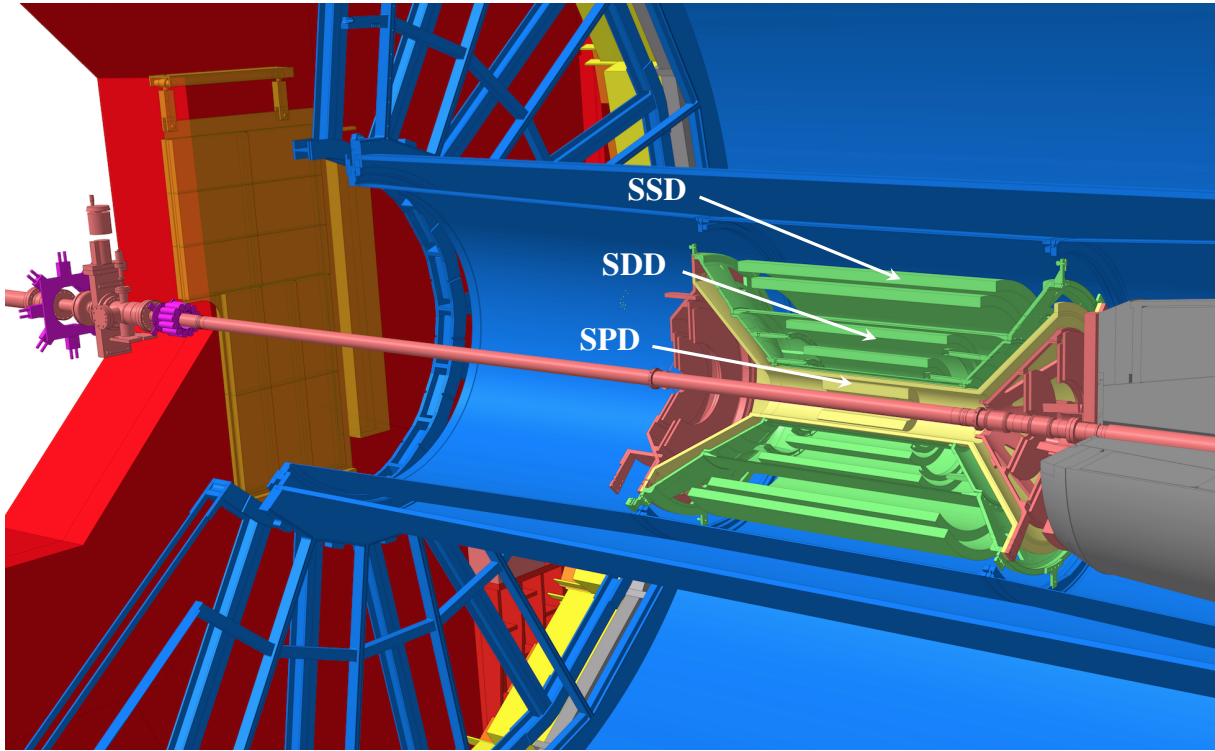


Figure 3.5: ITS schematics during Run 2. [42]

limeter. The ITS consists of six cylindrical layers comprising silicon detectors. Starting from the interaction point, there are two layers of SPD (Silicon Pixel Detector), two layers of SDD (Silicon Drift Detector) and two layers of SSD (Silicon Strip Detector), as shown in Figure 3.5. Positioned around the collision point, these layers enable precise measurement of the location of the primary vertex and the properties of particles produced from the collisions, accurately pinpointing their path to within a fraction of a millimeter.

By utilizing the ITS, it becomes possible to identify particles containing strange and heavy quarks by reconstructing the coordinates at which their decay occurs, so called secondary vertices. It is also used for improving angle and momentum resolution, and identifying low momentum particles.

### The Time Projection Chamber (TPC)

The TPC is the main particle tracking detector within the ALICE experiment. As schematically shown in Figure 3.4, it is a large cylinder filled with a Ne-CO<sub>2</sub>-N<sub>2</sub> gas mixture, that is serving as a detection medium. Charged particles passing through the TPC cause ionization of the gas atoms along their path, resulting in the release of drifting electrons towards the detector end plates. The ionization process characteristics are then used for particle identification. The

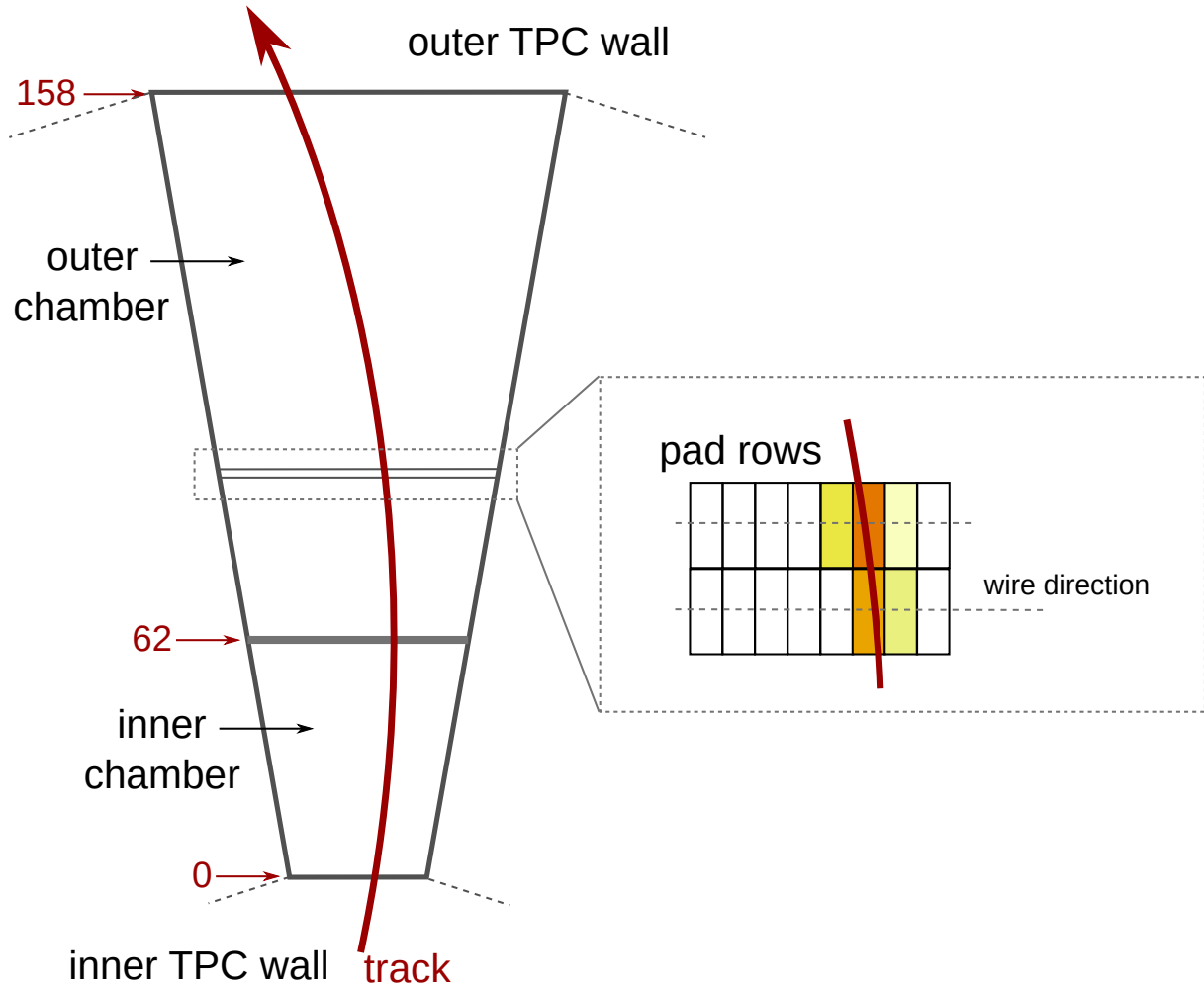


Figure 3.6: Illustration of one TPC readout segment. [44]

ionization strength dependence on particle velocity is given by the Bethe-Bloch formula, which describes the average energy loss of charged particles in a medium.

Multi-wire proportional counters were used as the detection medium due to their ability to provide signals with pulse heights proportional to the ionization strength. Signal amplification is achieved through an avalanche effect near the anode wires situated in the readout chambers. The positive ions generated in the avalanche induce a positive current signal on the pad plane. The readout process involves the use of 557 568 pads forming the cathode plane of the multi-wire proportional chambers (MWPC) located at the end plates. This allows for the determination of the radial distance to the beam and the azimuth. An illustration of one end plate with one row of pads is shown in Figure 3.6. The third coordinate  $z$ , along the beam direction, is obtained from the drift time.

The TPC's volume is mostly sensitive to charged particles passing through it, while keep-

ing the material budget to a minimum. Its straightforward pattern recognition, which involves continuous tracks, makes TPCs ideal for high-multiplicity environments like heavy-ion collisions, where tracking thousands of particles simultaneously is necessary. Within the ALICE TPC, tracks are sampled up to 159 times, resulting in an ionization measurement resolution as precise as 5%.

### **The Transition Radiation Detector (TRD)**

The ALICE experiment uses a TRD detector to discriminate between different types of charged particles at high momenta. It uses transition radiation (TR) which is emitted when a charged particle passes between two materials. Below 1 GeV/c, electrons are identified through a combination of measurements from the TPC and time of flight (TOF). For momenta in the range of 1-10 GeV/c, the TRD takes advantage of the emission of TR when electrons pass through a dedicated „radiator”, consisting of many layers of thin materials with different dielectric constants. This generates TR photons in the X-ray range, which are detected by MWPCs filled with a Xe-CO<sub>2</sub> gas mixture, depositing their energy on top of the ionization signals from the particle track.

The main purpose of ALICE TRD is to identify electrons and positrons, and to provide a fast trigger for charged particles with high momentum. Also, it is used in track reconstruction and calibration.

### **3.2.2 Particle Identification**

To identify a stable charged particle, its mass and charge must be determined. The mass is determined using measurements of momentum and velocity. The particle momentum and charge sign are obtained by analyzing the curvature of its track in a magnetic field. Particle velocity is derived using four methods involving time-of-flight, ionization, transition radiation, and Cherenkov radiation measurements. Each method performs well in different momentum ranges for specific particle types. In ALICE, these methods can be combined to measure particle spectra effectively. Apart from the information provided by the ITS and the TPC, additional specialized detectors are necessary to enhance particle identification in the ALICE experiment, such as the Time-Of-Flight (TOF) and the High Momentum Particle Identification Detector (HMIP).

#### **The Time-Of-Flight detector (TOF)**

The TOF measurements in ALICE determine the velocity of a charged particle by accurately measuring the time taken by particles to travel from the collision point to the TOF detector. By

combining this TOF data with tracking information from other detectors, each track is identified, and when the momentum is known, the particle mass can be determined. The ALICE TOF detector utilizes multigap resistive plate chambers (MRPCs), which are parallel-plate detectors constructed with thin sheets of standard window glass to create narrow gas gaps with high electric fields. Fishing lines are used to separate these plates, providing the required spacing. To achieve a detection efficiency close to 100%, each MRPC consists of 10 gas gaps. Positioned at a distance of 3.7 meters from the beam line, the TOF detector is located just outside the TRD detector.

### **The High Momentum Particle Identification Detector (HMPID)**

The HMPID is a specialized ring-imaging Cherenkov (RICH) detector designed to identify the speed of particles beyond the momentum range covered by energy loss measurements in ITS and TPC ( $p = 600$  MeV), as well as time-of-flight measurements. Cherenkov radiation is a shock wave produced when charged particles move through a material at a speed greater than the speed of light in that material. Only a thin radiator layer of a few centimeters is needed to emit enough Cherenkov photons if a medium is dense (large refractive index) enough. The photon detector is positioned at a distance of about 10 cm behind the radiator. This setup allows the cone of light to spread out, creating the distinctive ring-shaped image characteristic of Cherenkov radiation detection. The ALICE HMPID is the world's largest caesium iodide RICH detector and has a momentum range of up to 3 GeV for distinguishing pions and kaons and up to 5 GeV for distinguishing kaons and protons.

### **3.2.3 Calorimeters**

Particle energy is measured using calorimeters, as all particles except muons and neutrinos deposit all their energy in the calorimeter system through the production of electromagnetic or hadronic showers (Figure 3.7). Photons, electrons, and positrons deposit all their energy in an electromagnetic calorimeter, and their showers appear identical. However, photons can be distinguished by the absence of a track in the tracking system associated with the shower. The photons carry information about the system's temperature, but special detectors are required to measure them accurately.

#### **The Electro-Magnetic Calorimeter (EMCal)**

The EMCal enhances ALICE's capabilities to measure high-energy photons, electrons, neutral pions, and particle jets, as well as their correlations. Inside the EMCal, particle energy

is proportionally converted into detectable light. Charged particles primarily lose their energy through bremsstrahlung<sup>3</sup>, while high-energy photons lose energy via electron-positron pair creation. The EMCal is a lead-scintillator sampling calorimeter consisting of 100 000 individual scintillator tiles and 185 kilometers of optical fiber, with a total weight of approximately 100 tons. The EMCal covers almost the entire length of the TPC and the central detector, while one-third of its azimuth is positioned back-to-back with the PHOS. It enables the complete reconstruction of high-energy jets, so it is used for the study of specific hard processes and enhances the measurement precision of high-energy photons and electrons.

### The Photon Spectrometer (PHOS)

The PHOS is a high-resolution electromagnetic calorimeter installed in ALICE to study the initial phase of the collision by measuring photons directly from the collision. It covers a

<sup>3</sup>Bremsstrahlung is radiation produced by the deceleration of charged particles. In this case, it happens because of collisions with Pb nuclei.

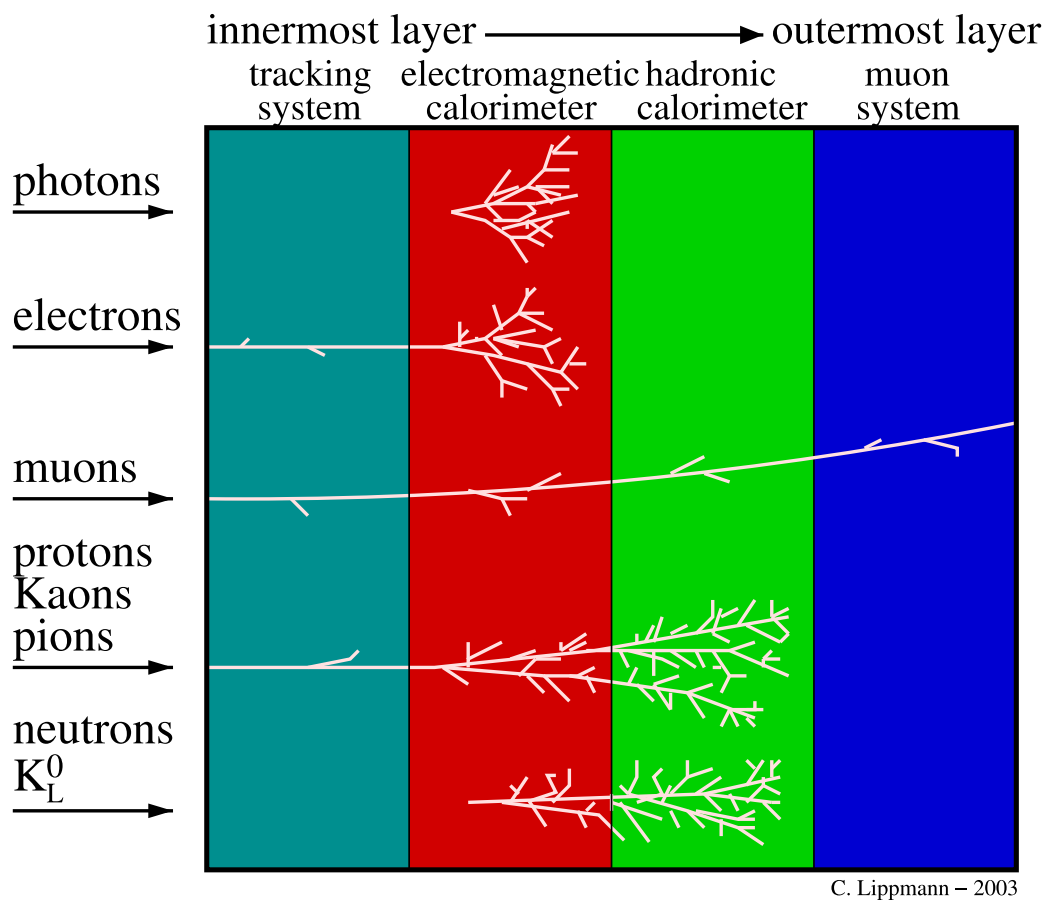


Figure 3.7: Illustration of different types of calorimeters and particles passing through them. [45]

limited acceptance domain at central rapidity<sup>4</sup> and consists of lead tungstate crystals, read out using Avalanche Photodiodes (APD). When high-energy photons hit lead tungstate, they cause it to glow or scintillate, allowing their measurement. Due to its extreme density, lead tungstate effectively stops most photons that reach it, making it an ideal material for photon detection.

### **The Photon Multiplicity Detector (PMD)**

The PMD is a particle shower detector designed to measure the number and distribution of photons produced in collisions. It includes a veto detector as its first layer to filter out charged particles. Photons, however, pass through a converter, generating an electromagnetic shower in a second detector layer, leading to substantial signals in multiple cells. In contrast, hadrons typically affect only one cell and produce signals corresponding to minimum-ionizing particles.

### **The muon spectrometer**

The ALICE muon spectrometer focuses on studying the complete spectrum of heavy quarkonia by observing their decay into the muon-antimuon channel. These heavy quarkonium states play a crucial role in investigating the early and hot stage of heavy-ion collisions, particularly the formation of QGP. In the presence of QGP, quarkonium states experience dissociation due to color screening, resulting in a suppression of their production rates. At the high collision energy of the LHC, both charmonium and bottomonium states can be explored and studied.

Muons are the only charged particles capable of passing almost undisturbed through any material. This is because muons with momenta below a few hundred GeV/ $c$  do not experience radiative energy losses and, therefore, do not produce electromagnetic showers. Additionally, being leptons, muons are not subject to strong interactions with the nuclei of the material they traverse. This behavior is utilized in muon spectrometers in high-energy physics experiments by placing muon detectors behind calorimeter systems or thick absorber materials. All charged particles other than muons are completely stopped, so any signal produced inside the muon spectrometer must correspond to a muon.

## **3.2.4 Forward detectors**

In the region of high pseudorapidity, there are small and specialized detectors used to determine global characteristics of the collisions. Their position is just around the beam pipe, meaning that they can be used for triggering and detecting the spectators (particles that didn't collide).

---

<sup>4</sup>Central rapidity is located around the interaction point, perpendicular to the beam axis.

**The Forward Multiplicity Detector (FMD)**

The FMD system's primary role is to provide information about charged particle multiplicities in the forward region. When combined with the pixel system of the ITS, the FMD covers the full range of pseudorapidity for all beam combinations. The FMD's segmentation and overlap with the ITS inner pixel layer provide redundancy and serve as important checks for analysis procedures. Additionally, the detector's segmentation enables the study of multiplicity fluctuations and the determination of the reaction plane on an event-by-event basis.

**The Zero Degree Calorimeter (ZDC)**

The ZDCs are calorimeters that detect the energy of spectator nucleons to determine the overlap region of colliding nuclei. There are four calorimeters in total: two to detect protons (ZP) and two to detect neutrons (ZN). They are located 115 m away from the interaction point on both sides, precisely along the beam line. The ZN is positioned at zero degrees with respect to the LHC beam axis, placed between the two beam pipes, hence the name Zero Degree Calorimeter. The ZP is positioned externally to the outgoing beam pipe. These calorimeters operate by detecting Cherenkov light produced by the charged particles.

**The V0 Detector**

The V0 detector in ALICE consists of two arrays of scintillator counters, V0-A and V0-C, positioned on both sides of the interaction point. V0-C is placed upstream of the muon absorber and covers the spectrometer acceptance, while V0-A is located around 3.5 meters away from the collision vertex on the opposite side. It is used to estimate the collision centrality by summing up the energy deposited in the two disks of V0, which is directly related to the number of primary particles produced in the collision and, therefore, the centrality of the event. Additionally, it provides minimum-bias triggers and serves as a reference in Van Der Meer scans, which provide information about the size and shape of the colliding beams and the delivered luminosity to the experiment.

**The T0 Detector**

The T0 detector measures the accurate interaction time as the reference signal for the TOF detector, aiding in particle identification. Also, T0 supplies five different trigger signals to the Central Trigger Processor, with the T0 vertex being the most crucial. The T0 vertex confirms the location of the primary interaction point along the beam axis promptly and accurately within predefined boundaries. Additionally, the T0 detector is used for online luminosity monitoring,

providing rapid feedback to the accelerator team. The T0 consists of two arrays of Cherenkov counters, T0-A and T0-C, located at opposite sides of the interaction point.

### 3.2.5 ALICE Cosmic Rays Detector (ACORDE)

The ALICE cavern serves as an ideal location to detect high-energy atmospheric muons generated by cosmic ray showers. The ACORDE is an array of scintillators that triggers the detection of cosmic ray showers by detecting the arrival of muons at the top of the ALICE magnet.

## 3.3 ALICE online systems

After the collision inside the ALICE, the signals from the detectors need to be collected to form an event that is stored in permanent storage, so it can later be accessed and used for various analyses. This process is challenging because collisions generate a substantial volume of data, and not all of this data is relevant or practical for use in analyses. For this reason, ALICE employs five online<sup>5</sup> systems [46]:

**The Trigger system (TRG)** is merging the information from all triggering detectors and, for each bunch-crossing of the LHC, quickly determining whether the resulting data are usable. Within microseconds, a decision is made, and for every positive decision, a series of trigger signals is sent to all detectors to enable synchronous readout.

**Data Acquisition (DAQ) system** is managing the data flow from the detector to the data storage. Additionally, the DAQ system incorporates software packages responsible for monitoring data quality and system performance.

**The High-Level Trigger (HLT)** performs detailed online analysis on almost complete events. Its primary function is to select or reject events and reduce the event size by either reading out only a portion of the data (region of interest) or compressing the entire event information.

**The Detector Control System (DCS)** is responsible for controlling all the detector services, such as high- and low-voltage power supplies, gas, magnets, cooling, and more.

**The Experiment Control System (ECS)** is a piece of software that ensures the coordination of all online systems on each detector. It is also providing operators with a unified view

---

<sup>5</sup>Online means that programs and actions run in real time.



of the experiment, serving as a central point for overseeing experiment operations and enabling independent activities on different parts of the experiment at the detector level, allowing different operators to carry out their tasks simultaneously.

The data flow from raw data to reconstructed events is shown schematically in Figure 3.8. Raw data from detectors is processed by Local Data Concentrators (LDCs) where it is assembled into sub-events. These sub-events are then transferred to Global Data Collectors (GDCs) where they are formed into a complete event. Publish agent then registers events into the AliEn system, so they can get stored on disks and then permanently stored on tapes by the CERN advanced storage manager (CASTOR).

During data-taking, the detectors also gather condition data, which is essential for calibrating individual detector signals. Conditions data includes information about the detector status and environmental variables during data-taking, such as inactive and noisy channel maps, response distributions, temperatures, pressure, and detector configurations. While many of these conditions could be calculated from the raw data and extracted offline after data-taking, it is

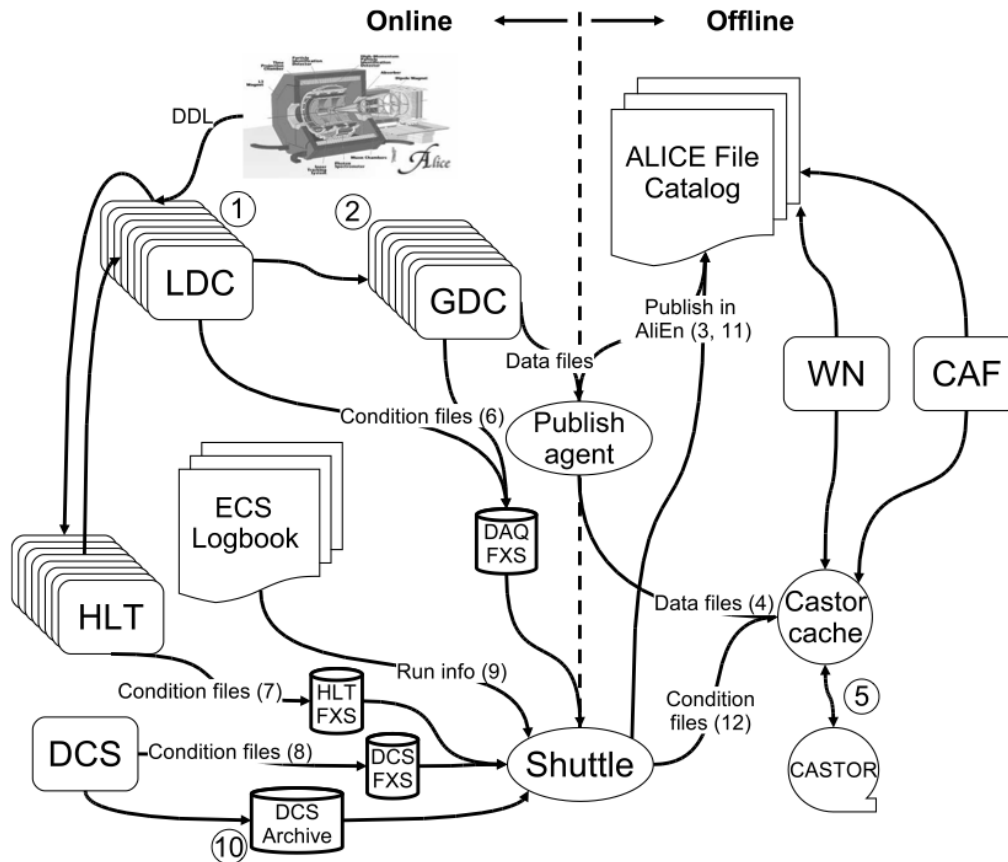


Figure 3.8: Schematic view of ALICE data flow. [47]

not feasible due to limited computing resources. Hence, condition data is extracted during data-taking and stored in the Offline Condition Data Base (OCDB).

A dedicated program called Shuttle collects these outputs and makes them available for reconstruction. It also retrieves run information from the ECS logbook and continuously monitors values from the DCS Archive. After processing the data, the Shuttle registers the produced condition files in AliEn and stores the data in CASTOR. [47]

## 3.4 ALICE offline software

The offline software is needed to develop and manage the data processing framework for various tasks, including simulation, reconstruction, calibration, alignment, visualization, and analysis. These tasks are crucial in the final stages of the experimental process as they help interpret the data collected by the experiment and extract relevant physics information. Due to the complexity and scale of the ALICE experiment, the software is involved in operating a wide range of environments to accomplish these tasks.

### 3.4.1 Grid

The processing and analysis of raw data and the simulation of events demand more computing resources than individual institutes or centers like CERN can provide alone. As a result, collaboration member institutes also contribute storage and computing capabilities. Manual data distribution for reconstruction and analysis is impractical, so there was a need for an automated system. The decentralized computing model known as Grid was a solution to this problem.

Since 2001, ALICE has been using AliEn, a Grid middleware service. Users interact with the Grid through the AliEn User Interface and available services are a combination of AliEn Middleware, which offers high-level or ALICE-specific services, and the middleware installed on the computing centers, which provides basic services.

### 3.4.2 AliRoot

The ALICE offline framework, AliRoot, is built on Object-Oriented programming techniques and is supported by the ROOT system. It also utilizes the AliEn system to access the computing Grid. These technical decisions have led to a unified framework, entirely written in C++, while still incorporating some external programs written in FORTRAN, that are hidden from users.

The AliRoot framework has been continuously developed since 1998 and serves multiple purposes, including simulation, alignment, calibration, reconstruction, visualization, and analy-

sis of experimental data. It played a crucial role in performing simulation studies for the Technical Design Reports of all ALICE subsystems, optimizing their design. Additionally, during the preparation phase before data collection, AliRoot was used to evaluate the physics performance of the complete ALICE detector and assess various experimental scenarios.

The offline framework was designed to efficiently simulate various collision types, such as nucleus-nucleus, proton-nucleus, and proton-proton, and to provide precise predictions of detector responses. Multiple Monte Carlo event generators like Pythia, Phojet, and HIJING are integrated with AliRoot to generate particles, storing information such as type, momentum, charge, production process, origin, and decay products in a kinematics tree file.

The simulation process involves using programs like Geant3, Geant4, and Fluka to model the detector's structure, particle motion, and interactions with the material. For interactions with sensitive detector parts, information such as position, time, energy deposition, and the corresponding track's tag is recorded as hits.

Finally, these hits are transformed into the detector's digital output, considering the detector's response function. All this information is then stored in the detector's specific hardware format as raw data.

### 3.4.3 Reconstruction of events

The ALICE reconstruction code is part of the AliRoot framework. For event reconstruction, it takes digits from the detector as input along with additional information like module number, readout channel number, time bucket number, etc. The input can be in either a special ROOT format, convenient for development and debugging, or raw data format, as produced by the real detector or generated from simulated special-format digits.

The output of the reconstruction process is stored in the ESD (Event Summary Data format). It contains information about reconstructed charged particle tracks, including particle identification details, as well as decays. This ESD data can be further reduced to get Analysis-Object data (AOD), which contains only the information needed for analysis.

Reconstruction is the same for simulated and real events and consists of the following steps:

**Cluster finding** is reconstructing space points where the particles left their signal for a specific detector. Particles that interact with a detector create a signal for several detecting elements, so the first step of reconstruction is finding clusters of signals to eliminate random noise.

**Track reconstruction and particle identification** is based on the Kalman filter approach, as shown in Figure 3.9. The track reconstruction process begins by identifying track „seeds”

in the outermost part of the TPC, assuming they originated from the primary vertex. The reconstruction then proceeds with a similar seeding in the innermost part of the TPC, followed by the removal of clusters already associated with tracks. The final filtering is performed without requiring the seeds to point to the primary vertex. Afterward, the track information is supplemented with data from other detectors such as ITS, TRD, TOF, HMPID, and PHOS, if the track is within their acceptance regions. This results in the formation of „global tracks”. Combining particle identification information from outer detectors (TRD, TOF, HMPID) and  $dE/dx$  measurements obtained from TPC and ITS, enables the identification of charged particles. For neutral particles in the central-rapidity region, identification is done using calorimeters (PHOS and EMCAL). Additionally, in the forward region, photons can be counted using the PMD.

**Primary vertex reconstruction** is done using different methods with the help of information such as tracklets from ITS, tracks from TPC and global tracks. After estimating the position of the primary vertex, it is then used for constraining tracks during the reconstruction procedure.

**Secondary vertex reconstruction** is done to find positions where unstable particles decayed, like cascades for example. This reconstruction is based on geometry, which is determined by the topology of the decay.

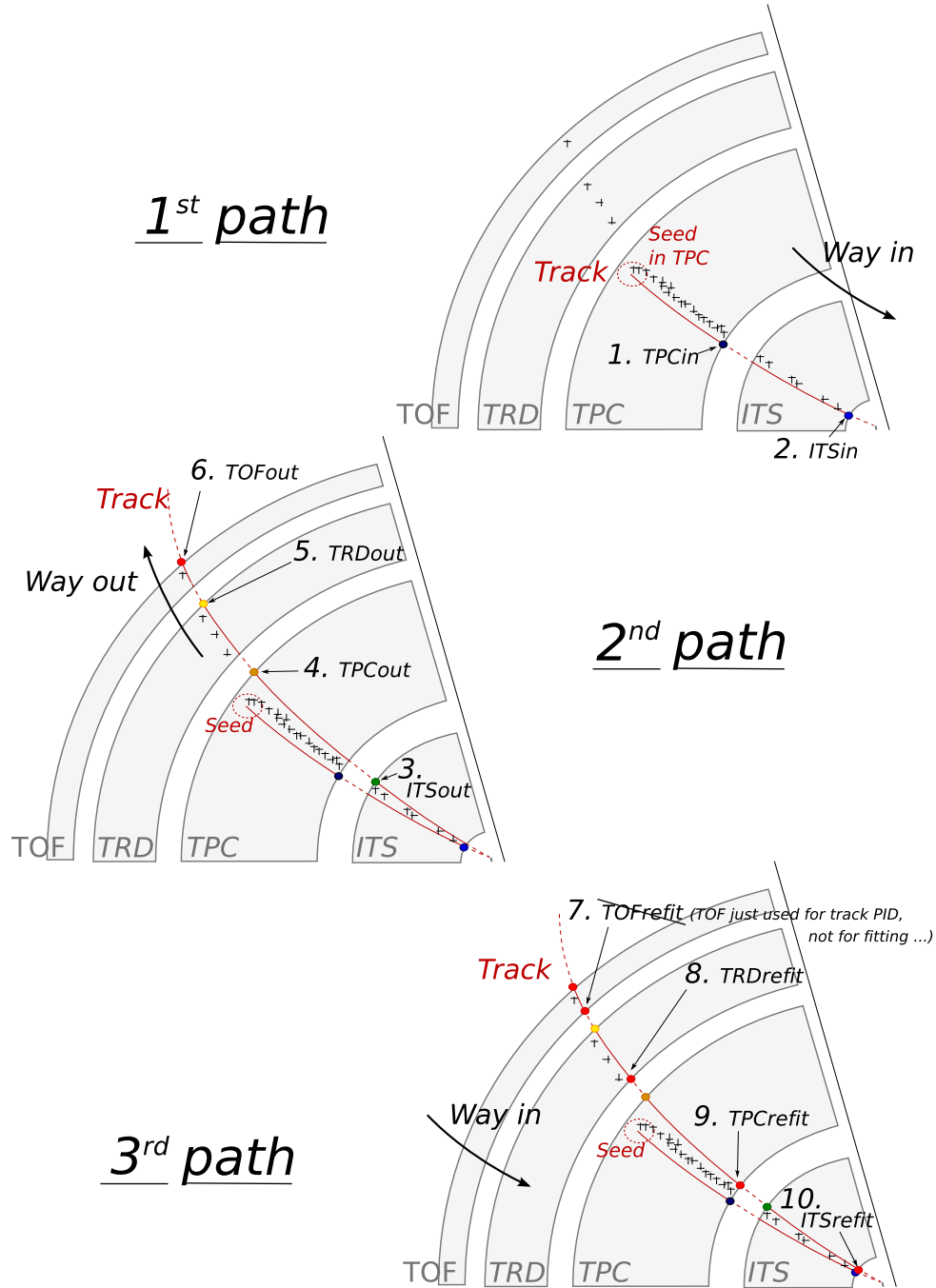


Figure 3.9: Principles of tracking for an ALICE event using Kalman filter approach. [48]

# Chapter 4

## Methodology

To extract the number of produced  $\Xi$  and  $\Omega$  hyperons from the raw signal, some selection needs to be performed. This involves selecting events (collisions) with the right properties and then extracting candidates that exhibit the properties of our desired particles. The selection procedure for events and candidates is already well defined and has been tested many times, as this is not the first analysis searching for multi-strange baryons conducted using ALICE data. The results from the last analysis conducted on this topic of research were published in 2020 in [1], and this analysis follows its steps.

To ensure that the analysis in this thesis produces the expected results, it is performed on two sets of data. One is the main topic of research, while the other is used as a check to be compared with previous results, thereby ensuring that no mistakes are made in the analysis procedure.

This chapter explains all analysis steps in detail, comprising five main sections: Data and MC, Cascade reconstruction, Analysis details, Comparison with published results, and Systematic uncertainties. First, details about data and event selections are provided. Following that, the theoretical background for reconstructing particle tracks is explained. In the Analysis details section, numerical values for the selection criteria are provided along with an explanation of the signal extraction procedure and efficiency computation. The comparison of results from this analysis with published results is presented in the next section, while the last section is dedicated to the computation of systematic uncertainties.

## 4.1 Data selection

### 4.1.1 Data and MC samples

The analysis is done on two data sets, one with minimum-bias (MB) data<sup>1</sup> and the other with high-multiplicity (HM) data, with corresponding Monte-Carlo (MC) samples. The main results come from the HM dataset, and the MB is used for comparison with previous results as an assurance that the analysis is working properly. The data used for this analysis was collected by ALICE throughout the whole 2016-2018 period.

The LHC periods from 2016 that are used in the MB analysis are :

LHC16d\_pass2, LHC16e\_pass2, LHC16f\_pass2, LHC16g\_pass2, LHC16h\_pass2,  
LHC16i\_pass2, LHC16j\_pass2, LHC16k\_pass2, LHC16l\_pass3, LHC16o\_pass2,  
LHC16p\_pass2.

The periods used from 2017 are:

LHC17c\_pass2, LHC17e\_pass2, LHC17f\_pass2, LHC17g\_pass2, LHC17h\_pass2,  
LHC17i\_pass2, LHC17j\_pass2, LHC17k\_pass2, LHC17l\_pass2, LHC17m\_pass2,  
LHC17o\_pass2, LHC17r\_pass2.

The periods used from 2018 are:

LHC18b\_pass2, LHC18c\_pass2\_CENT, LHC18d\_pass2, LHC18e\_pass2, LHC18f\_pass2,  
LHC18g\_pass2, LHC18h\_pass2, LHC18i\_pass2, LHC18j\_pass2, LHC18k\_pass2,  
LHC18l\_pass2, LHC18m\_pass2, LHC18o\_pass2, LHC18p\_pass2, LHC18c\_pass2\_FAST.

All of the mentioned datasets are used in the MB analysis, while in the HM analysis, from 2016 only the LHC16o\_pass2 and LHC16p\_pass2 periods are used (data from 2017 and 2018 is the same). The other periods from 2016 didn't have flat multiplicity percentile distributions, meaning that the number of events was not constant with multiplicity. This would introduce a problem, as the multiplicity is split in classes that have some width. The mean of a certain multiplicity class should correspond to the mean value of multiplicity. If the multiplicity distribution is not constant, classes could be biased to show results for higher or lower multiplicity than their mean.

Monte-Carlo simulations were made for the same runs as in the data sample. For the HM, the LHC19h11a, b, c (+extra)\_tr were used. LHC19h11a, b, c are simulated for pp collisions at 13 TeV, reconstructed with Pythia8\_Monash2013\_HighMult\_001 and anchored to the High Multiplicity V0-triggered collisions on 2018., 2017. and 2016. data, respectively. LHC19h11\_extras include extra statistics.

<sup>1</sup>The minimum-bias data is raw data after the first trigger with no imposed cuts.

The MB LHC22e1\_tr was used with the MB dataset and is enriched in  $\Xi$  and  $\Omega$ . LHC22e1\_tr is for pp at 13 TeV, reconstructed with Pythia\_8\_Monash\_2013, injected strangeness (Geant4) and anchored to pass2 of Run2 data (2016-2018).

### 4.1.2 Event selection

Both for the data and MC, events were selected according to the following selection criteria implemented in the AliEventCuts class:

- Trigger selection: AliVEvent::kINT7 for the MB sample and AliVEvent::kHighMultV0 for the HM sample
- Rejection of “incomplete DAQ events” (only for data) using the AliESDevent::IsIncompleteDAQ() method.
- The primary vertex position along the beam axis must be within 10 cm of the nominal interaction point.
- Rejection of pile-up tagged events using the AliESDevent::IsPileupFromSPD() method.
- SPD and Track Vertex consistency: for events with both tracklets and track vertices reconstructed, it was verified that the separation along the z-coordinate is less than 5 mm.
- Rejection of background tagged events, based on the correlation between tracklets and clusters in the SPD, via the AliAnalysisUtils::IsSPDClusterVsTrackletBG() method.

After applying this selection, 860. mil. events were left in the HM sample and 1.9 bil in the MB sample.

### 4.1.3 Multiplicity selection

The events were divided into multiplicity classes. The selection applied is similar to that in previous analyses [1]. The multiplicity estimator is V0M centrality, which is based on the sum of the amplitudes from the V0-A and V0-C detectors. The multiplicity classes for MB are listed in table 4.1 and for HM in table 4.2.



Table 4.1: Multiplicity classes used for each particle in MB analysis.

Particle	V0M centrality intervals (%)
$\Xi^-, \bar{\Xi}^+$	0-1, 1-5, 5-10, 10-15, 15-20, 20-30, 30-40, 40-50, 50-70, 70-100
$\Omega^-, \bar{\Omega}^+$	0-5, 5-15, 15-30, 30-50, 50-100

Table 4.2: Multiplicity classes used for each particle in HM analysis.

Particle	V0M centrality intervals (%)
$\Xi^-, \bar{\Xi}^+, \Omega^-, \bar{\Omega}^+$	0-0.01, 0.01-0.05, 0.05-0.10

## 4.2 Cascade reconstruction

The  $\Xi$  and  $\Omega$  can't be detected directly as they have a short lifetime, so they must be observed through their decay products. Their decays consist of two steps before detection, known as cascade decay, so together they are called cascades. The topology of the cascade decay is shown in Figure 4.1. Reconstruction is based on the following decay channels

$$\begin{aligned}
\Xi^- [dss] &\rightarrow \Lambda [uds] + \pi^- [\bar{u}d] & \text{B.R. 99.9\%} & \quad c \cdot \tau = 4.91 \text{ cm} , \\
\bar{\Xi}^+ [\bar{d}\bar{s}\bar{s}] &\rightarrow \bar{\Lambda} [\bar{u}\bar{d}\bar{s}] + \pi^+ [u\bar{d}] & \text{B.R. 99.9\%} & \quad c \cdot \tau = 4.91 \text{ cm} , \\
\Omega^- [sss] &\rightarrow \Lambda [uds] + K^- [\bar{u}s] & \text{B.R. 67.8\%} & \quad c \cdot \tau = 2.461 \text{ cm} , \\
\bar{\Omega}^+ [\bar{s}\bar{s}\bar{s}] &\rightarrow \bar{\Lambda} [\bar{u}\bar{d}\bar{s}] + K^+ [u\bar{s}] & \text{B.R. 67.8\%} & \quad c \cdot \tau = 2.461 \text{ cm} .
\end{aligned}$$

In the following, I'll refer to both the particles and anti-particles  $\pi^- + \pi^+$ ,  $K^- + K^+$ ,  $\Lambda + \bar{\Lambda}$ ,  $\Xi^- + \bar{\Xi}^+$ ,  $\Omega^- + \bar{\Omega}^+$ , as pions, kaons, lambdas, xis, omegas or  $\pi$ ,  $K$ ,  $\Lambda$ ,  $\Xi$ ,  $\Omega$ .

Pions and kaons are charged and, therefore, can be traced and detected. They will be referred to as bachelor particles. The lambdas are electrically neutral and we need to detect their decay products. They will be referred to as baryon daughters or V0's and they decay into two charged particles, also called V0 daughters, in these decay channels

$$\begin{aligned}
\Lambda[uds] &\rightarrow p[uud] + \pi^-[\bar{u}d] & \text{B.R. } 64.1\% & \quad c \cdot \tau = 7.89 \text{ cm}, \\
\bar{\Lambda}[\bar{u}\bar{d}\bar{s}] &\rightarrow \bar{p}[\bar{u}\bar{u}\bar{d}] + \pi^+[u\bar{d}] & \text{B.R. } 64.1\% & \quad c \cdot \tau = 7.89 \text{ cm}.
\end{aligned}$$

Cascade reconstruction is done by associating three tracks, the bachelor track and the track pair from the V0 decay. These tracks must first pass a set of selections, explained in 4.2.1. After that, only the ones that match with topological selection 4.2.2 and with candidate selection 4.2.3, are considered. More detailed explanations from this chapter can be found in [49].

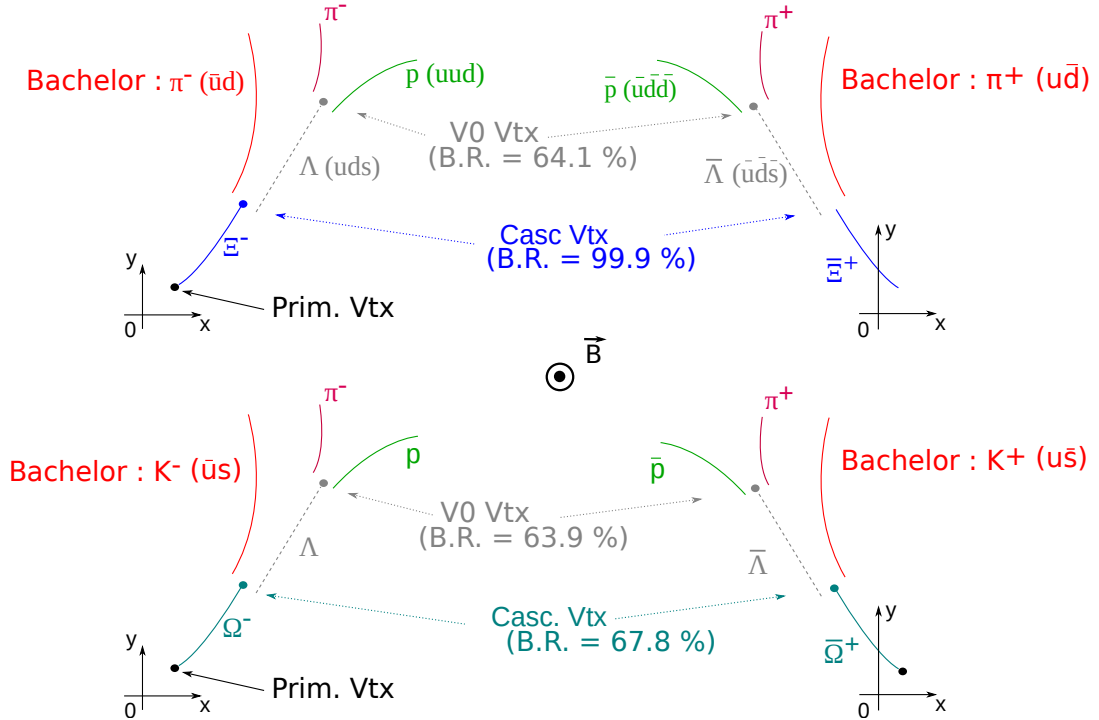


Figure 4.1: The topology of the cascade decay for cascades and their antiparticles along with successive decays. [50]

### 4.2.1 Track selections

The accurate identification of cascades relies heavily on the quality of reconstructing daughter tracks, specifically their momentum resolution and trajectory. The main tracking detectors of the ALICE are the ITS and the TPC, and reconstruction exclusively relies on their combined tracks, as they provide the best resolution. To guarantee the best momentum resolution and a precise estimation of particle trajectory, selection criteria are applied to daughter tracks.

The acceptance volume of all central detectors is in the pseudo-rapidity region  $|\eta| < 0.8$ , so only the tracks from this region are accepted. Any track that contains ITS and/or TPC shared clusters is rejected, as it could be wrongly assigned and could influence tracking quality.

All tracks need to pass the final refit in the TPC. The track parameters have been well estimated in the TPC when the track is re-propagated inward to reach its closest approach distance to the primary vertex. To ensure good momentum resolution and particle identification, the tracks are required to be associated in TPC with at least 70 readout pad rows of 159 in total.

For a track in the TPC, the parameter used for particle identification is the difference between the measured specific energy loss and the expected energy loss value determined by the Bethe-Bloch formula. When normalized to the resolution of the  $dE/dx$  measurement in the TPC, this difference can be expressed in terms of the number of standard deviations  $\sigma_{TPC}$

$$n_{\sigma} = \frac{(dE/dx)_{measured} - (dE/dx)_{Bethe-Bloch}}{\sigma_{TPC}}.$$

This provides the flexibility to choose the level of strictness in particle identification. For  $\Xi^-$  this would mean that the bachelor track must correspond to  $\pi^-$  and  $\Omega^-$  to  $K^-$ , while the positive V0 track must be compatible with a proton and negative with a pion.

Out-of-bunch pile-up events happen when two or more collisions happen within the readout time of the detectors, coming from different crossing bunches. To remove the contribution from those events, it is required that at least one of the daughters passes the ITS refit or TOF matching. The ITS refit is done by requiring that the track can be refitted in the ITS. TOF has highly precise information about the bunch crossing and it is required that one of the daughter particles matches a specific event. [1]

### 4.2.2 Topological selections

Topological reconstruction is done by applying geometric and kinematic criteria to the daughter tracks. All the applied cuts are shown in Figure 4.2. The goal is to find our cascades, which are primary particles, and to do that first we need to track the secondary particles.

To find V0's, each secondary track is combined with all other secondary tracks that have an opposite charge. Two cuts are applied to the minimum value of the distance to the primary vertex. To make sure they are secondary particles this has to be larger than a given value. These cuts are seen in Fig. 4.2 under 1.a). The minimal distance of closest approach (DCA) is set for the V0 daughters. In the case of  $\Xi^-$ , same is done for  $\pi^-$  and p (and similar for  $\Omega^-$  and  $\bar{\Omega}^+$ ). For a pair of tracks, their minimal respective distance (DCA between V0 daughters, shown under 1.b) ) must be less than a given value. After finding the V0 vertex, a check is done to see

if the momentum vector of the V0 points back to the cascade vertex. This is done by applying the cut to the cosine of the angle between the V0 momentum vector and a vector connecting the cascade vertex to V0, as shown in 1.b). In the end, the DCA between the V0 track and the primary vertex (PV) is set to be larger than a selected value, so that V0's that are primaries can be excluded.

The invariant mass of V0 is then calculated and compared to the real mass of the  $\Lambda$ . The particle is rejected if the calculated mass is greater than the resolution of the detector. The detector has limited accuracy, so the value of the measured mass will follow some distribution, as shown in Figure 4.2 panel 1.d).

The cascades are identified in a similar way. The V0's found within the  $\Lambda$  mass window are combined with all possible secondary tracks. These are then bachelor candidates. Two selection criteria are put on the bachelor track. The DCA to PV for the bachelor must be larger than a given value, the one for V0 is already done in the V0 finding, and the DCA between the bachelor and V0 must be under some value. These are shown in Figure 4.2 in panels 2.a) and 2.b).

Next, check that the cosine of the PA of the cascade candidate is larger than set values, as this angle must be relatively small since the cascades have a short lifetime. This is shown in 2.c). The final selection makes sure that the cascade vertex position is larger than some minimal distance from PV. It is also demanded that the V0 vertex is outside of the selected maximal distance to ensure causality. In the example in panel 2.d) this leads to the rejection of the V0 vertex.

These are all standard cuts that were applied in the previous analyses [51, 52]. There is one additional cut in this analysis, that is now applied in all new analyses that contain  $\Omega$  and  $\Xi$ . This cut is related to the angle between V0 and the momentum vector of the sum of bachelor and baryon and is set to be larger than a set small value to make sure they are not coming from the same point. It is shown in Figure 4.3 how  $\Lambda$  decay can be wrongly identified as  $\Xi$ .

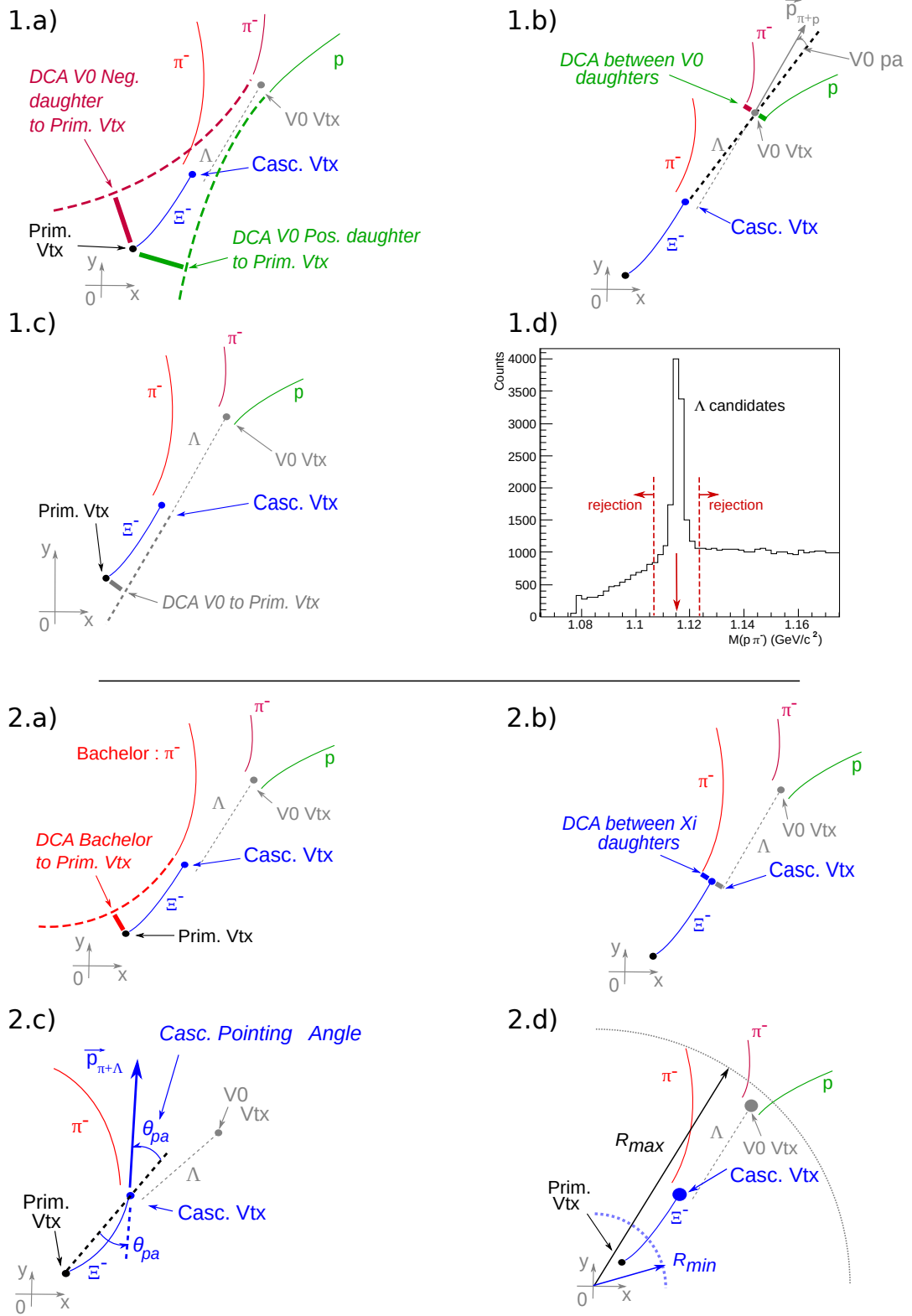


Figure 4.2: Illustrations of topological selections used to reconstruct  $\Xi^-$ . V0 daughters selection is shown in 1.a)-d), while the selections relevant to cascade are shown in 2.a)-d). [53]

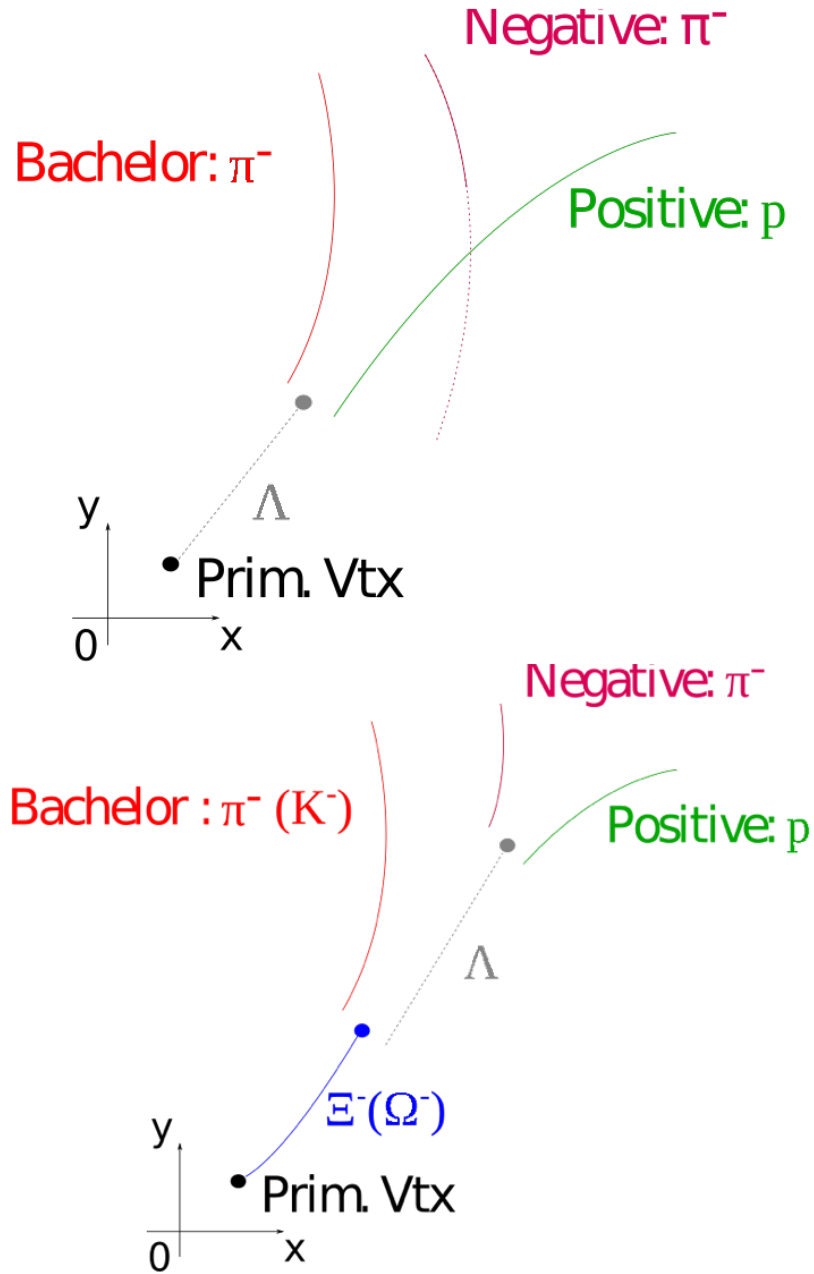


Figure 4.3: Illustration of a  $\Lambda$  decay with a pion passing close to a proton, which could result in misidentifying it as  $\Xi$ . [49]

### 4.2.3 Candidate selections

The hyperons at ALICE are studied in the mid-rapidity<sup>2</sup> window  $|y| < 0.5$ . As  $\Omega$  and  $\Xi$  share the same V0 decay daughters, the selection of competing cascade rejection is applied for  $\Omega$ . This means that candidates, in  $\Omega$  analysis, that are within some range of the  $\Xi$  mass are rejected. The width of the rejecting region was determined according to the invariant mass resolution of the corresponding competing signal, which is for  $\Xi$  equal to  $8 \text{ MeV}/c^2$ .

The candidates that have proper lifetimes larger than expected are also rejected to avoid background from interactions with the detector material. The proper lifetime is calculated using mass and measured variables, momentum and length, and is required to be less than three times the expected value.

For Monte Carlo, it is additionally checked that the reconstructed cascade candidate corresponds to the „true” primary particle.

---

<sup>2</sup>Rapidity is used to express angles with respect to the axis of the colliding beams. It is defined as  $y = \frac{1}{2} \ln \frac{E+p_z}{E-p_z}$ , where  $E$  is the energy of the particle and  $p_z$  is the momentum along the beam axis.

## 4.3 Analysis details

The analysis was performed on two datasets, HM and MB. The MB was used to compare the results with a previous analysis [52], by repeating the same analysis procedure, to make sure the new analysis produces the same results. After confirming that the analysis was producing the expected results, it was then applied on HM data with minor changes, such as setting differences in multiplicity classes and binning of transverse momentum spectra.

### 4.3.1 Analysis cuts

The selection criteria explained in section 4.2 are called cuts. The numerical values of cuts are determined from various previous analyses and through studies on how specific cuts influence results. For a cut to be good, it is important that it doesn't reduce too much of the real signal, i.e. true cascade candidates, but to reduce as much background as possible. For these studies, MC is most suitable, as we know what are real candidates and what is just background.

The values used in this analysis are taken from [1] and are listed in table 4.3. For the HM sample, the cut on the bachelor-baryon cosine pointing angle is added, and the cut on the cosine of the cascade pointing angle is tighter. The bachelor-baryon cosine pointing angle is explained in the previous section and graphically shown in Figure 4.3. Tightening of the cascade pointing angle removes a lot of background in both  $\Xi$  and  $\Omega$ . The same cuts are applied to the data and the MC with one difference: in the MC analysis the cascade candidate is further checked to match a „true” primary particle of the same species.

### 4.3.2 Signal extraction

The candidates that are left after passing all the selection criteria are composed of true cascades and background candidates. There is no way to know which is which, so to separate the real signal from the background, statistical analysis is employed based on the analysis of the invariant mass spectrum.

To determine the invariant mass of the cascade, the invariant mass of the two daughter tracks must be measured first. This is done using the following relation

$$M_{measured}^2(\Lambda) = \left( \sqrt{m_{\pi^-}^2 + \vec{p}_{neg}^2} + \sqrt{m_p^2 + \vec{p}_{pos}^2} \right)^2 - (\vec{p}_{neg} + \vec{p}_{pos})^2,$$

where  $m_{\pi^-}$  and  $m_p$  are PDG values for masses of pion and proton, while  $\vec{p}_{neg}$  and  $\vec{p}_{pos}$  are their respective momenta measured by the detector. To get the mass of a cascade the procedure is



Table 4.3: Track, topological and candidate selection criteria applied to charged  $\Xi$  and  $\Omega$  candidates.

Track selection	$\Xi$ ( $\Omega$ ) cut value
Daughter track pseudorapidity	$ \eta  < 0.8$
Daughter track $N_{TPCclusters}$	$\geq 70$
TPC dE/dx selection	$< 5\sigma$
out-of-bunch pile-up rejection	ITSorTOFrefit for at least one daughter
Topological selection	$\Xi$ ( $\Omega$ ) cut value
Cascade transverse decay radius $R_{min}$	$> 0.6(0.5) \text{ cm}$
V0 transverse decay radius $R_{max}$	$> 1.2(1.1) \text{ cm}$
DCA bachelor to PV	$> 0.04 \text{ cm}$
DCA V0 to PV	$> 0.06 \text{ cm}$
DCA meson V0 to PV	$> 0.04 \text{ cm}$
DCA baryon V0 to PV	$> 0.03 \text{ cm}$
DCA between V0's	$< 1.5\sigma$
DCA bachelor to V0	$< 1.3 \text{ cm}$
Cascade cos(PA)	for MB $> 0.97$ and for HM $> 0.998$
V0 cos(PA)	$> 0.97$
V0 mass window	$\pm 8 \text{ MeV}/c^2$
Bachelor to baryon cos(PA) (HM only)	pT-dependent - min. value $< 0.9992$
Candidate selection	$\Xi$ ( $\Omega$ ) cut value
Rapidity interval	$ y  < 0.5$
Proper lifetime	$< 3 \times c\tau$
Competing cascade rejection (only for $\Omega$ )	$ M(\Xi) - 1.321  > 8 \text{ MeV}/c^2$
MC association (MC only)	identity assumption for cascades

repeated once more, but now for a bachelor and a V0

$$M_{measured}^2(\Xi^-) = \left( \sqrt{m_{\Lambda}^2 + \vec{p}_{V0}^2} + \sqrt{m_{\pi^-}^2 + \vec{p}_{bach}^2} \right)^2 - (\vec{p}_{V0} + \vec{p}_{bach})^2,$$

$$M_{measured}^2(\Omega^-) = \left( \sqrt{m_{\Lambda}^2 + \vec{p}_{V0}^2} + \sqrt{m_{K^-}^2 + \vec{p}_{bach}^2} \right)^2 - (\vec{p}_{V0} + \vec{p}_{bach})^2,$$

where  $\vec{p}_{V0} = \vec{p}_{neg} + \vec{p}_{pos}$ , and  $\vec{p}_{bach}$  is the measured momentum of the bachelor candidate. In a similar way, the mass of anti-particles is computed.

The measurement accuracy is not perfect, so the reconstructed invariant masses will be distributed in a peak structure with a width is determined by detector resolution. The invariant

mass of the true cascade candidates should be close to the PDG mass and should form a peak, while the background comes from a random association of three tracks and should have a flat or decreasing distribution.

The invariant mass plots are divided into transverse momentum ( $p_T$ ) bins. For the MB sample, the bin selection is made to be the same as in [52], so an exact comparison can be done with final spectra (shown in Table 4.4). For the HM sample, the number of bins for  $\Omega$  is made to match the bins for  $\Xi$ , as there are enough statistics for  $\Omega$  and it is better for spectra to have a larger number of bins (shown in Table 4.5). Only the first  $p_T$  bin (0.6-1.0) is not included, as there were not enough statistics in the data and Monte-Carlo, so the uncertainties were too large.

Table 4.4:  $p_T$  bins used for each particle in MB analysis.

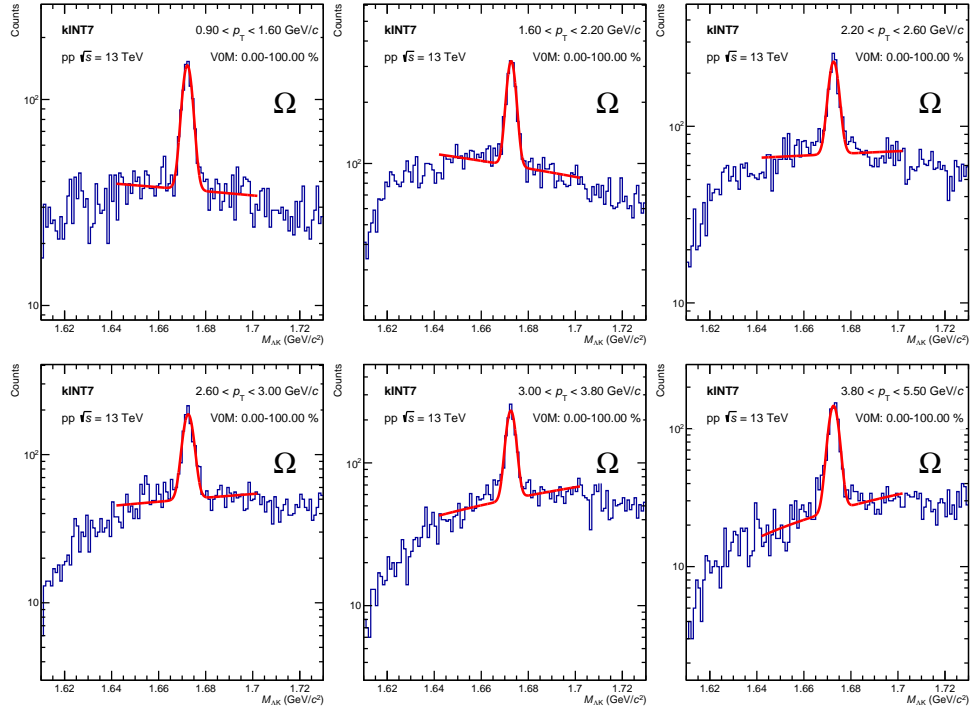
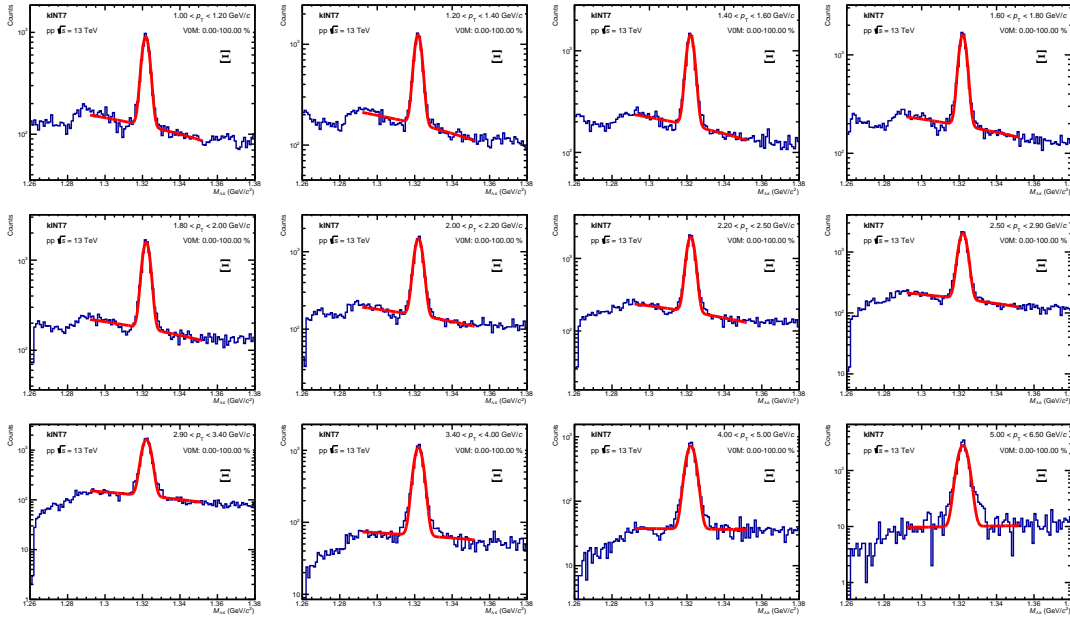
Particle	Minimum-Bias $p_T$ interval limits (GeV/c)
$\Xi$	1.0, 1.2, 1.4, 1.6, 1.8, 2.0, 2.2, 2.5, 2.9, 3.4, 4.0, 5.0, 6.5
$\Omega$	0.90, 1.60, 2.20, 2.60, 3.00, 3.80, 5.50

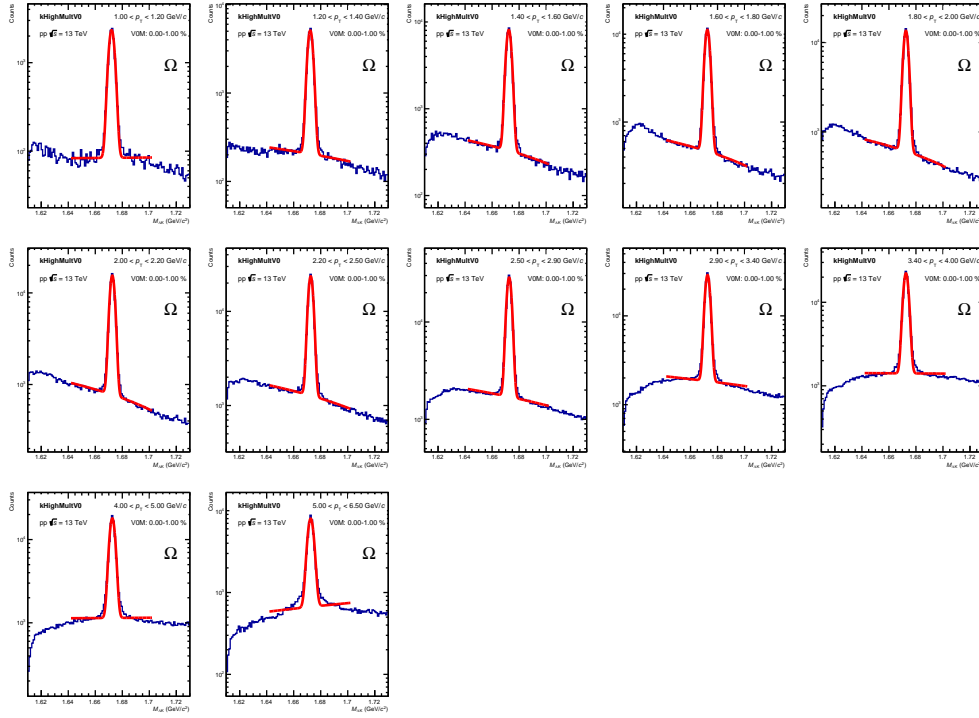
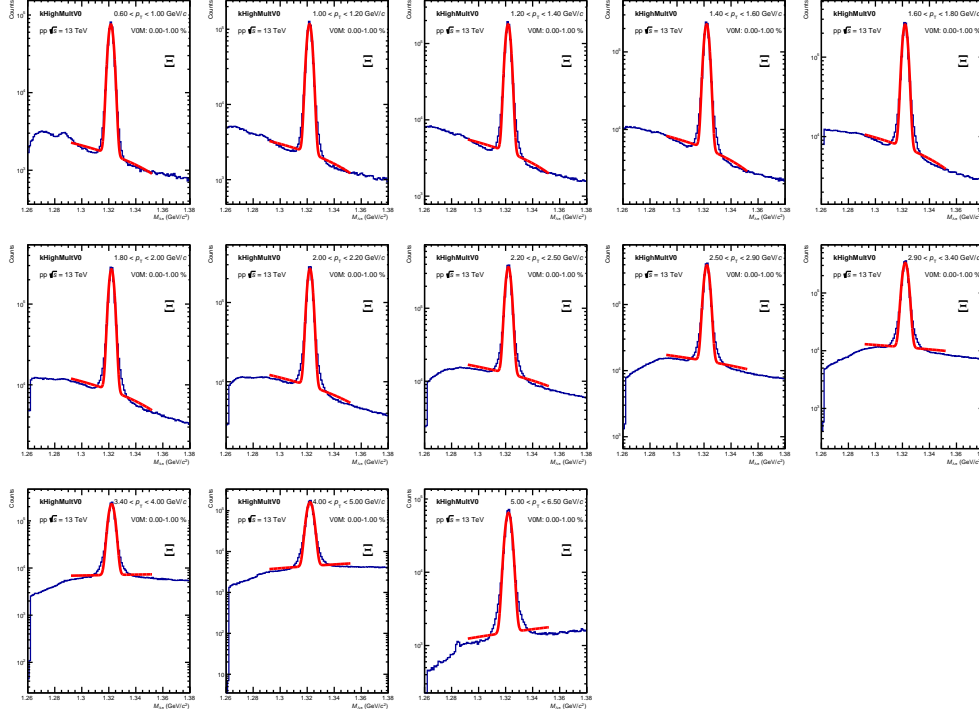
Table 4.5:  $p_T$  bins used for each particle in HM analysis.

Particle	High-Multiplicity $p_T$ interval limits (GeV/c <sup>2</sup> )
$\Xi$	0.6, 1.0, 1.2, 1.4, 1.6, 1.8, 2.0, 2.2, 2.5, 2.9, 3.4, 4.0, 5.0, 6.5
$\Omega$	1.0, 1.2, 1.4, 1.6, 1.8, 2.0, 2.2, 2.5, 2.9, 3.4, 4.0, 5.0, 6.5

The invariant mass distributions are then fitted with a Gaussian for the signal and a linear function for the background, in order to determine the mean ( $\mu$ ) and the width ( $\sigma_G$ ) of the signal peak. The same procedure is applied for MC. The signal is then extracted by using the bin counting procedure. The integral of the peak region, defined as  $([\mu - 4\sigma_G, \mu + 4\sigma_G])$ , is subtracted by the integral of a background region  $([\mu - 8\sigma_G, \mu - 4\sigma_G] \cup [\mu + 4\sigma_G, \mu + 8\sigma_G])$  to get the raw signal.

For the MB data, the fitted invariant mass distributions are shown in Figures 4.4, 4.5, and for HM in Figures 4.6, 4.7. Notice that the y-axis is in logarithmic scale, so although the background looks large, it is an order of magnitude lower than the signal peak.

Figure 4.4:  $\Omega$  invariant mass plots for MB data fitted with a Gaussian plus linear function.Figure 4.5:  $\Xi$  invariant mass plots for MB data fitted with a Gaussian plus linear function.

Figure 4.6:  $\Omega$  invariant mass plots for HM data fitted with a Gaussian plus linear function.Figure 4.7:  $\Xi$  invariant mass plots for HM data fitted with a Gaussian plus linear function.

### 4.3.3 Acceptance x efficiency

The obtained raw signal is not the real number of produced particles. It is what the detector managed to detect and what is left after all the selections and cuts were applied. The acceptance is a „detector volume” in which you expect to see the particles, and efficiency is the probability of reconstructing a particle in the detector. To correct the raw signal, Monte-Carlo is used. In MC, the real number of generated particles is well known. After passing it through a simulation of the detector (Geant) and repeating the same analysis procedure, the raw MC signal is left. The ratio of MC signal  $N_{MCraw}$  and the number of generated particles  $N_{generated}$  is done for all  $p_T$  bins to get the acceptance-efficiency

$$\epsilon(p_T) = \frac{N_{MCraw}(p_T)}{N_{generated}(p_T)}.$$

The efficiencies are computed for different multiplicity bins in the MB sample. It can be seen in Figure 4.8 that there is no multiplicity dependence in efficiencies, as most of them are under one  $\sigma$  of each other. Therefore, it was decided to use integrated efficiency in the analysis, i.e., the same efficiency for the whole multiplicity range. This same procedure was already done in [52]. Since the uncertainties on the efficiencies computed as a function of multiplicity are large in some cases, a systematic uncertainty of 2 % is assigned for all  $p_T$  bins.

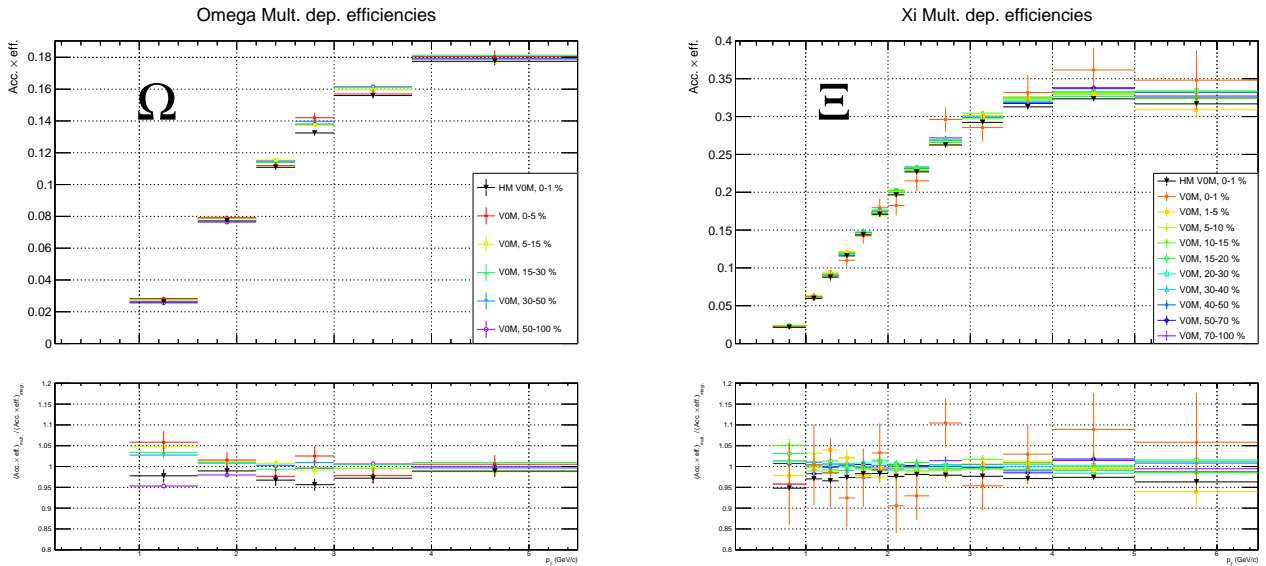


Figure 4.8: Acceptance times efficiency corrections as a function of multiplicity for  $\Omega$  (left) and  $\Xi$  (right) for the MB sample (rainbow) and the HM int. multiplicity sample (black). The ratio on the bottom panels is done wrt. integrated MB efficiency.

In the HM sample, the multiplicity dependent efficiencies couldn't be computed as the size of the multiplicity bins was smaller than the resolution of histograms that contained information about the number of generated particles in MC. The resolution was 1 % and the highest multiplicity bin goes from 0 to 0.01 %. As the efficiency has the same values and shape for MB and HM MC samples, it was decided to use integrated efficiency and to assign the same systematic uncertainty of 2 %. Efficiencies obtained from HM MC are shown in Figure 4.8 with black lines.

## 4.4 Comparison to the published results

To make sure that the analysis procedure works as expected, meaning that all analysis steps are correctly applied, a ratio is done between MB data from 2016-2018 and MB data from 2015. The 2015 data was used in a previous analysis [1], and as the cut values and analysis procedure are the same, the results should also be the same. The comparison is done at the level of the corrected  $p_T$  spectra. The explanation of the importance and the properties of  $p_T$  spectra will be given in the next chapter.

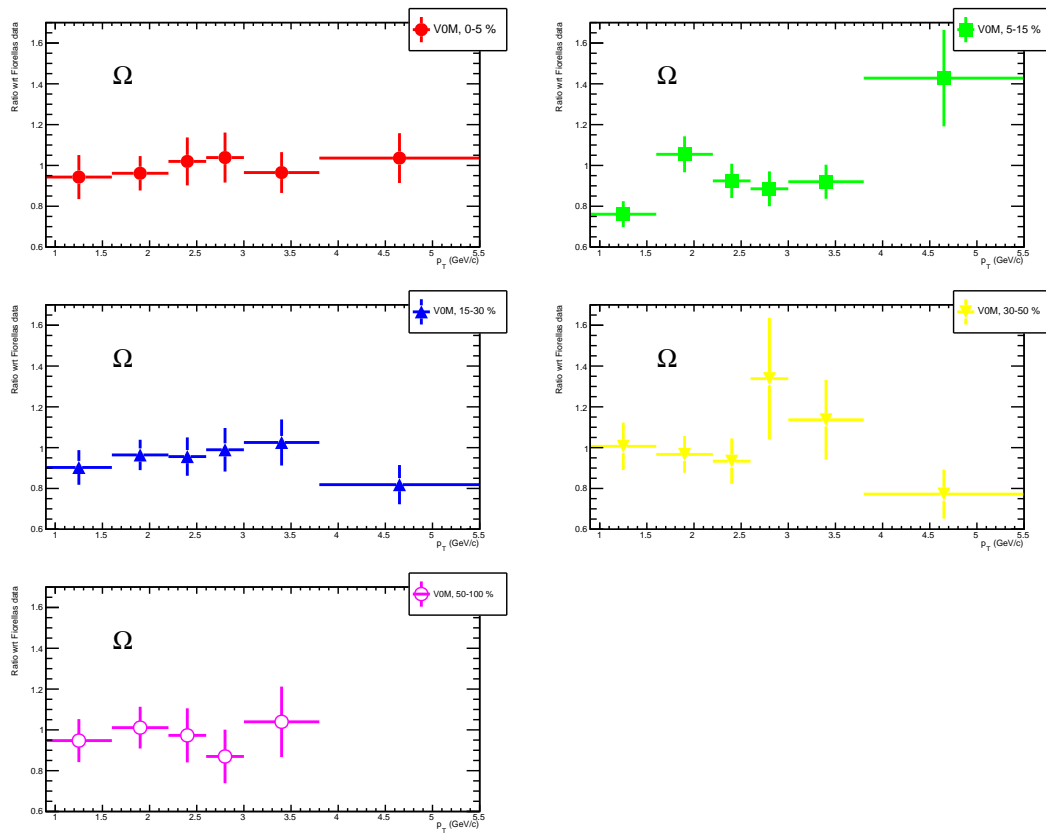
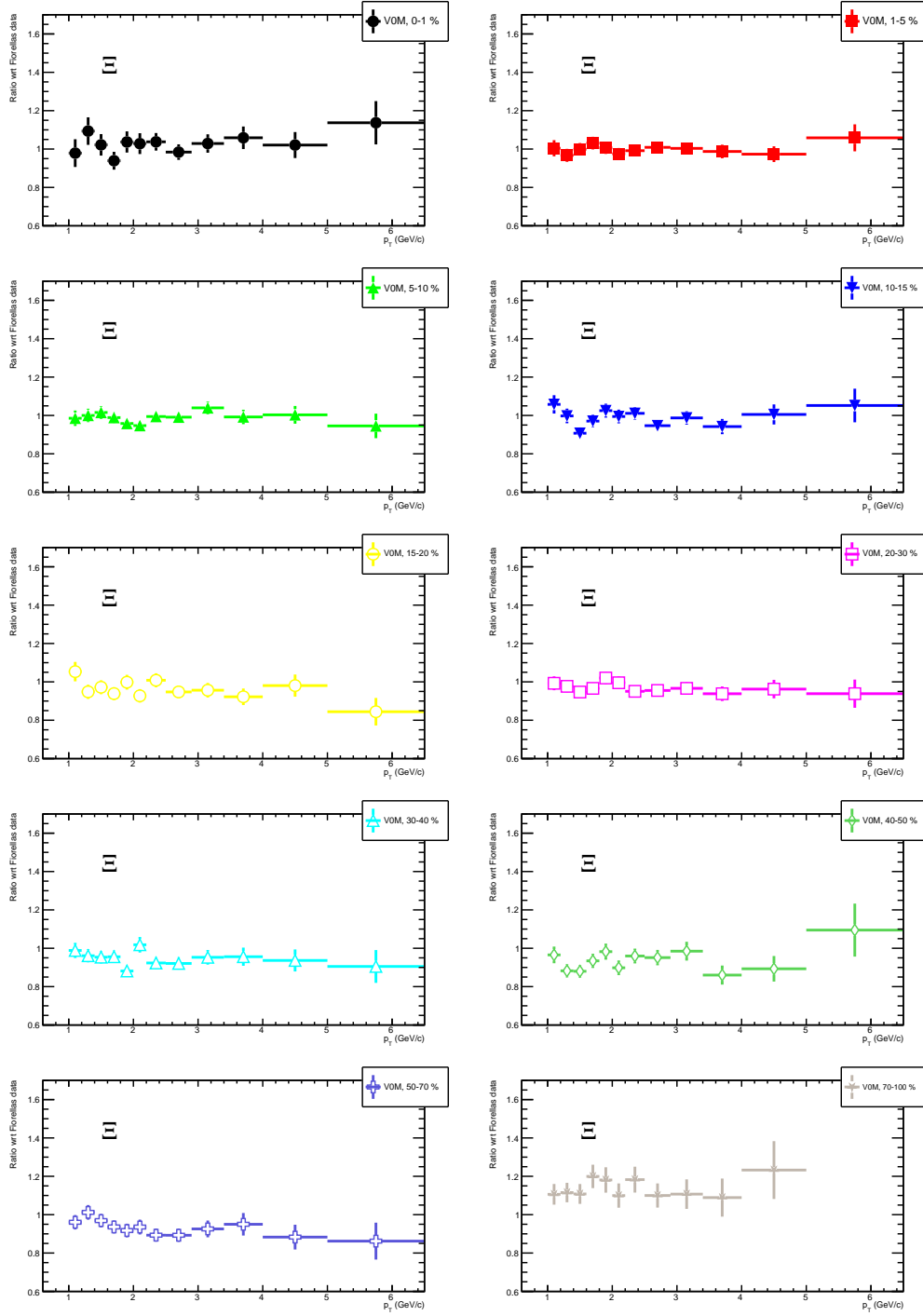


Figure 4.9: Ratio of  $\Omega$  MB corrected  $p_T$  spectra to the published results.

In Figures 4.9 and 4.10, it can be seen that for most  $p_T$  bins, the ratio is equal to one, within one sigma. Also to be noted, the errors are statistical, meaning that the real error, the one with systematical uncertainties, would be larger than the ones shown in the plots. The errors are larger for  $\Omega$  because there were not a lot of statistics for  $\Omega$  in 2015.

It was therefore concluded that the results are compatible with each other, meaning that the analysis is done correctly. The systematics were only done for the HM sample, as the results from MB have already been published and there is no need to recompute them.

Figure 4.10: Ratio of  $\Xi$  MB corrected  $p_T$  spectra to the published results.



## 4.5 Systematic uncertainties

Systematic uncertainties are uncertainties in measurements that arise from imperfections or limitations in the experimental setup, calibration procedures, modeling assumptions, or analysis techniques. Unlike statistical uncertainties, which arise from the inherent variability in data, systematic uncertainties are associated with known or unknown biases and errors in the experimental or theoretical procedures. These uncertainties can impact the accuracy and the precision of results and should always be carefully considered.

The computation of systematic uncertainties consists of a set of variations around the applied selection criteria, as done in previous analyses [52, 51]. This is done by repeating the analysis with some different cut values and reassessing the results. If the results don't change with some variation of the cut, it can be concluded that there is no systematic error in that cut. On the other hand, if the results change, that is an indication of a systematic effect that needs to be included in the final results error.

To decide if the systematic uncertainty is significant or not, the Roger Barlow approach is used [54]. When the analysis is performed for two different cut values, the first value will give the result  $r_1$  with uncertainty  $\sigma_1$ , and the other value  $r_2$  and  $\sigma_2$ . As the analysis procedure and the used data are the same, these two results are fully correlated. To compare these results, the ratio  $r_1/r_2$  is computed. If there is no systematic error, the ratio will equal one. In the real world, there will be some deviation from unity, and to decide if the difference is significant, Barlow criteria are employed. If the deviation from unity is under one Barlow sigma  $\sigma_{Barlow} = \sqrt{\sigma_1^2 - \sigma_2^2}$ , the systematic uncertainty is considered insignificant.

All the systematics are computed separately for the three different multiplicity classes. The plots shown in this chapter are only for the highest multiplicity bin (0.00-0.01 %) as the uncertainties for the other classes show the same behavior and have similar values.

### 4.5.1 Cut variations

The variations of the cuts are the same as used in previous analyses [51, 52]. The values of the cut variations around default cuts (table 4.3), are shown in table 4.6 for  $\Omega$  and in table 4.7 for  $\Xi$ .

It was also checked that with these cut variations, not more than 10 % of the total raw signal is lost with respect to the loosest cut. These are shown in Figures 4.11 and 4.12. In some  $p_T$  bins, the signal loss is greater than 10 % for the tightest cut, but if the MC has the same behavior the final results don't change. This is checked by doing a ratio of corrected  $p_T$  spectra.

To get the values of the systematic errors on  $p_T$  spectra, the ratio of the varied corrected  $p_T$  spectra to the one with default cuts is done, with the errors computed with the Barlow procedure.

The ratios are shown in Figures 4.13 and 4.14. For each cut, only the maximum deviations are considered for the final systematics. Maximum deviations are shown in Figures 4.15 and 4.16. If errors are significant, based on Barlow criteria, they are added in quadrature to form the total systematic uncertainty for each  $p_T$  bin, shown in red in Figures 4.17 and 4.18.

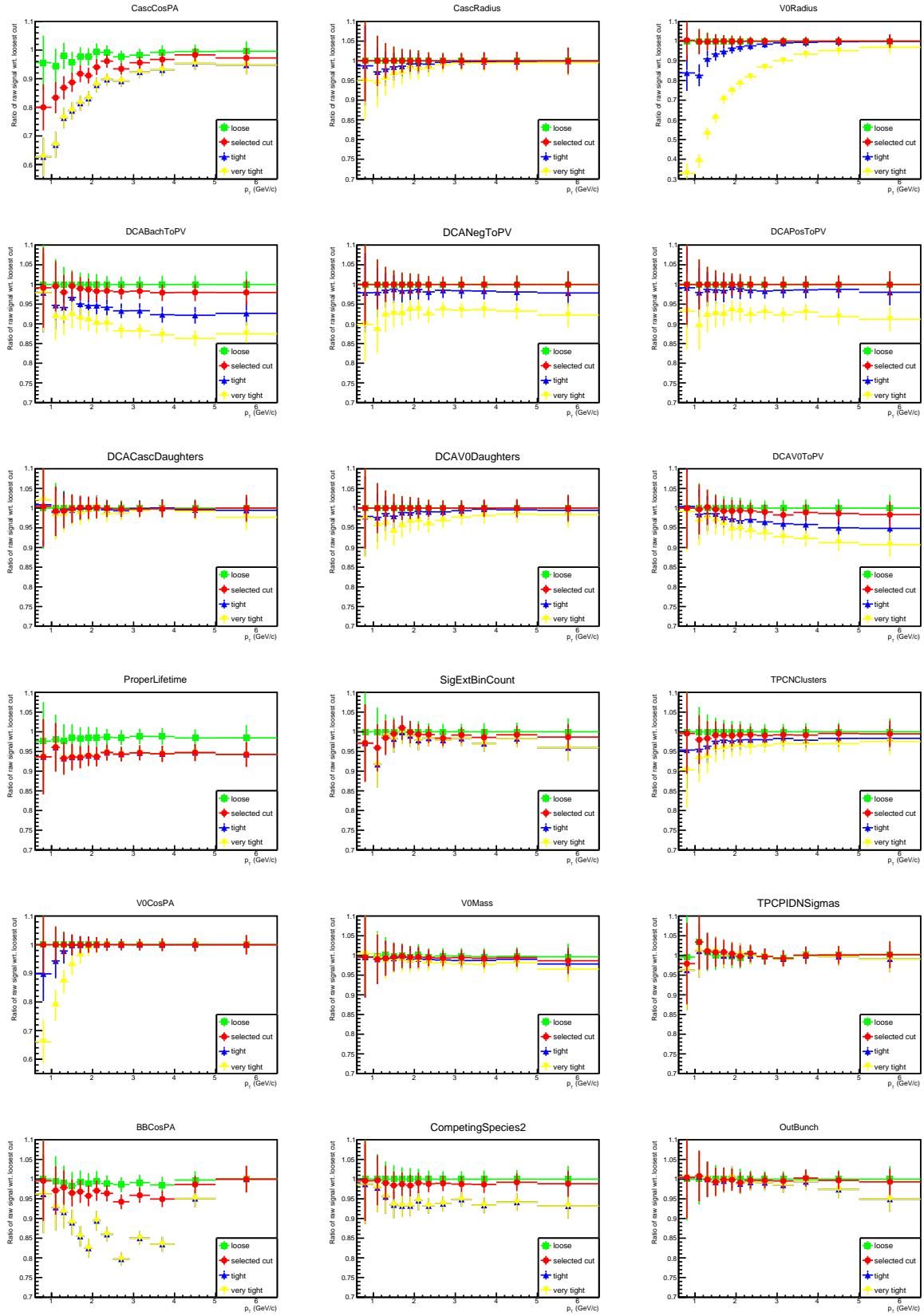
The total systematic uncertainty is the sum in quadrature of the systematic uncertainty coming from cut variation, signal extraction detector material budget, uncertainty from using integrated multiplicity, and from in-bunch pile-up. In Figures 4.17 and 4.18, the cut variation contribution is shown in red, and the material budget contribution is shown in green. The pile-up contribution is not shown as it is taken to be 2 % for all  $p_T$  bins. The in-bunch pile-up is taken from [52]. The multiplicity uncertainty of 2 % is not added to the plots but is added to the final spectra used in computing integrated yields.

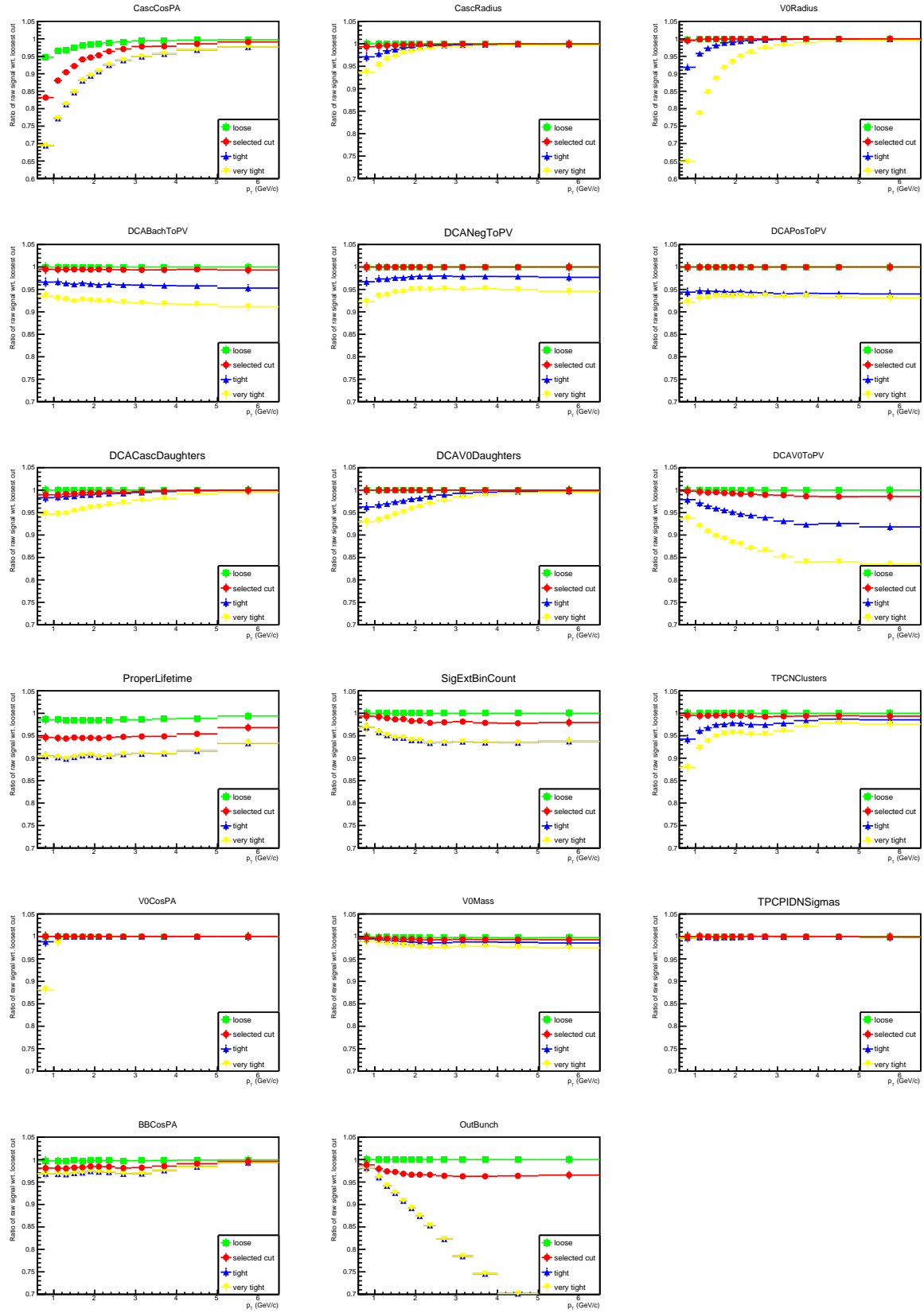
Table 4.6: Values of the selection cuts chosen for systematics estimation in the HM  $\Omega$  analysis.

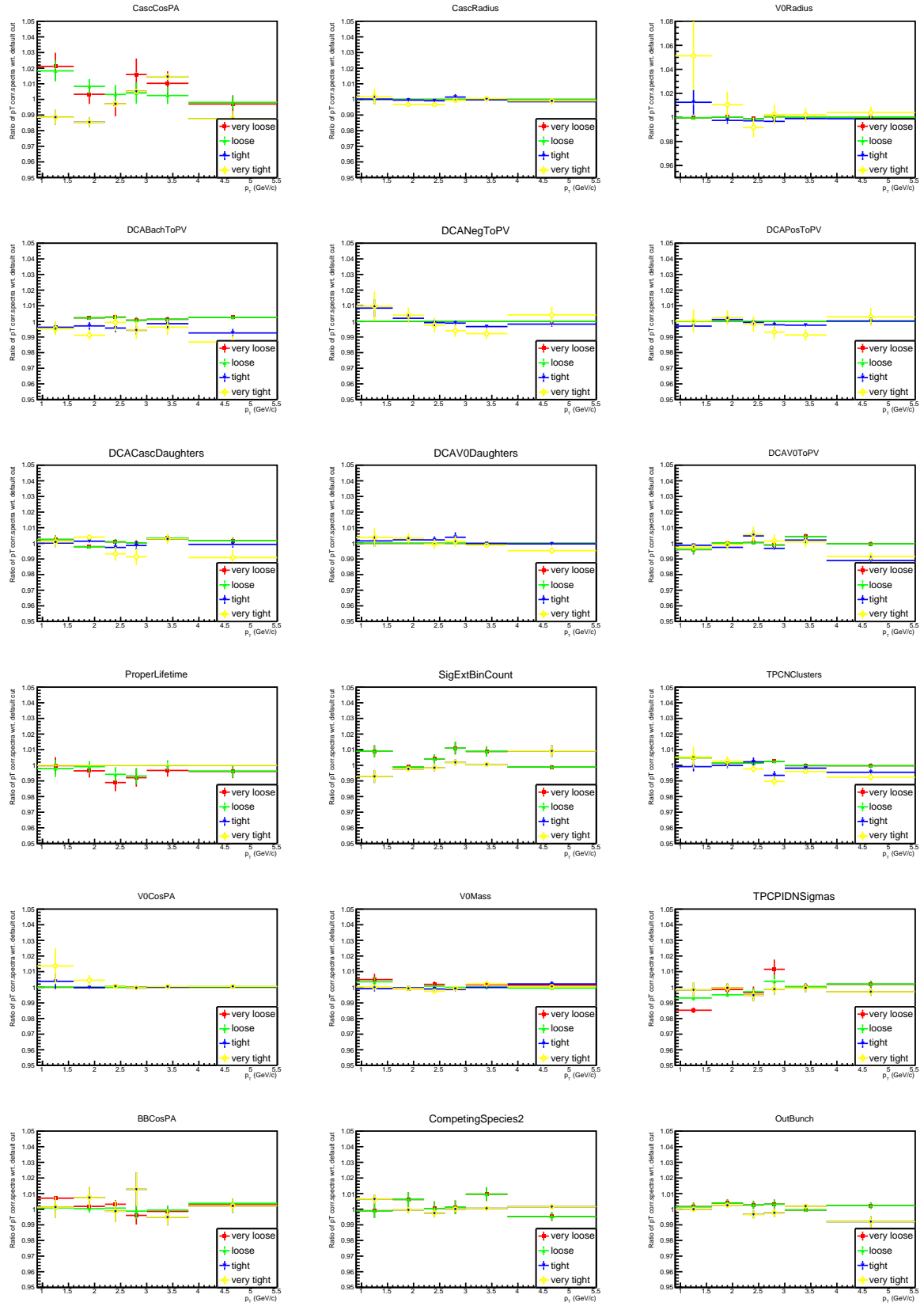
Track selection	$\Omega$ Cut value			
	very loose	loose	tight	very tight
Daughter track $N_{TPCclusters}$		$\geq 67$	$\geq 73$	$\geq 76$
TPC dE/dx selection	$< 7\sigma$	$< 6\sigma$	$< 4\sigma$	
out-of-bunch pile-up rejection	none			ITSrefit
Topological selection	$\Omega$ Cut value			
Cascade transverse decay radius $R_{min}$	$> 0.3$	$> 0.4$	$> 0.6$	$> 0.7$
V0 transverse decay radius $R_{max}$		$> 1.0$	$> 2.5$	$> 6.0$
DCA bachelor to PV		$> 0.03$	$> 0.07$	$> 0.10$
DCA V0 to PV		$> 0.05$	$> 0.08$	$> 0.10$
DCA meson V0 to PV	$> 0.02$	$> 0.03$	$> 0.10$	$> 0.30$
DCA baryon V0 to PV		$> 0.02$	$> 0.05$	$> 0.10$
DCA between V0's	$> 2.0$	$> 1.8$	$> 1.3$	$> 1.0$
DCA bachelor to V0	$> 2.0$	$> 1.8$	$> 1.0$	$> 0.6$
Cascade cos(PA)	$> 0.994$	$> 0.996$	$> 0.999$	
V0 cos(PA)	$> 0.95$	$> 0.96$	$> 0.98$	$> 0.985$
V0 mass window	$\pm 10$	$\pm 9$	$\pm 7$	$\pm 6$
Bachelor to baryon cos(PA)	$< 0.9998$	$< 0.9995$	$< 0.998$	
Candidate selection	$\Omega$ Cut value			
Proper lifetime	$< 5$	$< 4$	$< 3$	
Competing cascade rejection	$\pm 2$	$\pm 5$	$\pm 14$	$\pm 20$
Signal extraction window		$\pm 4.5$	$\pm 3.5$	

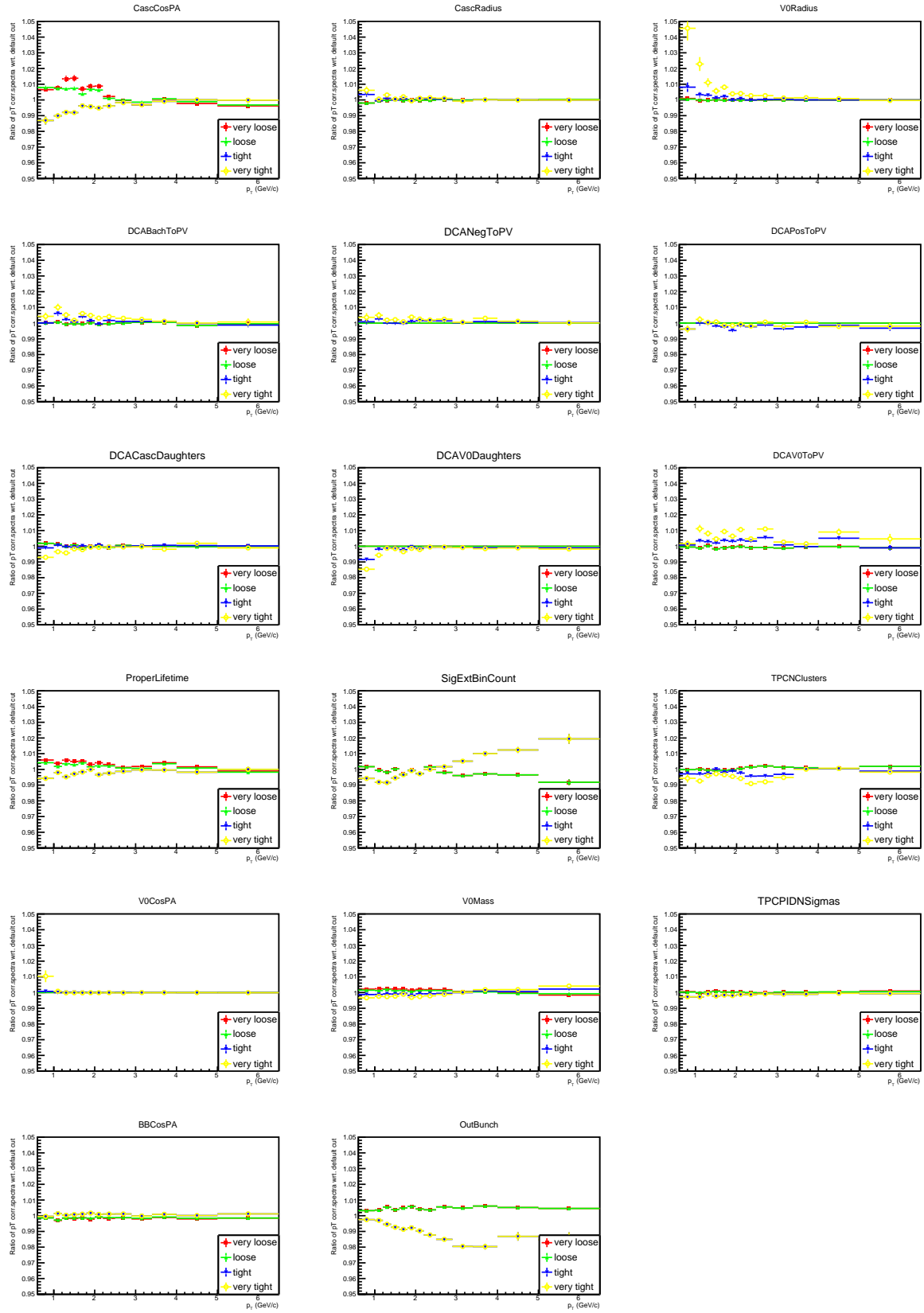
Table 4.7: Values of the selection cuts chosen for systematics estimation in the HM  $\Xi$  analysis.

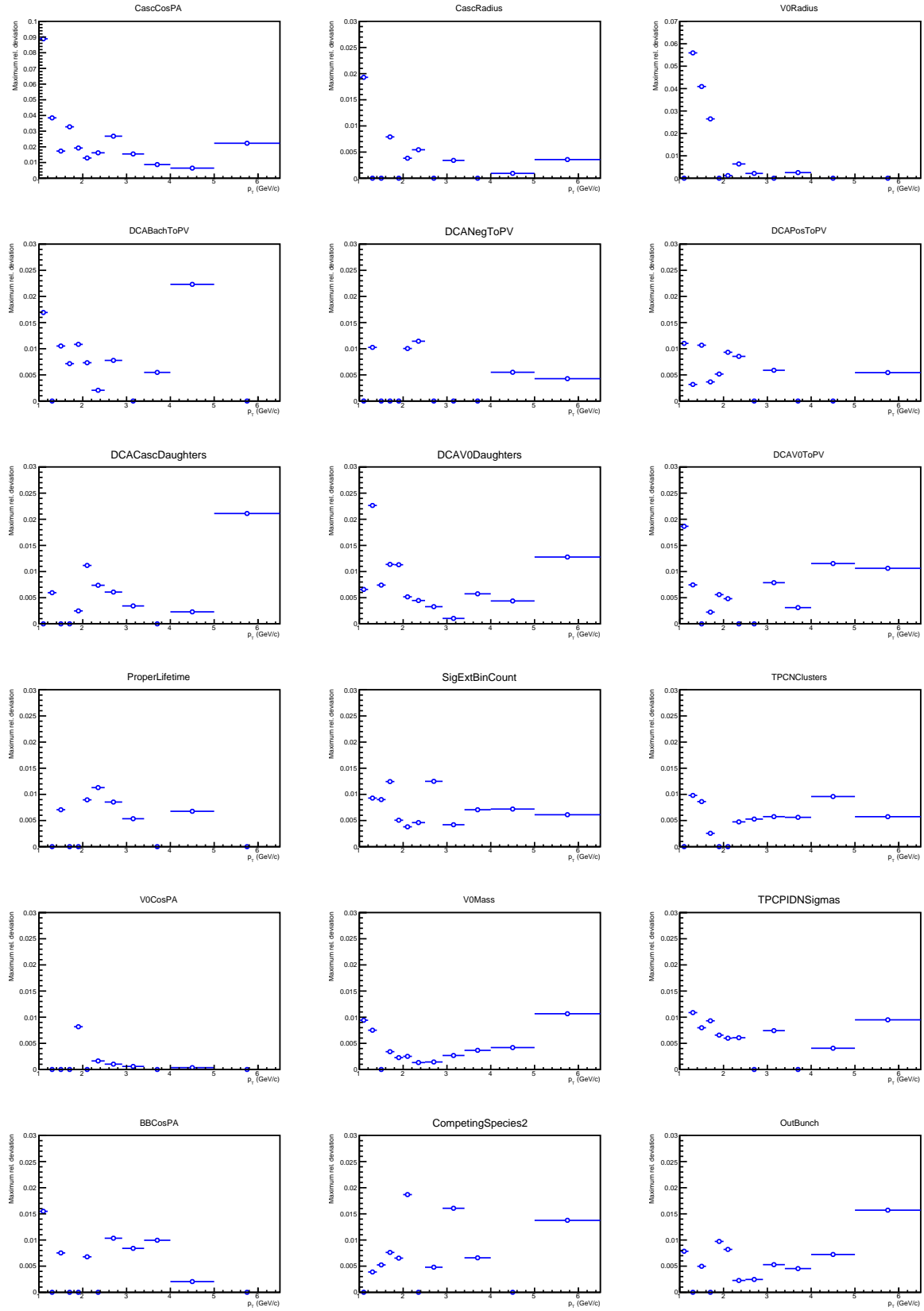
Track selection	$\Xi$ Cut value			
	very loose	loose	tight	very tight
Daughter track $N_{TPCclusters}$		$\geq 65$	$\geq 75$	$\geq 80$
TPC dE/dx selection	$< 7\sigma$	$< 6\sigma$	$< 4\sigma$	
out-of-bunch pile-up rejection	none			ITSrefit
Topological selection	$\Xi$ Cut value			
	very loose	loose	tight	very tight
Cascade transverse decay radius $R_{min}$	$> 0.4$	$> 0.5$	$> 0.8$	$> 1.0$
V0 transverse decay radius $R_{max}$	$> 1.0$	$> 1.1$	$> 2.5$	$> 5.0$
DCA bachelor to PV		$> 0.03$	$> 0.1$	$> 0.17$
DCA V0 to PV		$> 0.05$	$> 0.1$	$> 0.15$
DCA meson V0 to PV	$> 0.02$	$> 0.03$	$> 0.15$	$> 0.30$
DCA baryon V0 to PV		$> 0.02$	$> 0.09$	$> 0.11$
DCA between V0's	$> 2.0$	$> 1.8$	$> 1.1$	$> 0.8$
DCA bachelor to V0	$> 2.0$	$> 1.8$	$> 1.2$	$> 1.0$
Cascade cos(PA)	$> 0.994$	$> 0.996$	$> 0.999$	
V0 cos(PA)	$> 0.95$	$> 0.96$	$> 0.98$	$> 0.99$
V0 mass window	$\pm 10$	$\pm 9$	$\pm 7$	$\pm 6$
Bachelor to baryon cos(PA)	$< 0.9998$	$< 0.9995$	$< 0.998$	
Candidate selection	$\Xi$ Cut value			
	very loose	loose	tight	very tight
Proper lifetime	$< 5$	$< 4$	$< 2.5$	
Signal extraction window		$\pm 5$	$\pm 3$	

Figure 4.11: Signal loss with cut variation for  $\Omega$ .

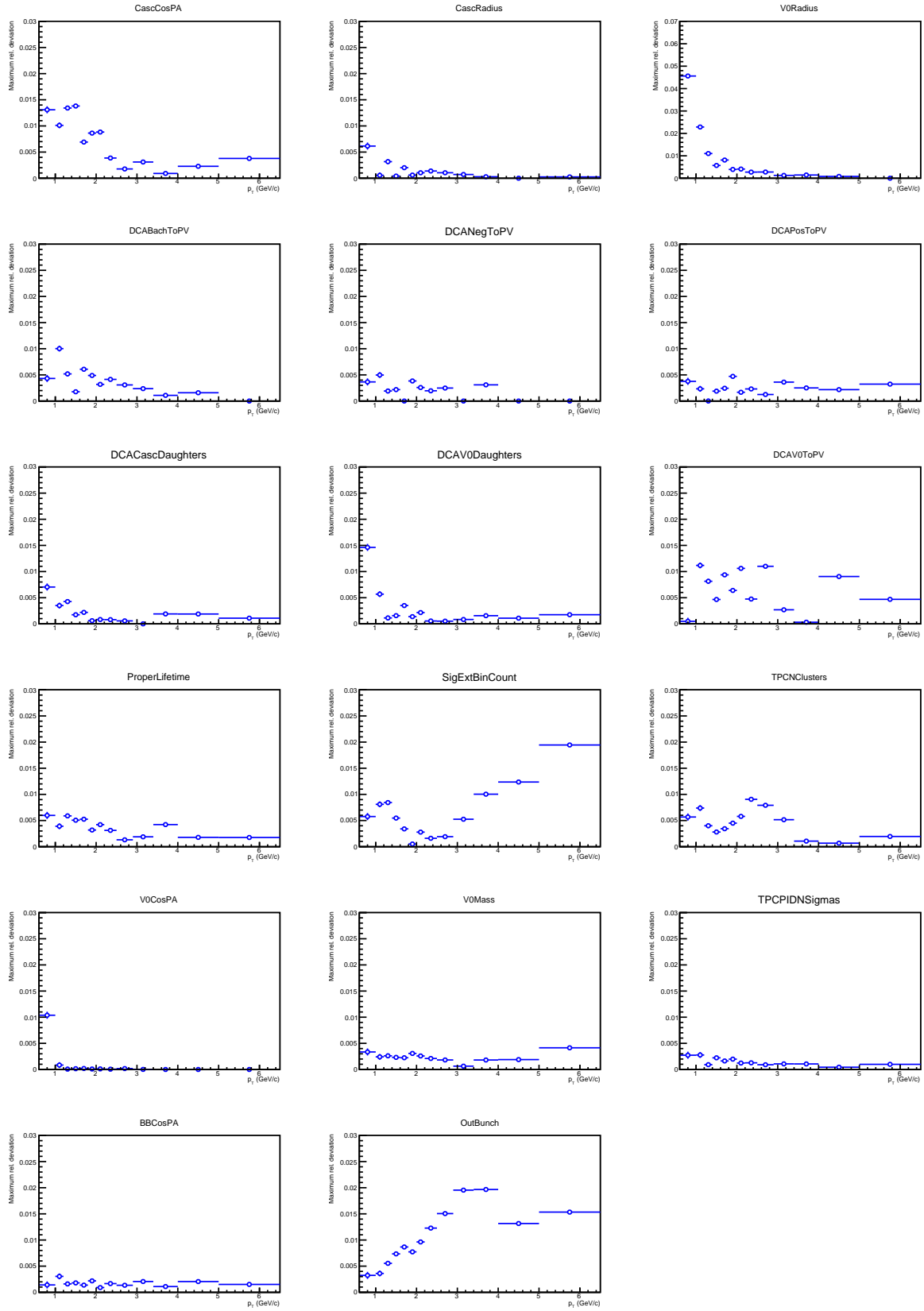
Figure 4.12: Signal loss with cut variation for  $\Xi$ .

Figure 4.13: Ratio of  $p_T$  spectra wrt. the default one for  $\Omega$ .

Figure 4.14: Ratio of  $p_T$  spectra wrt. the default one for  $\Xi$ .

Figure 4.15: Maximum deviation for  $\Omega$ .



Figure 4.16: Maximum deviation for  $\Xi$ .

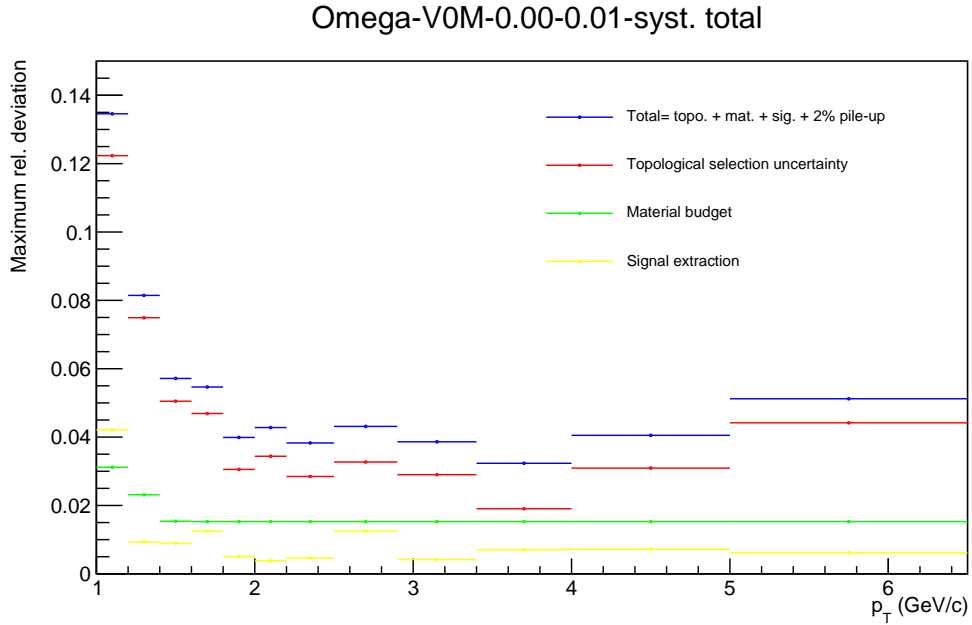


Figure 4.17: Total systematic uncertainty for  $\Omega$  (blue line). The red line is the contribution from cut variation, the green line is the contribution from material budget and the yellow line the contribution from signal extraction. Pile-up (2 %) and int. multiplicity uncertainty (2 %) is not shown but is added to the total.

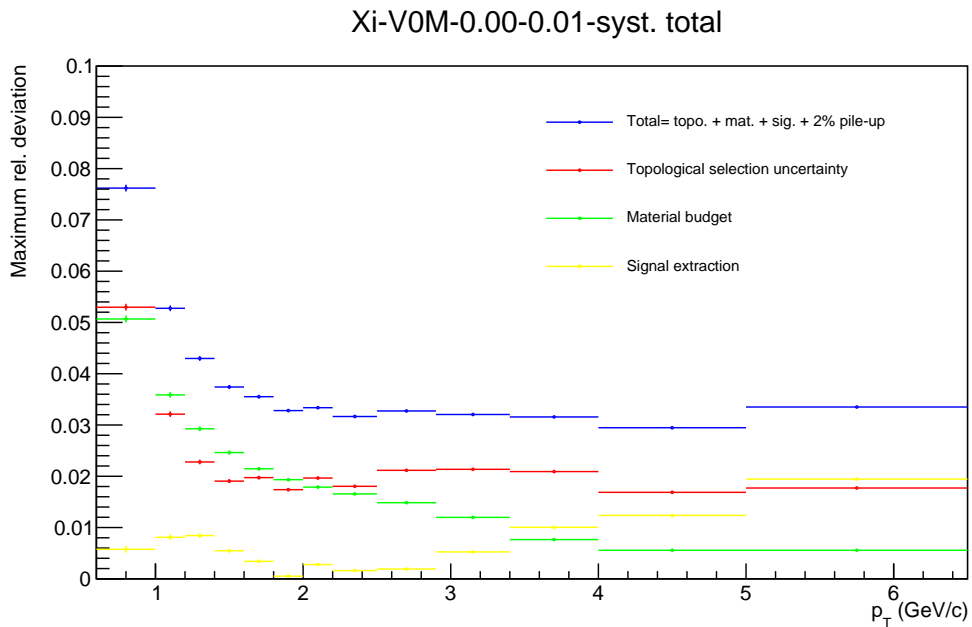


Figure 4.18: Maximum deviation for  $\Xi$ . The red line is the contribution from cut variation, the green line is the contribution from material budget and the yellow line the contribution from signal extraction. Pile-up (2 %) and int. multiplicity uncertainty (2 %) is not shown but is added to the total.

### 4.5.2 Signal extraction uncertainty

To check how the method of signal extraction influences the final yield and to compute its contribution to the systematic uncertainty, two variations were performed.

First, different widths for signal extraction were considered. As a default, the signal region was defined as  $([\mu - 4\sigma_G, \mu + 4\sigma_G])$ , while the background region was  $([\mu - 8\sigma_G, \mu - 4\sigma_G] \cup [\mu + 4\sigma_G, \mu + 8\sigma_G])$ . For  $\Xi$ , variation was done by using  $\pm 5\sigma$  as a loose cut and  $\pm 3\sigma$  as a tight cut, while for  $\Omega$ , values were  $\pm 4.5\sigma$  and  $\pm 3.5\sigma$ . The uncertainty from this is shown in Figures 4.11 and 4.16 in plots titled SigExtBinCount.

Another contribution to systematic uncertainty was estimated by changing the fit functions used for the background. As a default, a linear background is used. Two different background functions were used: 2nd and 3rd degree polynomials. The uncertainty from this is really small, less than 0.3 %. The difference in yields with different background shapes is shown in Figure 4.19 and is added to the total uncertainty for signal extraction.

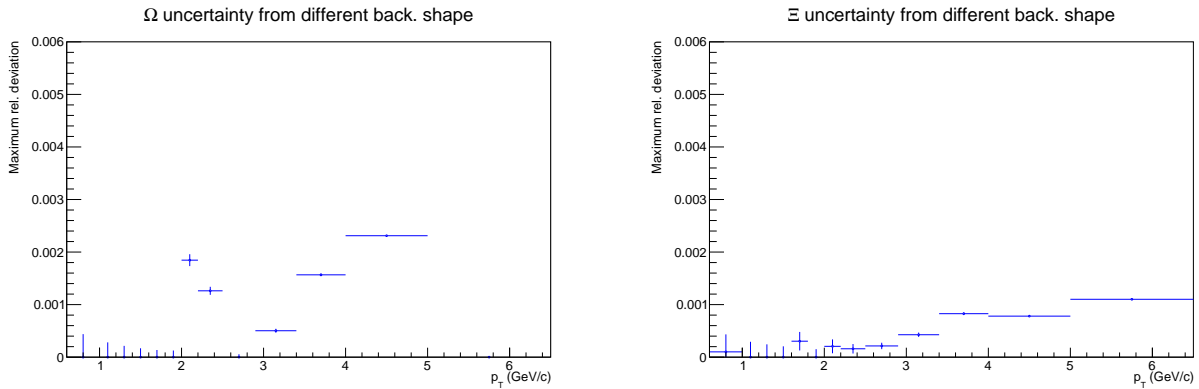


Figure 4.19: Contribution to the systematic uncertainty from using different background fits.

The sums of these two contributions are shown in Figures 4.17 and 4.18, and are marked with a yellow line.

# Chapter 5

## Results

The precise measurement of charged particle transverse momentum spectra reveals insights into both soft and hard interactions. Perturbative Quantum Chromodynamics (pQCD) describes parton-parton interactions at high momentum transfers, known as hard scattering processes. However, a significant fraction of particles in pp collisions, even at LHC energies, arise from soft interactions. QCD's description of soft interactions remains less established compared to hard processes. Current models, like PYTHIA, combine perturbative QCD for hard interactions with phenomenological methods for soft interactions in high-energy hadron collisions. To accurately describe particle production in pp collisions at the highest LHC energies, these models need refinement using data on charged particle production, including multiplicity and transverse momentum distributions, and correlations with charged particle multiplicity.

To study the phenomenon of strangeness enhancement, yields of hyperons are compared to the yields of non-strange hadrons, in this case charged pions. With this comparison, it can be seen how the number of produced hadrons containing strange quark increases with multiplicity. If there was no strangeness enhancement, the increase in produced number of pions and hyperons would be the same, meaning that their ratio should remain constant. But, as it is already shown in the chapter 2, this ratio shows a growing trend in pp collisions.

All important results from this analysis are reported in this chapter in six sections. First, the corrected  $p_T$  spectra as a function of multiplicity will be shown. The corrected spectra are shown for the MB and HM samples. After that, only the HM spectra are fitted and finally integrated to get the final yields. Before showing integrated yields, the final systematics from the fitting and integrating procedures are shown. After integrating the fit function the final integrated yields dependence on multiplicity is shown and compared to other systems. The mean transverse momentum dependence on multiplicity is presented in the section after. To compare the results for  $\Omega$  and  $\Xi$ , the ratios of their yields are calculated and shown, with some

interesting results, but unfortunately with relatively large errors.

Hyperon yield ratios to the pion yields are shown in comparison to results from other colliding systems, and those are the most important result from this analysis. They show clear agreement with the results for other collision systems and energies, and further confirm previously published results. The existence of strangeness enhancement in proton-proton systems is evident and one can conclude that the production of hyperons depends on the final multiplicity of the collision, and not on the initial system size or energy.

## 5.1 Corrected $p_T$ spectra

Transverse momentum spectra provide information about the production mechanisms of particles in collisions. Different processes lead to different distributions of transverse momenta for the produced particles. By analyzing these spectra, the underlying mechanisms responsible for particle production can be studied, which helps in testing theoretical models and understanding the fundamental forces and particles involved.

Transverse momentum spectra are sensitive to the dynamics of QCD processes in high-energy collisions, allowing us to test QCD predictions, such as the behavior of parton distribution functions (PDFs) and the fragmentation of partons into hadrons. Deviations from expected transverse momentum spectra could indicate the presence of new particles or phenomena beyond the Standard Model of particle physics.

The corrected  $p_T$  spectra are shown in Figure 5.1. Only statistical errors are included and are not visible as they are smaller than the marker size. In section 4.4, it was checked that the MB spectra agree with previous results. In bottom panels, the ratios with yields from MB integrated multiplicity are shown. The spectra become harder with increasing multiplicity. Hardening of spectra means that the average transverse momentum shifts to right and there are more particles produced with higher multiplicity. It can also be seen that the slope is different and there are more particles with increasing  $p_T$ . The latter can be seen in the bottom plots.

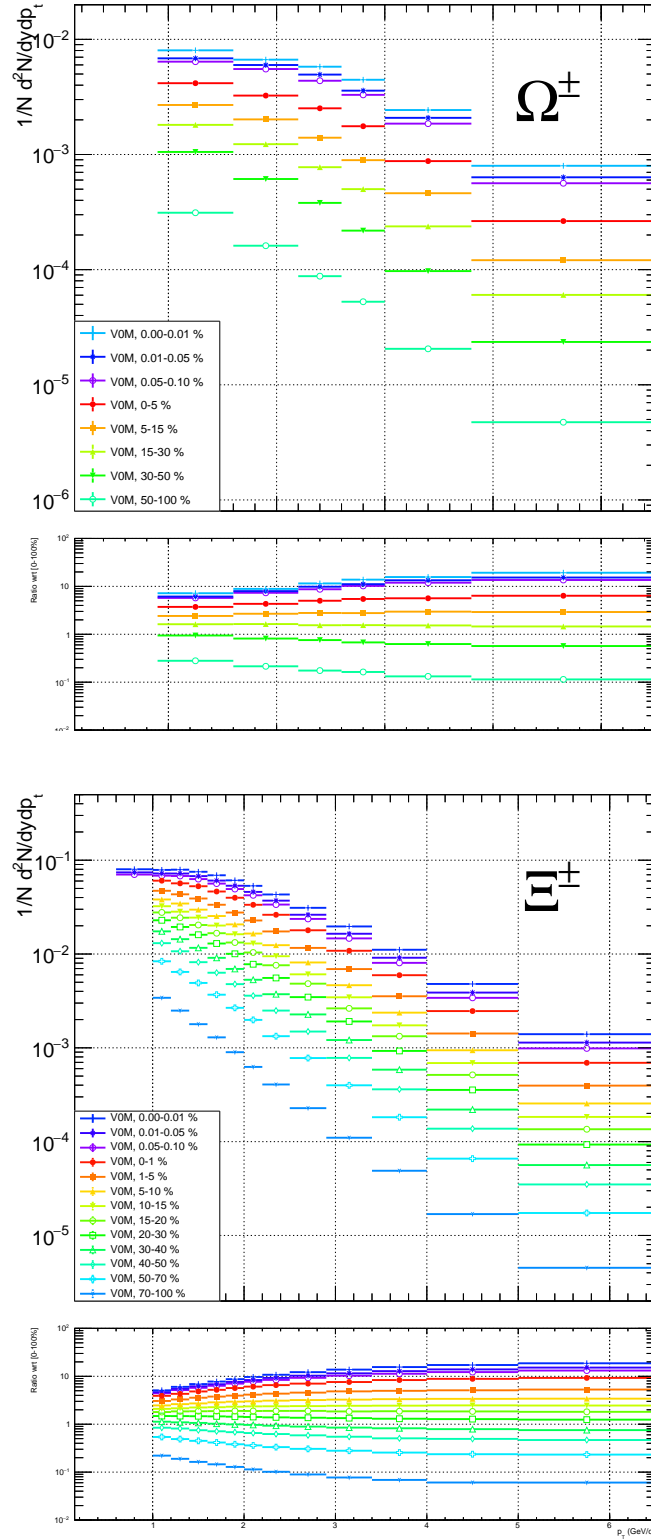


Figure 5.1:  $\Omega^- + \bar{\Omega}^+$  and  $\Xi^- + \bar{\Xi}^+$  corrected  $p_T$  spectra for different V0M multiplicity classes for HM (blue palette) and MB (rainbow palette). In the bottom panel, the ratios with respect to the integrated multiplicity case are shown. Only the statistical errors are shown.

## 5.2 Spectra fitting

To extract the total yield for each multiplicity class, the discrete spectra must be extrapolated to cover the whole  $p_T$  range. The default fitting function is a Levy-Tsallis distribution, used in the previous analyses and shown to best follow spectra shape

$$\frac{d^2N}{dydp_T} = \frac{1}{N_{ev}} \cdot \frac{(n-1)(n-2)}{nT(nT+m(n-2))} \cdot \left(1 + \frac{\sqrt{m^2 + p_T^2} - m}{nT}\right)^{-n},$$

where  $N_{ev}$  is the total number of events,  $n$  and  $T$  are fitting parameters, and  $m$  and  $p_T$  are the mass and the transverse momentum of the particle.

The spectra, with fitting functions, are shown in Figure 5.3. In the bottom panels, ratios of data and the fit are shown. For most  $p_T$  bins the ratio is within 10 percent of one. The  $\chi^2/ndf$  (chi-squared per degree of freedom) was used as a measure of the goodness of fit. It was checked that  $\chi^2/ndf \leq 2$ . The  $\chi^2/ndf$  values are shown in Figure 5.2.

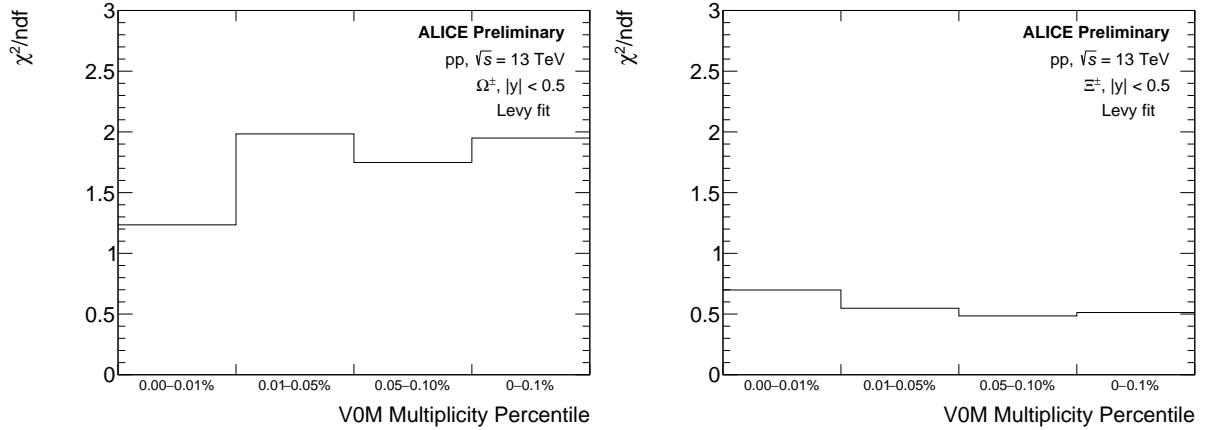


Figure 5.2:  $\Omega^- + \bar{\Omega}^+$  (left) and  $\Xi^- + \bar{\Xi}^+$  (right)  $\chi^2/ndf$  values for different multiplicity classes for the Levy-Tsallis fit.

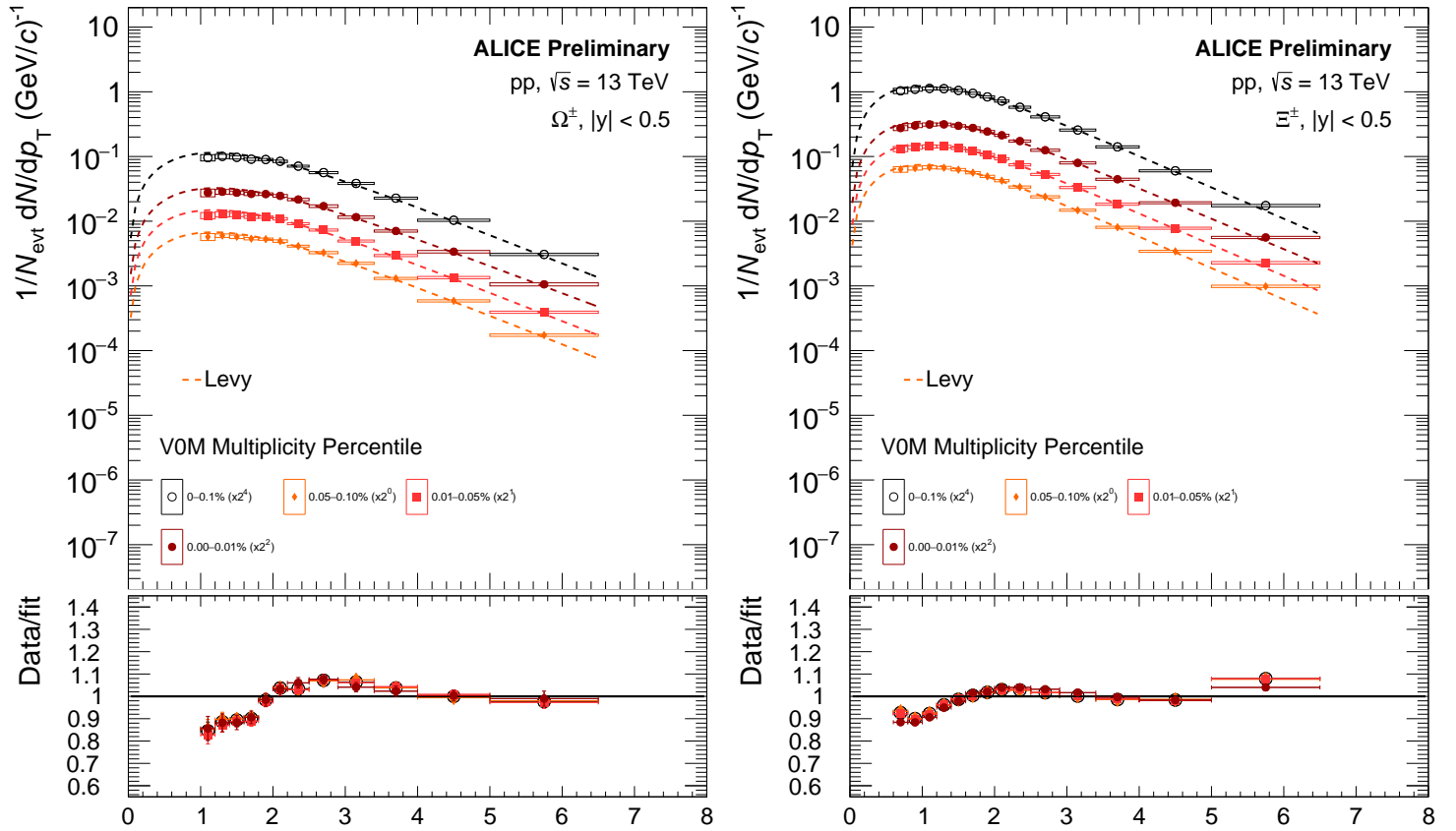


Figure 5.3:  $\Omega^- + \bar{\Omega}^+$  (left) and  $\Xi^- + \bar{\Xi}^+$  (right) corrected  $p_T$  spectra fitted with a Levy-Tsallis distribution. In the bottom panel the ratios of the measured spectra to the fitting function are shown. The error bars are statistical and the error boxes are systematic uncertainties.



### 5.2.1 Total yield uncertainty

To get the statistical uncertainty of the integrated yield, the yield was computed by generating 1000 copies of the original spectra and varying the original yields per  $p_T$  bin with a Gaussian distribution. The mean for this Gaussian was selected to be the original yield and the width was the original statistical error. The integrated yield was then computed for each of these variations and the standard deviation of the computed values is the final statistical uncertainty of the yield. The values of the statistical error, the systematic error and the integrated yield value are in table 5.1.

Two contributions are considered for the systematic uncertainty of the integrated yield. The first is from varying the fit function over the systematic uncertainty of the corrected spectra. Two spectra variations are considered: „extreme high” and „extreme low”. Each point in the  $p_T$  spectra was increased or decreased in value to get the two extreme variations. The integrated yield was then computed for both of them by fitting the Levy-Tsallis function. These yields were then compared to the default yield and the maximum deviation from both was summed, divided by two, and taken as the systematic uncertainty.

The other contribution is related to the extrapolated fraction of the fitted spectra. The spectra was fitted with four alternative functions: Boltzmann, Bose-Einstein,  $m_T$ -exponential and Fermi-Dirac, and compared to the Levy-Tsallis. This adds an additional systematic uncertainty to the final yield. To keep  $\chi^2/ndf \leq 2$ , it was necessary to reduce the fitting range for some fit functions. The final systematic uncertainty is shown in Figure 5.4. The results of the fits are shown in Figure 5.5.

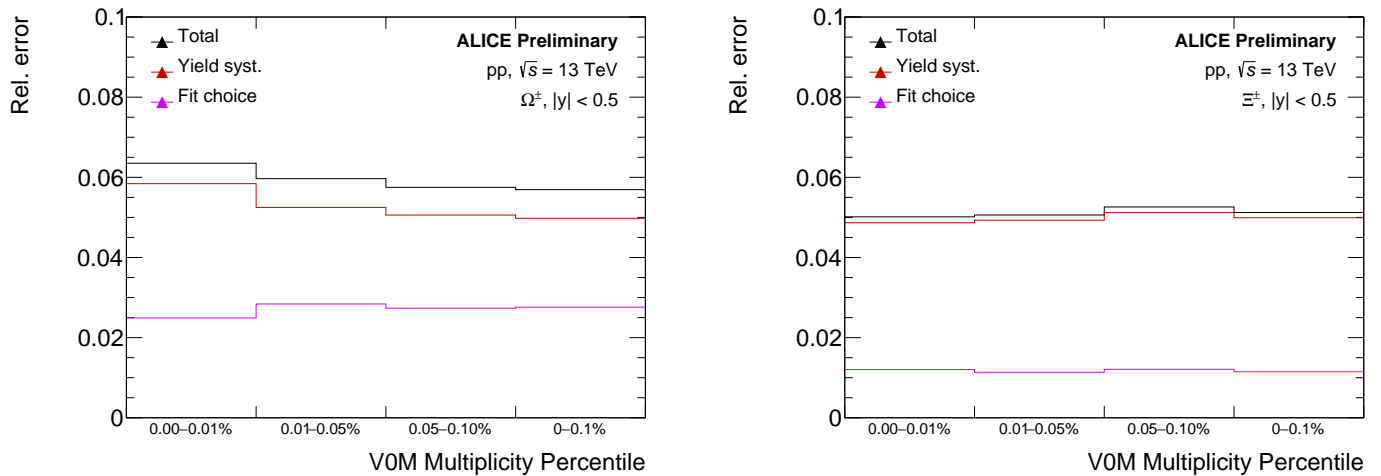


Figure 5.4: Total relative systematic error for integrated yields of  $\Omega$  (left) and  $\Xi$  (right) for different multiplicity classes.

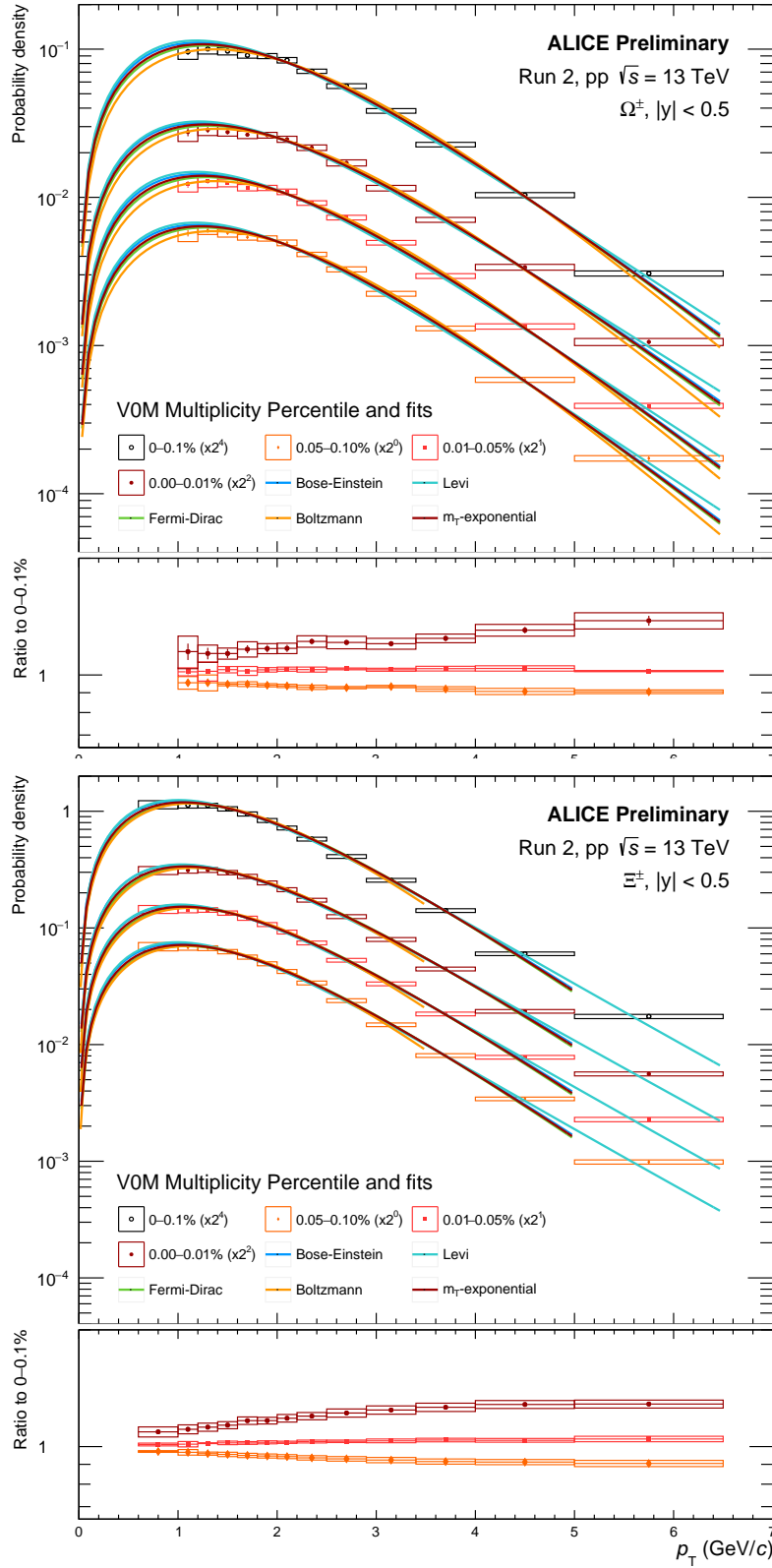


Figure 5.5:  $\Omega^- + \bar{\Omega}^+$  (top) and  $\Xi^- + \bar{\Xi}^+$  (bottom) spectra fitted with different fitting functions. The bottom panels show the ratio of spectra with respect to integrated multiplicity. The boxes represent the systematic uncertainties.

## 5.3 Integrated yields

After fitting the corrected  $p_T$  spectra, they are integrated over the whole  $p_T$  range to get the integrated yield for the selected multiplicity class. Multiplicity is directly correlated to centrality and is evaluated with the V0M multiplicity estimator. The multiplicity values in table 5.1 are taken from [55].

Table 5.1: Integrated yields with final statistical and total systematic errors.

V0M multiplicity	$dN_{ch}/d\eta,  \eta  < 0.5$	$dN/dy \pm \text{Stat.} \pm \text{Syst.} [\times 10^{-3}]$	
		$\Xi^- + \bar{\Xi}^+$	$\Omega^- + \bar{\Omega}^+$
0.00-0.01 %	$36.29 +0.56 -0.46$	$187.11 \pm 0.36 \pm 9.38$	$19.90 \pm 0.17 \pm 1.27$
0.01-0.05 %	$32.57 +0.49 -0.42$	$165.90 \pm 0.22 \pm 8.40$	$17.50 \pm 0.12 \pm 1.04$
0.05-0.10 %	$30.43 +0.47 -0.40$	$154.67 \pm 0.18 \pm 8.14$	$15.93 \pm 0.10 \pm 0.92$

The dependence of the integrated yield on multiplicity is shown in Figure 5.6. The yield for integrated multiplicity is pink, while the published results for the MB analysis at 13 TeV are in blue [1]. A 2nd degree polynomial function is fitted to all points. It is clear from the plots that the points follow the same growing trend.

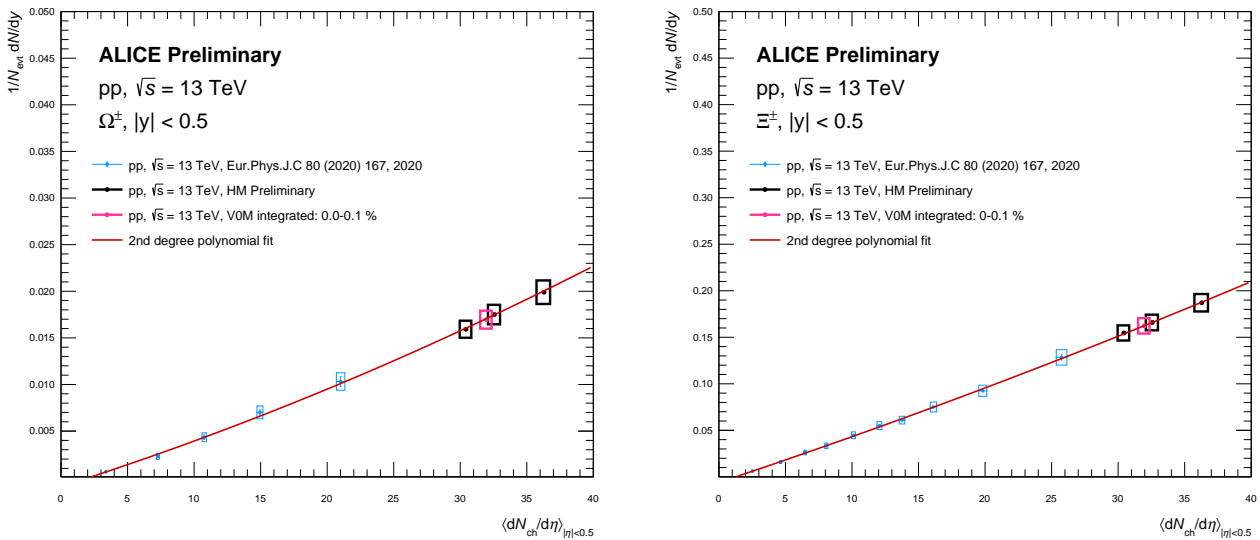


Figure 5.6:  $\Omega^- + \bar{\Omega}^+$  (left) and  $\Xi^- + \bar{\Xi}^+$  (right) integrated yields as a function of multiplicity. The black points are the three HM classes and the pink point is the integrated multiplicity. A 2nd degree polynomial is fitted to the results. The boxes represent the total systematic errors.

Further comparison with results from other systems, proton-lead at 5.02 TeV, lead-lead at 2.76 TeV and 5.02 TeV, is done and shown in the Figure 5.7. Agreement in the yields for different systems is easily seen. We can conclude that the number of produced  $\Omega$  and  $\Xi$  doesn't depend on the system size or the energy of the collision, but only cares about the final state of the event.

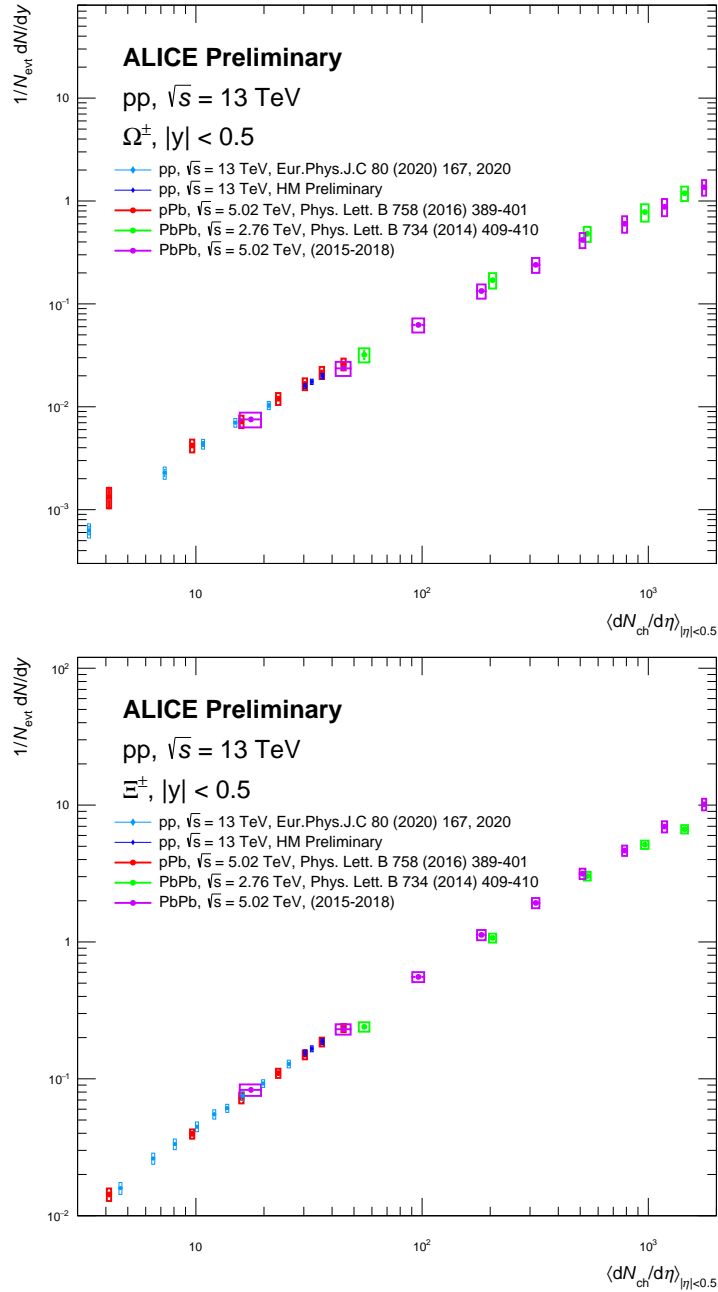


Figure 5.7:  $\Omega^- + \bar{\Omega}^+$  (up) and  $\Xi^- + \bar{\Xi}^+$  (down) normalized  $p_T$ -integrated yields as a function of multiplicity for pp, pPb and PbPb.

## 5.4 The average transverse momentum

The average transverse momentum, often called mean  $p_T$  and denoted as  $\langle p_T \rangle$ , is a statistical measure representing the average amount of momentum carried by particles perpendicular to the beam direction in a given collision event. It is calculated by averaging the transverse momenta of all particles produced in the event.

It provides valuable information about the overall dynamics of a collision process or particle decay. It serves as a key observable in experimental high-energy physics analyses, offering insights into different phenomena. It can give an indication of the typical momentum scale of particles produced in a collision, reflecting the energy scale of the interaction. Different particle production mechanisms lead to distinct distributions of transverse momenta. Studying the average transverse momentum helps us understand the underlying processes responsible for particle creation in high-energy collisions. In heavy-ion collisions, where QGP is formed, particles lose energy as they traverse through it. Deviations in the average transverse momentum from expectations can provide insights into the degree of energy loss and the properties of the QGP.

Mean  $p_T$  as a function of multiplicity is shown in Figure 5.8. It follows a growing trend with increase in multiplicity.

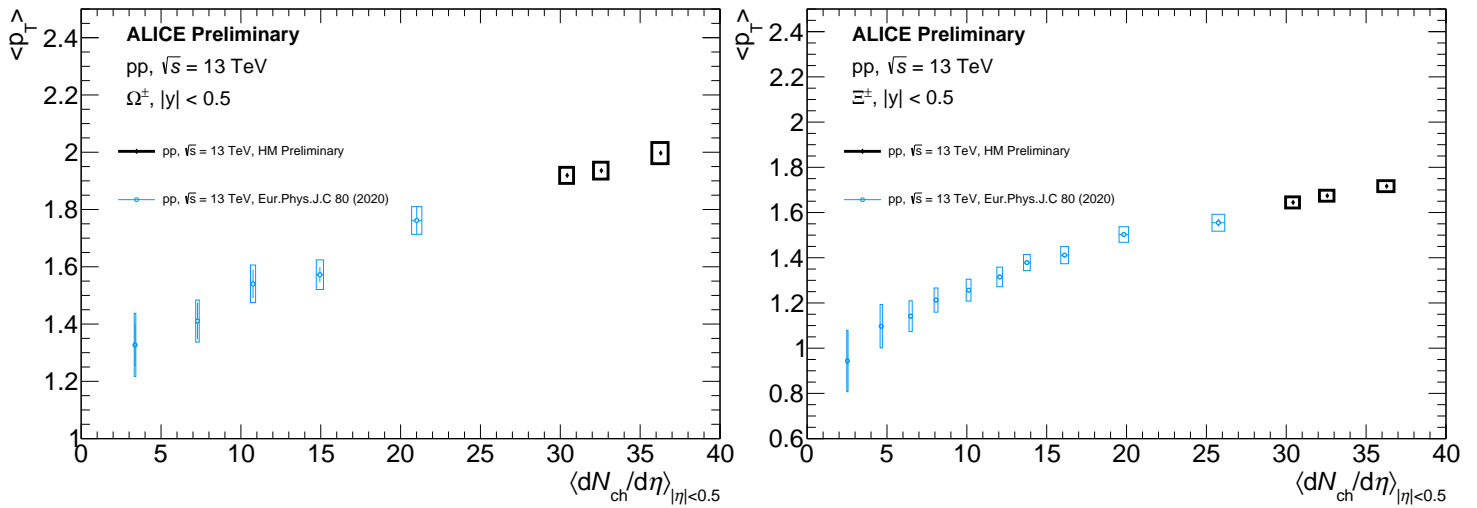


Figure 5.8:  $\Omega^- + \bar{\Omega}^+$  (left) and  $\Xi^- + \bar{\Xi}^+$  (right) mean  $p_T$  as a function of multiplicity. The black points are the three HM classes and the pink point is the integrated multiplicity. The boxes represent the total systematic uncertainties.

## 5.5 $\Omega$ to $\Xi$ ratios

The reason behind doing ratios of  $\Omega$  to  $\Xi$  yields is to check if there is a visible dependence of the ratios on multiplicity. From strangeness enhancement, it can be expected that with higher multiplicities, the ratio of  $\Omega$  to  $\Xi$  would grow, as  $\Omega$  has one strange quark more than  $\Xi$ . This ratio can be calculated by using corrected  $p_T$  spectra and integrated yields.

By calculating the ratio of the spectra, the difference in slopes between  $\Omega$  and  $\Xi$  spectra can be seen. The results for ratios obtained in the MB sample and in the HM sample are shown in Figure 5.9. Some dependence on multiplicity can be seen in the MB case, but the errors are quite large. For HM ratios, there is no clear dependency. The MB ratio shows that the ratio is higher for higher multiplicity classes. This would agree with strangeness enhancement, i.e., more  $\Omega$  relative to  $\Xi$  are produced for higher multiplicities because  $\Omega$  has a higher strange quark content. Also, it can be seen that with higher  $p_T$ , there is a growth in ratio values. This would mean that the slope of  $\Xi$  spectra has a steeper fall than the  $\Omega$  spectra of the same multiplicity. In the bottom plot, one can see that the HM ratio lays on top of the MB ratio, as expected.

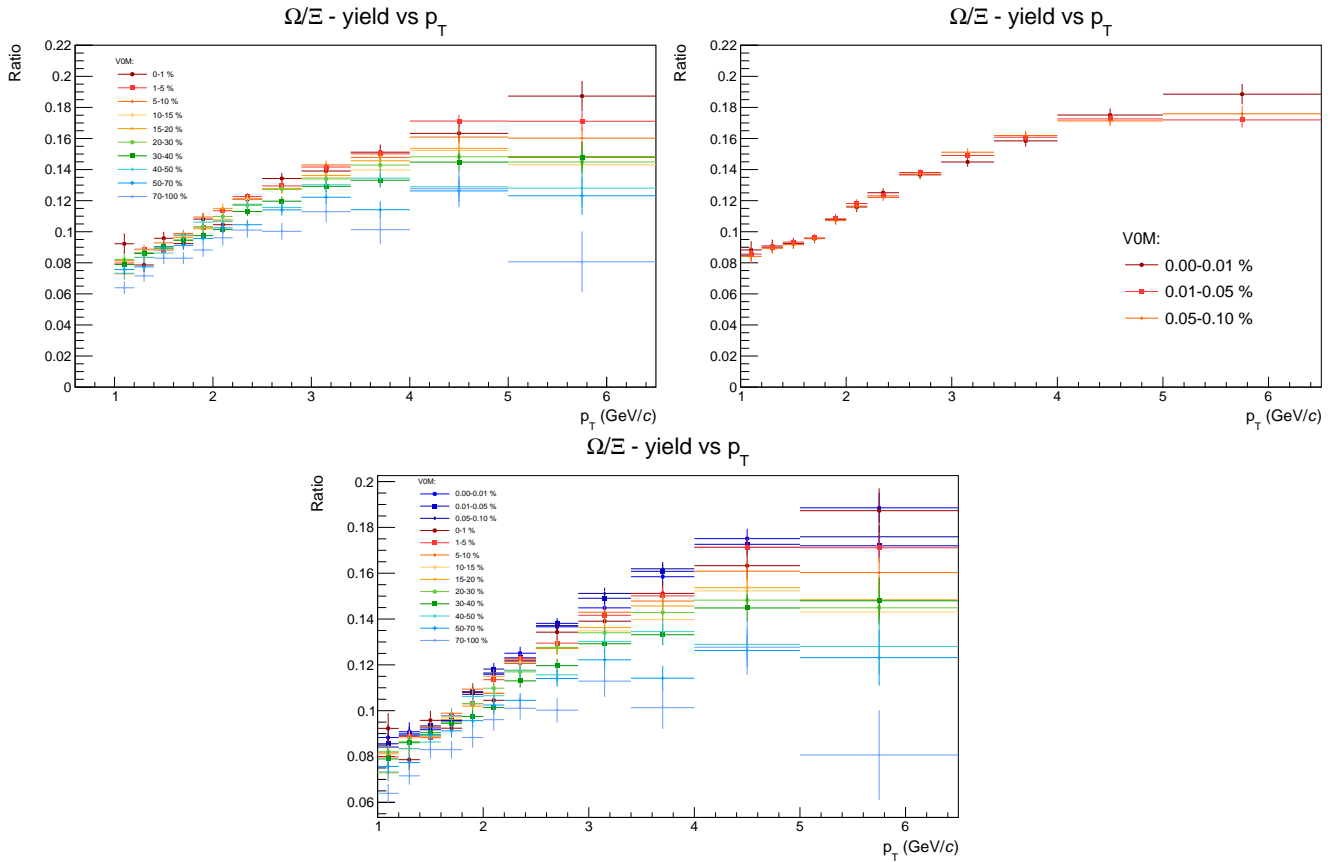


Figure 5.9:  $\Omega$  and  $\Xi$  ratio for different multiplicity classes: MB (left), HM (right) and both (bottom).

Another check for strangeness enhancement is done by calculating the ratios of integrated yields. The result is shown in Figure 5.10. The ratio is done by dividing the  $\Omega$  measured yields with the  $\Xi$  fit function, shown in Figure 5.6. The fit function on the left plot is calculated as a ratio of two fit functions from Figure 5.6. On the right plot, only the x axis is changed to a logarithmic scale. It seems that there is saturation in the ratio, meaning that the effect of strangeness enhancement with greater s quark content is becoming less pronounced. The errors shown are only from  $\Omega$  yields, and are fairly large so a conclusion can't be drawn but this could be interesting for future research. What can be concluded is that the steep rise in this ratio, for lower multiplicities, does not continue to higher values of multiplicities.

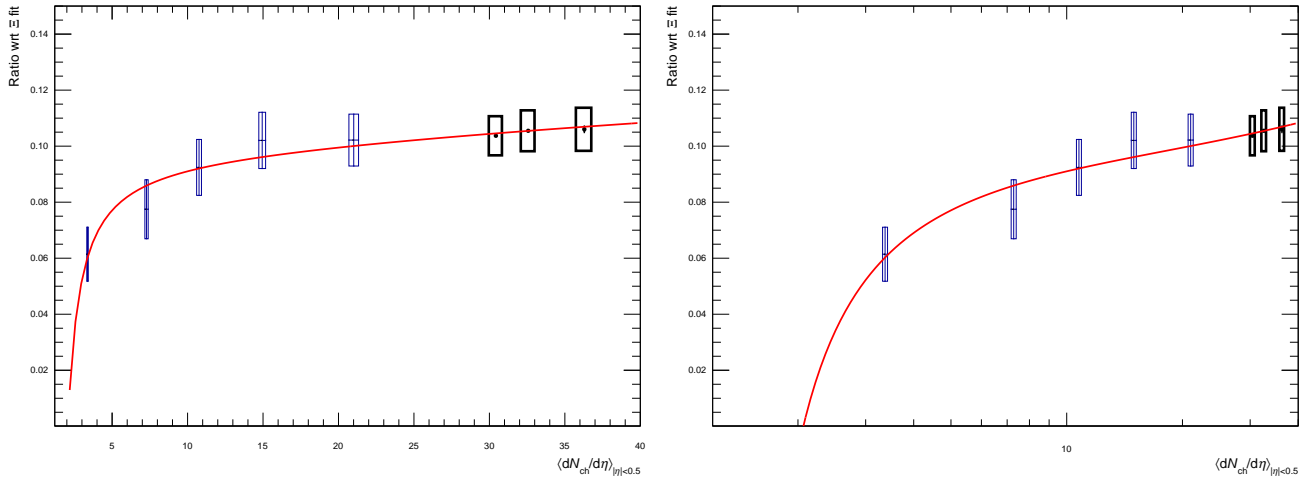


Figure 5.10:  $\Omega$  and  $\Xi$  ratio of integrated yields.

## 5.6 Ratio to pions

To finalize, ratios of integrated yields to integrated yields of pions were calculated. The pion yields are taken from [56] and extrapolated to this data. It was checked that they show agreement with preliminary results for HM pion yields [57]. The ratios are compared with results for other systems [1, 58, 59, 60].

In Figure 5.11, the results for different systems show similar values within one sigma deviations. This clearly indicates that the strangeness production does not depend on system energy or size, but only on the final multiplicity. The possibility of saturation for smaller system is still not completely removed, but there is no sign of it for considered multiplicities.

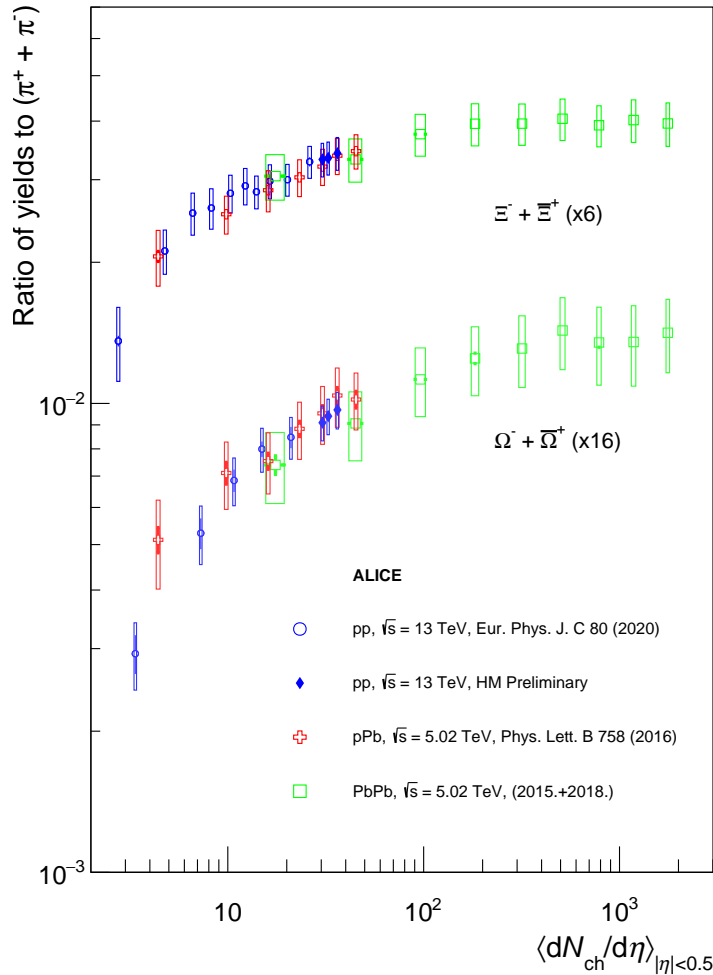


Figure 5.11: Integrated hadron-to-pion ratios as a function of multiplicity measured in pp, p-Pb, and Pb-Pb collisions at energies of 13 TeV and 5.02 TeV. The boxes represent the systematic uncertainties.



In Figure 5.12, results for different systems also show agreement within the uncertainties. Here, we show the consistency between Run I and Run II results. There is a clear growing trend in strangeness production with increase in multiplicity until saturation occurs for more central PbPb collisions.

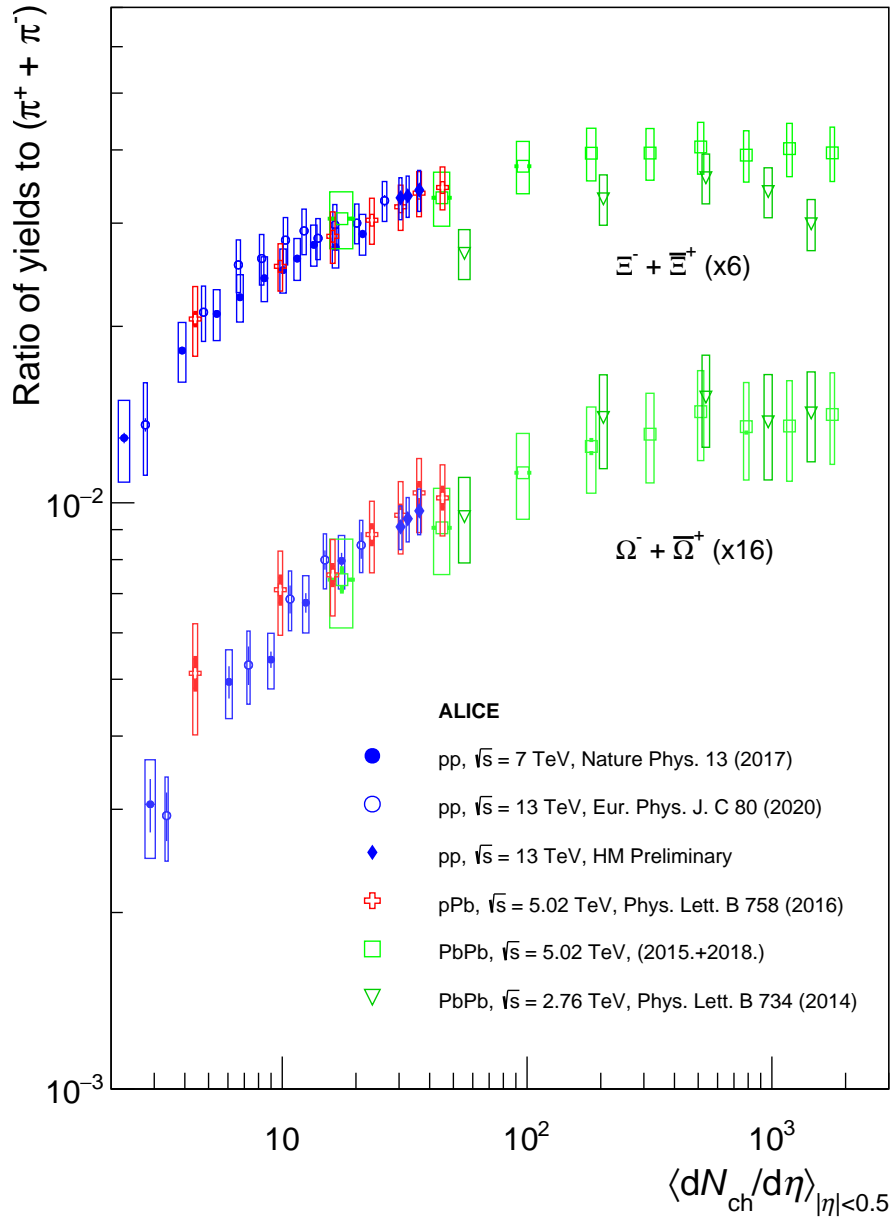


Figure 5.12: Ratio of  $\Xi$  and  $\Omega$  yields with pion yields for different systems, including Run I pp and PbPb data.

# Chapter 6

## Conclusion

The motivation for this research stemmed from investigating the strangeness enhancement phenomenon in proton-proton collisions, which could potentially indicate the formation of quark-gluon plasma in the initial phase following the collision. To explore this, the production of multi-strange hyperons, Xi and Omega, was analyzed using data collected by the ALICE detector. Specifically, collisions with the highest multiplicities, i.e., with the highest number of produced charged particles in the final state, were considered to allow comparison with results from proton-lead and lead-lead collisions.

First, transverse momentum spectra were computed, showing results consistent with expectations: with higher multiplicity, the spectra become harder. This suggests that as the multiplicity increases, the number of produced hyperons also increases, and the relative number of hyperons grows for higher transverse momentum.

After fitting the spectra, the dependence of the integrated yield on multiplicity was examined. Integrated yield refers to the number of produced hyperons per collision in a certain multiplicity bin. These yields exhibit a rising trend with increasing multiplicity, consistent with previous results obtained for proton-proton collisions. Notably, the trend appears steeper than linear and was well-fitted with a second-order polynomial, indicating a non-linear dependence of hyperon production on multiplicity. Comparison with other systems, such as proton-lead and lead-lead collisions at different collision energies, showed agreement within uncertainties. High-multiplicity proton-proton and proton-lead collisions demonstrated a particularly close agreement, suggesting that hyperon production is independent of the initial system size. Similarly, an agreement with lead-lead results was observed.

The average transverse momentum was found to follow the established trend, increasing with higher multiplicities. This correlation was expected, as higher multiplicities correspond to more central collisions, resulting in more hard interactions and higher-energy particle pro-

duction, thus carrying larger momenta. These average transverse momentum values can aid in refining models that combine perturbative QCD for hard interactions with phenomenological methods for soft interactions. In the past, there was a significant disparity between model predictions and real results for hyperon production in high-energy collisions, making these findings particularly useful, especially considering the previously limited statistics for multi-strange hyperons.

Comparison of the Xi and Omega spectra and integrated yields was conducted through ratios, revealing some dependence of particle yields on multiplicity. The ratios showed a slow increase with higher multiplicity, suggesting a relatively greater production of Omega compared to Xi, in agreement with strangeness enhancement. However, significant errors in these ratios prevented clear conclusions. Analysis of integrated yield ratios indicated a less steep growth trend in Omega/Xi yields compared to previous results from proton-proton collisions, hinting at the possibility of saturation. This would be something worth considering in the future, as the saturation is not predicted by strangeness enhancement.

The final results focused on the ratios of hyperon to charged pion yields, providing a clear observation of strangeness enhancement. The relative hyperon production shows a fast growing trend at lower multiplicities, with saturation occurring in more central lead-lead collisions at higher multiplicities. The results from this research follow the growing trend and are consistent with those from proton-lead and lead-lead systems, suggesting that hyperon production is dependent on final multiplicity rather than initial system size or energy. While predictions suggested possible saturation in the proton-proton system, this was not observed, indicating a strong agreement between results from different systems and supporting the hypothesis of a shared production mechanism for hyperons. These findings are important for the development of improved prediction models and for refuting theoretical models predicting saturation. Unfortunately, these results alone cannot definitively answer the question of quark-gluon plasma production in proton-proton collisions, but they undoubtedly represent progress in that direction.

# Prošireni sažetak

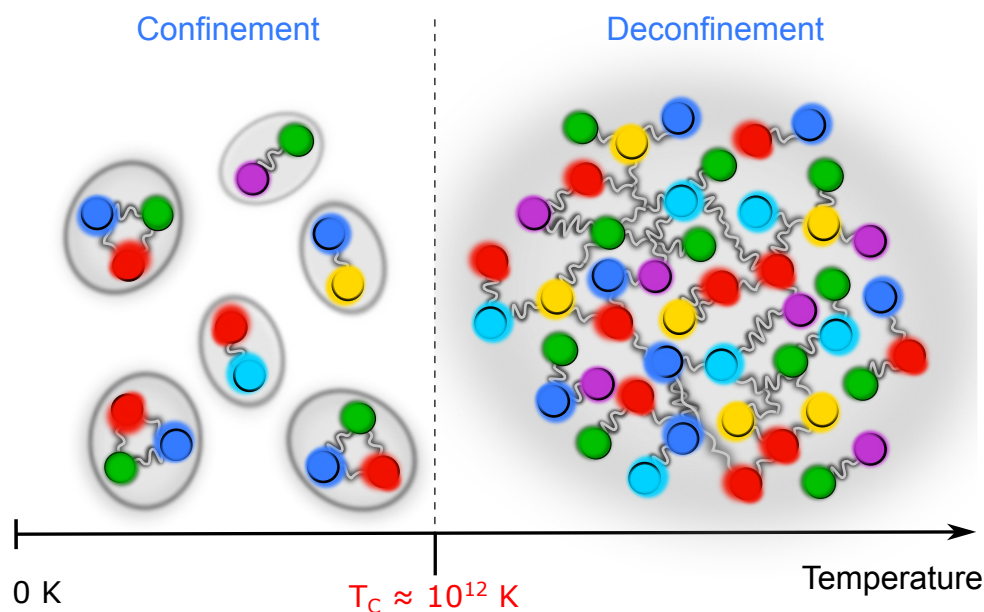
## Uvod

Jedna od glavnih tema visokoenergetske fizike je proučavanje svojstava kvarkovsko-gluonske plazme (QGP) koja se stvara pri ultra-relativističkim sudarima teških iona. kvarkovsko-gluonska plazma je stanje materije u kojemu su kvarkovi i gluoni u nevezanom stanju, tj. asimptotski su slobodni. Vjeruje se da je Svemir u neposrednom trenutku nakon Velikog praska, prije stvaranja prve hadronske materije, bio upravo u tom obliku, što objašnjava veliki interes za istraživanjem svojstava takve materije. Postojanje kvarkovsko-gluonske plazme je predviđeno prije 40-ak godina, te je prvi puta detektirano u Pb-Pb sudarima 2000. godine na CERN-u. Kako je za stvaranje QGP-a potrebna visoka temperatura i/ili visoka gustoća materije (slika 7.1), očekivano je da će se to stanje postići u sudarima teških iona dok u sudarima dva protona neće doći do stvaranja te zanimljive faze materije.

Za proučavanje svojstava QGP-a promatraju se fenomeni koji su takozvani potpisi QGP-a. Uzrok postojanja svih tih fenomena bi bilo nastajanje QGP-a direktno nakon sudara te ako nije došlo do stvaranja QGP-a u sudaru, ti fenomeni ne bi bili vidljivi. Neki od potpisa QGP-a su grebenasta struktura (eng. ridge), potisnuće mlazova (eng. jet suppression), potisnuće kvarkonija (eng. suppression of heavy quarkonium) itd. Kako se na LHC-u postižu sve veće energije sudara, primijećeno je da se većina ovih potpisa QGP-a vidi i u pp sudarima visokog multipliciteta. Jedan od potpisa koji je i glavna tema ovog istraživanja je povećanje stranosti (eng. strangeness enhancement), koji je nedavno opažen u pp sudarima pri energiji od 13 TeV-a [1].

## Fizika stranosti

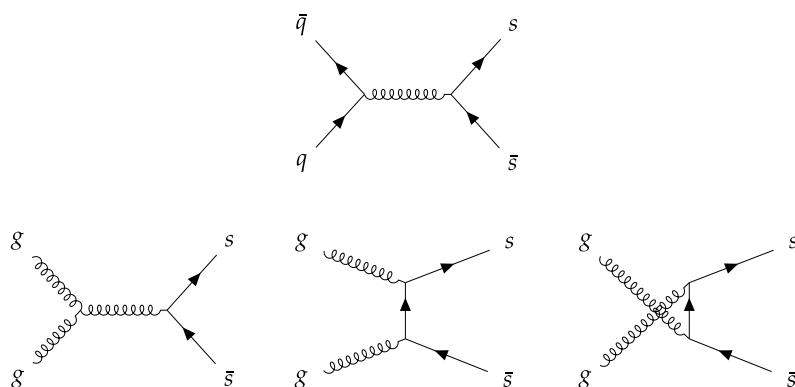
Sva materija oko nas je izgrađena od samo dvije vrste kvarkova, gornjih i donjih kvarkova (eng. up and down quarks), dok strane kvarkove ne nalazimo u prirodi već nastaju samo u ekstremnim uvjetima kao što su npr. neutronske zvijezde ili nakon visokoenergetskih sudara, jer hadroni



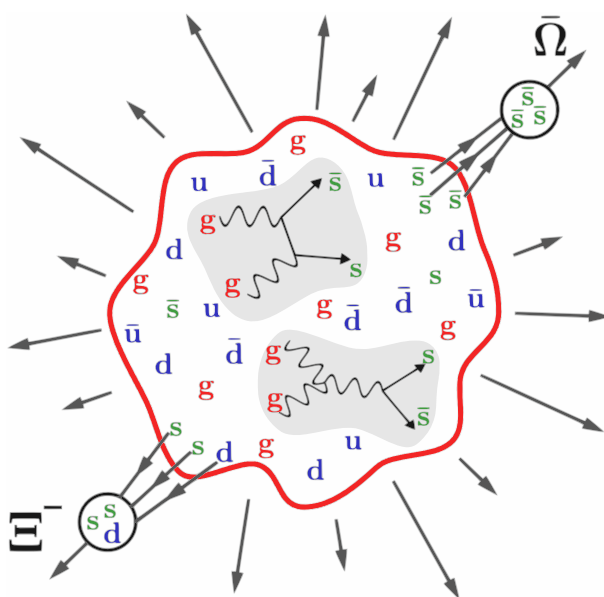
Slika 7.1: Pojednostavljeni prikaz prelaska obične hadronske materije u kvarkovsko-gluonsku plazmu. [14]

koji sadrže jedan ili više stranih kvarkova nisu stabilni i imaju kratko vrijeme poluživota. U početnoj fazi nakon visoko energetskog sudara, hiperoni (hadroni s jednim ili više stranih kvarkova) nastaju nakon tvrdih (perturbativnih) raspršenja partona (kvark ili gluon) preko procesa anihilacije kvarkova ili fuzije gluona (slika 7.2). Ovi procesi dominiraju pri stvaranju hiperona visokih transversalnih impulsa dok pri nižim dominiraju neperturbativni procesi. U modelima fragmentacije struna (eng. string fragmentation) proizvodnja stranih kvarkova je potisnuta naspram proizvodnje lakših kvarkova, jer strani kvark ima veću masu. No ta teorija ne opisuje dobro višak proizvedenih stranih čestica pri sudarima hadrona. Nakon predlaganja postojanja fenomena povećanja stranosti prvotno je primijećeno da u sudarima teških iona s povećanjem multipliciteta dolazi do povećane proizvodnje stranih čestica s obzirom na druge čestice.

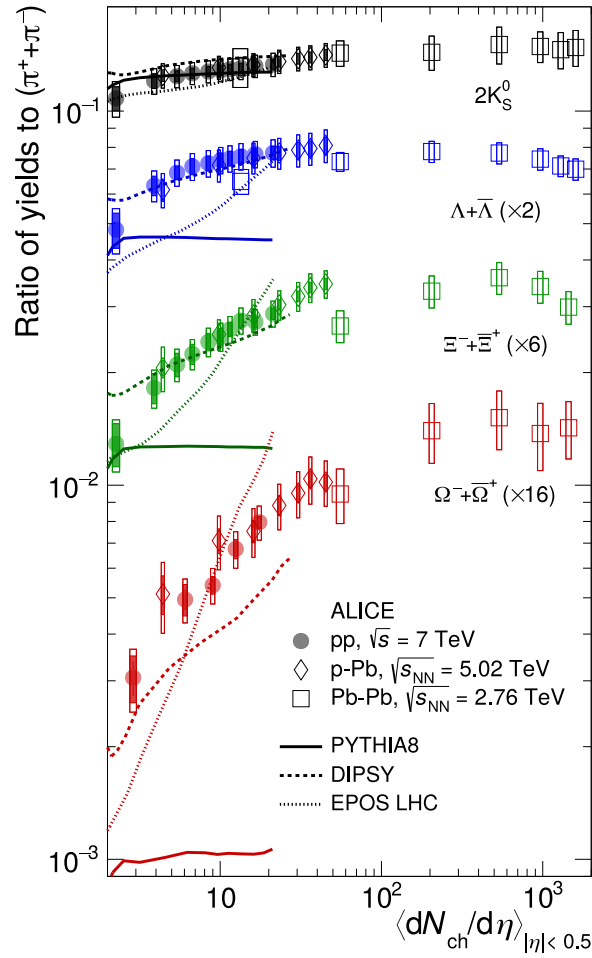
Kako sami razlog zbog kojeg dolazi do takvog fenomena nije bio poznat, najprihvaćenija teorija je bila da do toga dolazi zbog kvarkovsko-gluonske plazme koja se stvara direktno nakon sudara teških iona i smatrao se jednim od mogućih potpisa QGP-a. Teoriju su prvi puta predložili Rafaelski i Muller 1982. godine tvrdeći da bi se u slučaju nastajanja kvarkovsko-gluonske plazme proizvelo više stranih čestica nego kada bi imali obični hadronski plin. Masa stranog kvarka je dovoljno malena da bi se mogao proizvesti kao kvark-antikvark par pri termalnim fluktuacijama u kratkom razdoblju nakon sudara dok postoji kvarkovsko-gluonska plazma (slika 7.3). Povećanje stranosti je prvo primijećeno u sudarima teških iona, no s povećanjem energija sudara protona, i samim time povećanjem multipliciteta, vidi se da pri pp sudarima

Slika 7.2: Feynmannovi dijagrami koje prikazuju stvaranje  $s\bar{s}$  parova.

visokog multipliciteta dolazi do povećanja proizvodnje hadrona sa stranim kvarkovima. Kako se smatra da je pojava kvarkovsko-gluonske plazme moguća samo u sudarima teških iona navedeni fenomen se više ne smatra potpisom QGP-a te teorija iza same pojave više nije toliko prihvaćena.

Slika 7.3: Pojednostavljena vizualizacija stvaranja  $\Xi^-$  i  $\bar{\Omega}^+$  hiperona hadronizacijom iz QGP-a.

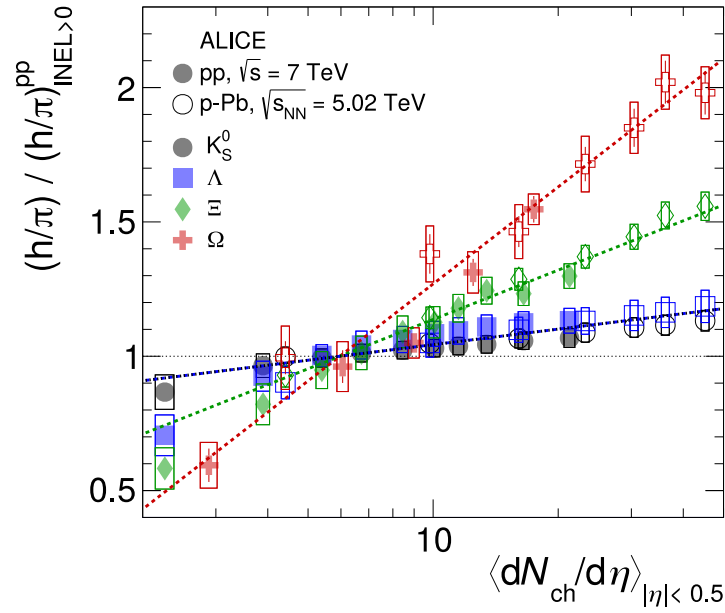
Uz energije na LHC-u od 13 TeV pri proton-proton sudarima postižu se događaji multipliciteta usporedivih s onima pri perifernim sudarima teških iona. U centralnim olovo-olovo (Pb-Pb) sudarima se proizvede maksimalno oko 20 000 nabijenih čestica u rasponu pseudo-rapiditeta  $|\eta| < 0.5$  dok za periferne Pb-Pb i pp sudare visokog multipliciteta nastaje red veličine 100 takvih čestica. Time se može promatrati trend koji prati proizvodnja stranih hadrona na rasponu od pp sudara niskog multipliciteta do centralnih olovo-olovo sudara. Rezultati pokazuju ras-



Slika 7.4: Omjer broja proizvedenih hiperona i broja proizvedenih nabijenih piona u ovisnosti u multiplicitetu ( $dN_{ch}/d\eta$ ) mjereni u području  $|\eta| < 0.5$ . [2]

tući trend dok ne dođe do saturacije pri vrlo visokim multiplicitetima centralnijih olovo-olovo sudara (slika 7.4).

Također je pokazano da je fenomen povećanja proizvodnje stranosti to izraženiji što hadron ima veći broj stranih kvarkova (slika 7.5). To znači da će se povećanjem multipliciteta događaja više povećati relativni broj nastalih Omega hiperona (Omega ima 3 strana kvarka) naspram povećanja broja nastalih Ksi hiperona (Ksi ima 2 strana kvarka). Pokazano je da proizvodnja stranosti (broj stranih čestica po jedinici pseudorapiditeta) na različitim energijama pp, p-Pb i Pb-Pb sudara (za pp od 0.9 do 13 TeV-a, za p-Pb 5.02 i 8.16 TeV-a, Pb-Pb 2.76 i 5.02 TeV-a) daje slične rezultate pri jednakim multiplicitetima što vodi na zaključak da proizvodnja stranih hadrona ne ovisi o početnom sistemu ni energiji samog sudara već samo o konačnom stanju sustava. Mjerenja su rađena za hiperone: Lambda (uds), kratkoživući Kaon (ds), Ksi (dss) i Omega (sss) i njihovih antičestica, te će se u ovom istraživanju raditi analiza samo za Ksijeve i



Slika 7.5: Omjer proizvedenih hiperona i piona normaliziran na INEL > 0 slučaj. [2]

Omge gdje postoji najmanje obrađenih podataka, jer su to najteži od navedenih hiperona te se zbog toga proizvode u najmanjem broju.

Proizvodnja stranih čestica u sudarima teških iona se danas opisuje statističkim hadronskim (termalnim) modelima. U centralnim sudarima teških iona proizvodnja stranih hadrona je konzistentna s proizvodnjom u hadronskom plinu u termalnoj i kemijskoj ravnoteži te se može opisati velekanonskim ansamblom. U perifernim sudarima, proizvodnja stranih čestica naspram piona opada i teži prema brojkama dobivenima za pp sudare za čija predviđanja se isto koriste statistički modeli. Koriste se dodatni modeli dodani na čisti velekanonski model kao što su kanonsko potiskivanje stranosti (eng. strangeness canonical suppression) i jezgra-korona superpozicija (eng. core-corona superposition) modeli, koji uspješno opisuju potisnuće stvaranja stranih čestica u malim sustavima. No, to još uvijek ne opisuje mikroskopsko porijeklo povećanja proizvodnje stranih čestica te bi bolja statistika za male sustave mogla pridonijeti boljem razumijevanju.

Kako je primijećen trend rasta povećanja proizvodnje stranosti od pp sudara niskog multipliciteta sve do centralnih Pb-Pb sudara gdje dolazi do zasićenja, moglo bi se zaključiti da je u pozadini proizvodnje stranih čestica isti fizikalni princip koji bi to sve zajedno mogao objasniti. Potrebno je istražiti područje pp sudara s visokim multiplicitetima, gdje je trenutno statistika slaba, kako bi se vidjelo hoće li se trend rasta nastaviti ili će doći do zasićenja kao što je predviđeno velekanonskim statističkim modelom, što je i primijećeno u slučaju Pb-Pb sudara. Također, postoji izrazita sličnost pri proizvodnji stranih čestica u pp, p-Pb i Pb-Pb suda-

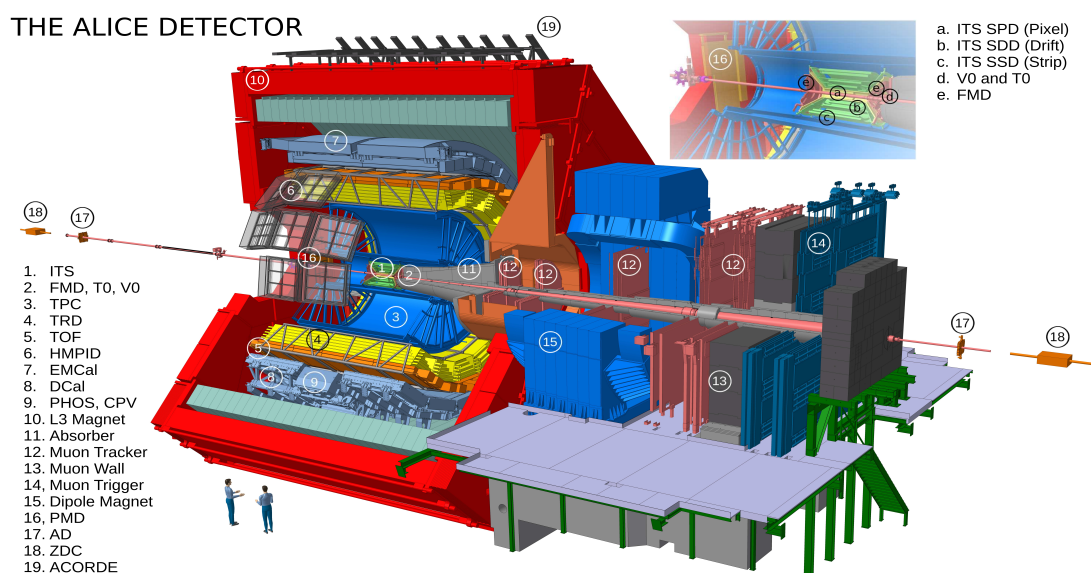


rima koja je objašnjena postojanjem QGP-a te se dovodi u pitanje nastaje li QGP i u sudarima protona, a ne samo teških iona.

## Eksperiment

Veliki hadronski sudarivač (eng. Large Hadron Collider (LHC)) na CERN-u je najveći sudarivač čestica na svijetu koji postiže energije do 13 TeV-a u sustavu centra mase nukleona. Na samom LHC-u se nalazi ukupno osam detektora od kojih je jedan i ALICE (A Large Ion Collider Experiment) detektor korišten za prikupljanje podataka koji će se koristiti za ovo istraživanje (slika 7.6). ALICE detektor je specijaliziran za promatranje sudara teških iona te ima izvrsnu sposobnost identifikacije čestica. Pravilno raspoznavanje čestica je bit ovog istraživanja što je razlog zašto se analiza radi na podacima prikupljenima upravo ALICE detektorom. ALICE se sastoji od 18-25 (ovisno o godini) manjih detektora koji zajedno daju informacije o masi, brzini i signalu čestica nastalih nakon sudara.

Za identifikaciju stranih čestica najbitnija su dva detektora: komora vremenske projekcije (eng. Time projection chamber (TPC)) i unutarnji sustav praćenja (eng. Inner tracking system (ITS)). ITS je centralni detektor koji se nalazi oko cijevi kroz koju prolazi akceleratori snop te se sastoji od 6 slojeva silikonskih detektora. Koristi se za precizno određivanje primarnih i sekundarnih točaka interakcije (verteksa), za praćenje čestica malenog impulsa te za poboljšanje prostorne rezolucije putanja čestica rekonstruiranih pomoću TPC-a. Precizno određivanje



Slika 7.6: Shematski prikaz ALICE detektora za vrijeme trajanja Run II. [42]

položaja primarnih i sekundarnih verteksa je vrlo bitno u slučaju identifikacije težih hiperona jer se vrlo brzo raspadnu. TPC je veliki cilindrični drift detektor odgovoran za praćenje i raspoznavanje čestica. Uz njih vrijedi spomenuti i V0 detektor pomoću kojeg se određuje centralnost, a time i multiplicitet događaja.

## Metodologija

Podaci su prikupljeni kroz cijelu 2016.-2018. godinu ALICE detektorom na LHC-u, prilikom proton-proton sudara energije 13 TeV-a u sustavu centra mase. Analiza je napravljena na dva seta podataka: podaci s visokim multiplicitetom i podaci s zadovoljenim minimalnim uvjetima (eng. minimum bias). Podaci s visokim multiplicitetom su glavna tema ovog istraživanja, dok je drugi set podataka korišten kao provjera da analiza daje rezultate kompatibilne s objavljenim.

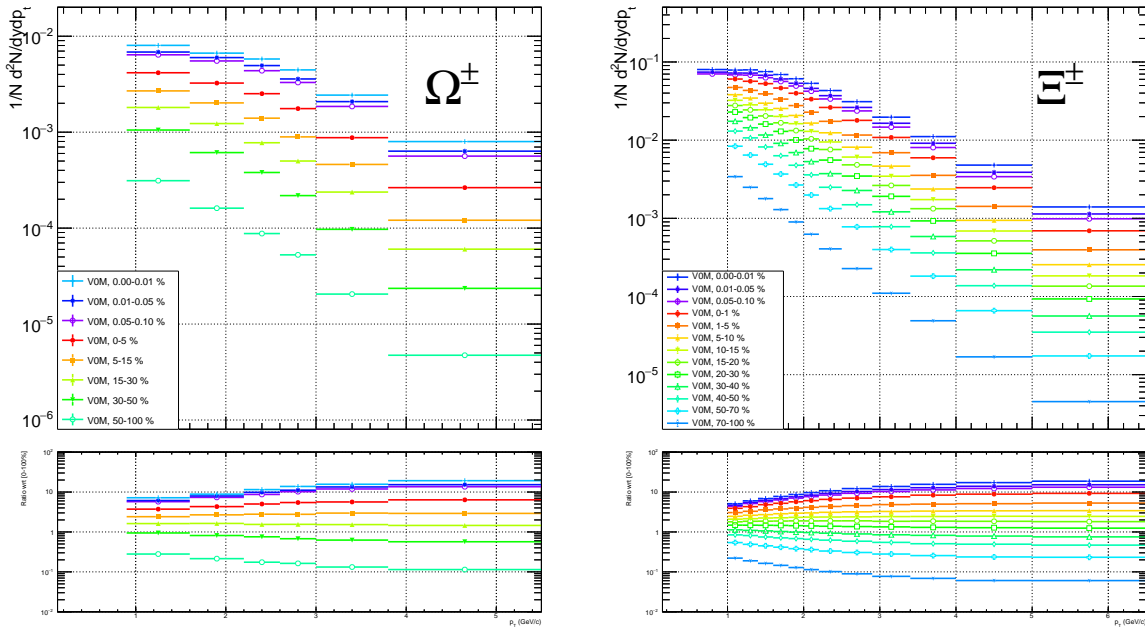
Kako Omega i Ksi hiperoni imaju kratko vrijeme poluživota oni se moraju prepoznati preko čestica na koje se raspadaju. Putanje iz ITS-a i TPC-a se spajaju te se na njih postavlja nekoliko kriterija uvjetovanih geometrijom raspada kako bi se odredili mogući kandidati. Raspoznavanje čestica se radi na podacima iz TPC-a gdje se gleda specifični energijski potpis za čestice na koje su se hiperoni raspali. Nakon toga se vrši analiza invarijantnih masa čestica, kako bi se odredio broj traženih hiperona u pojedinom rasponu transverzalnih impulsa i u različitim intervalima multipliciteta. Pri analizi se na već probrane podatke postavlja standardizirani niz uvjeta, tzv. rezova, kako bi se dobili što pouzdaniji rezultati i kako bi eliminirali lažne kandidate. Nakon toga se rade korekcije na efikasnost i odaziv detektora pomoću računalno generiranih Monte Carlo podataka. Za kraj ostaje odrediti sistematske greške i uključiti ih u konačni rezultat.

Nakon prvotne selekcije podataka koja se radi direktno na podacima iz detektora, ostaje oko 860 milijuna događaja visokog multipliciteta. Ta prva prilagodba podataka se radi na računalnoj mreži CERN-a zvanoj Grid pomoću tzv. lego vlakova (eng. lego trains), unutar programskog paketa ROOT. Nakon toga se analiza nastavlja lokalno na računalu pomoću AliRoot paketa.

ROOT je modularni znanstveni okvir softvera baziran na programskom jeziku C++ razvijen na CERN-u. Pogodan je za obradu velike količine podataka, statističke analize te spremanje podataka. AliRoot je računalni paket baziran na ROOT-u koji se koristi za obradu i pristup podacima s ALICE detektora. U njemu su ugrađene funkcije koje koriste podsustave ALICE detektora za identifikaciju čestica.

## Rezultati

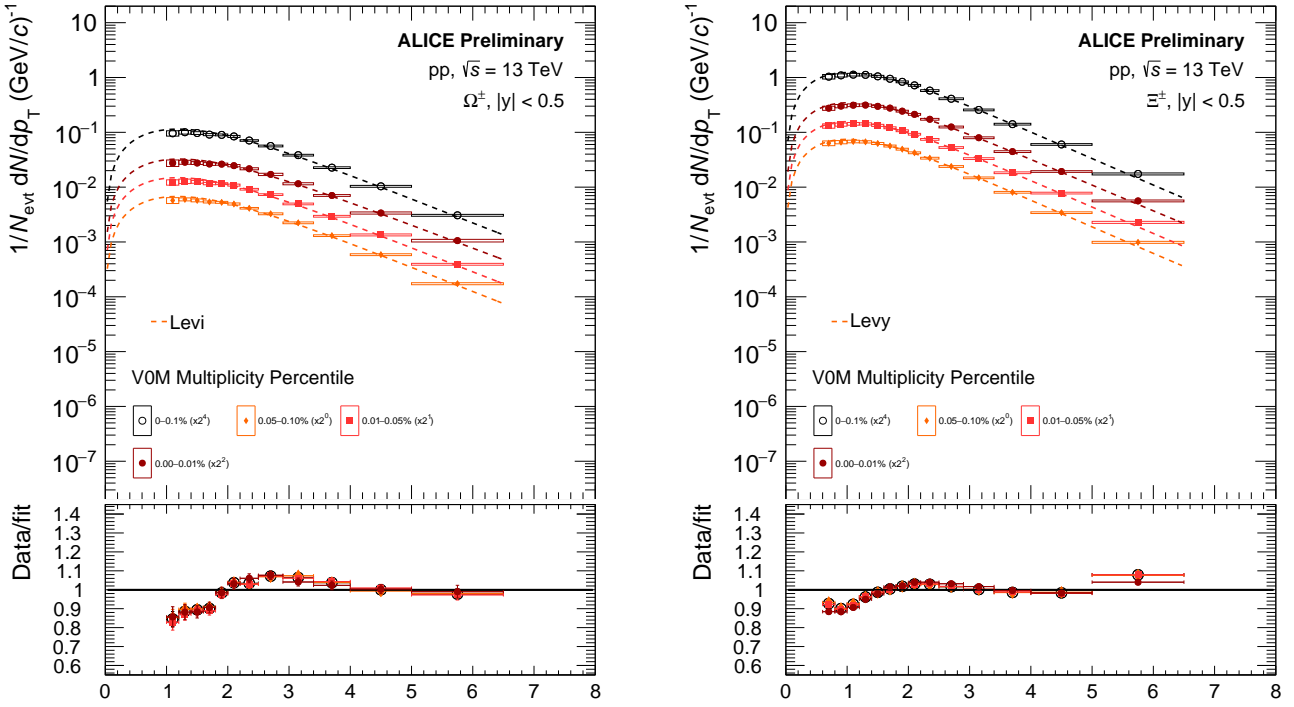
Ovisnost broja proizvedenih čestica o transversalnoj količini gibanja je prikazana na slici 7.7. Vidljivo je da s povećanjem multipliciteta broj proizvedenih hiperona raste, s time da je sve veći broj proizvedenih hiperona s višom transversalnom količinom gibanja. Ovi rezultati su uspoređeni s objavljenim rezultatima kako bi se provjerila valjanost analize i pokazano je da se većina rezultata slaže unutar jedne statističke devijacije.



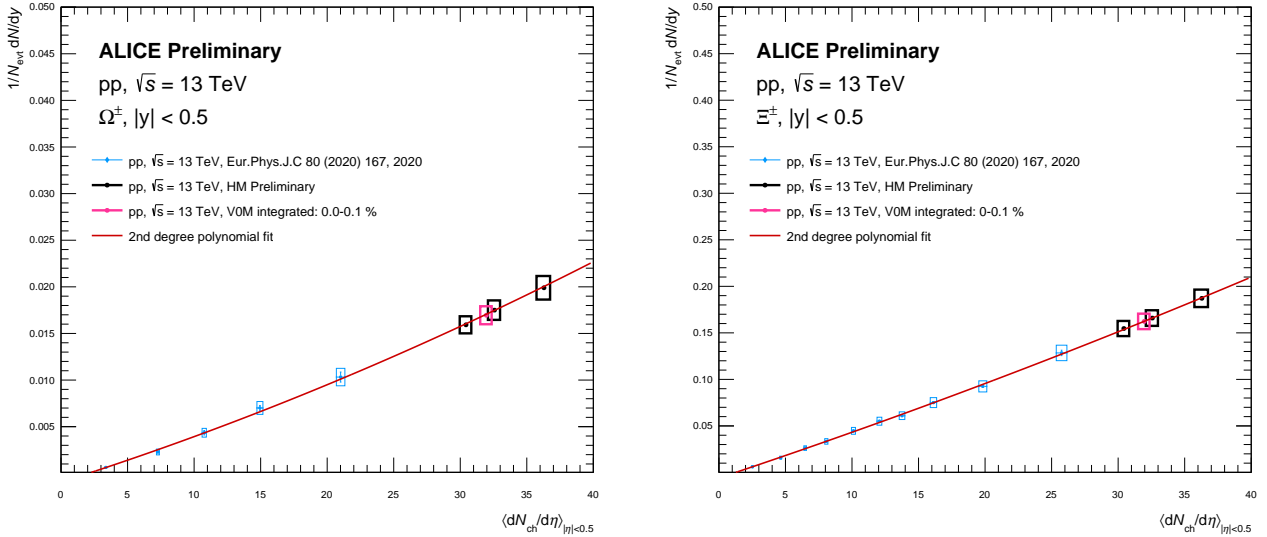
Slika 7.7: Ovisnost broja proizvedenih  $\Omega^- + \bar{\Omega}^+$  i  $\Xi^- + \bar{\Xi}^+$  o transversalnoj količini gibanja  $\Omega^- + \bar{\Omega}^+$  i  $\Xi^- + \bar{\Xi}^+$  za različite multiplicitete. Na donjim grafovima su prikazani omjeri naspram integriranog multipliciteta (0-100%). Na slikama su prikazane statističke greške.

Kako bi se odredio ukupan proizvedeni broj hiperona za određeni multiplicitet, na spektre je prilagođena Levy-Tsallis funkcija, čijom se integracijom dobije ukupan broj proizvedenih hiperona po događaju (slika 7.8). Pri prilagodbi, provjereno je da vrijedi  $\chi^2/ndf \leq 2$  za sve vrijednosti multipliciteta.

Integriranjem preko cijelog područja transversalnog impulsa dobiven je broj proizvedenih hiperona po sudaru u ovisnosti o multiplicitetu. Prikazan je zajedno s već objavljenim rezultatima za proton-proton sudare pri 13 TeV-a na slici 7.9. Vidljivo je slaganje s objavljenim rezultatima te da se broj proizvedenih hiperona povećava s porastom multipliciteta. Na rezultate je napravljena prilagodba polinoma drugog reda, koja ukazuje na nelinearnu ovisnost među proizvodnjom hiperona i multipliciteta.

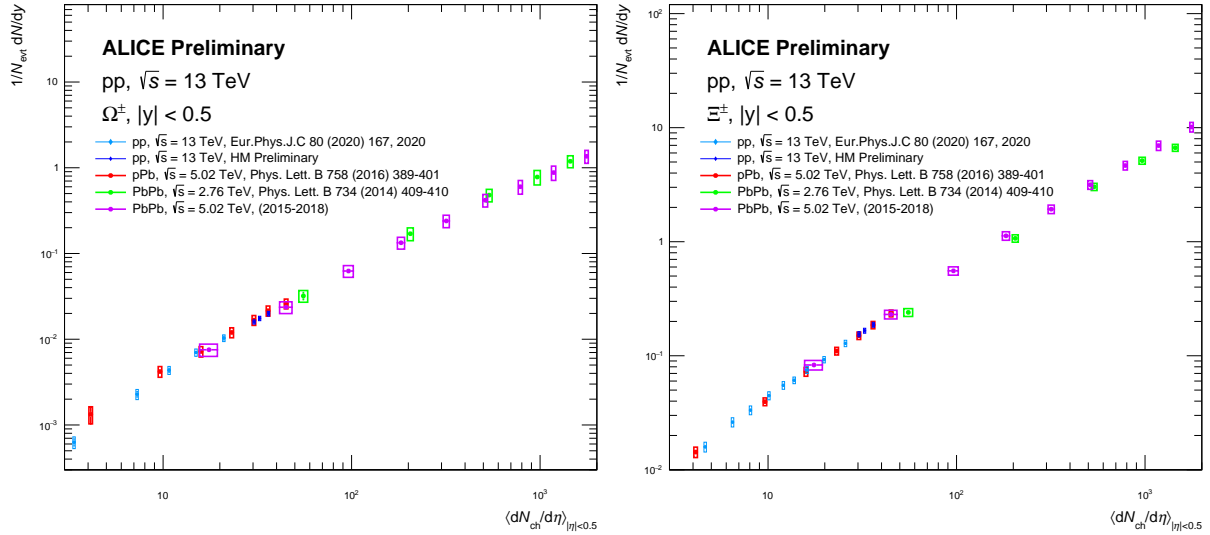


Slika 7.8: Spektri transverzalne količine gibanja za  $\Omega^- + \bar{\Omega}^+$  i  $\Xi^- + \bar{\Xi}^+$  s prilagođenim Levy-Tsallis distribucijama. U donjim grafovima je omjer prilagođene funkcije i podataka. Statističke greške su prikazane linijama dok su sistemske greške prikazane pravokutnicima.



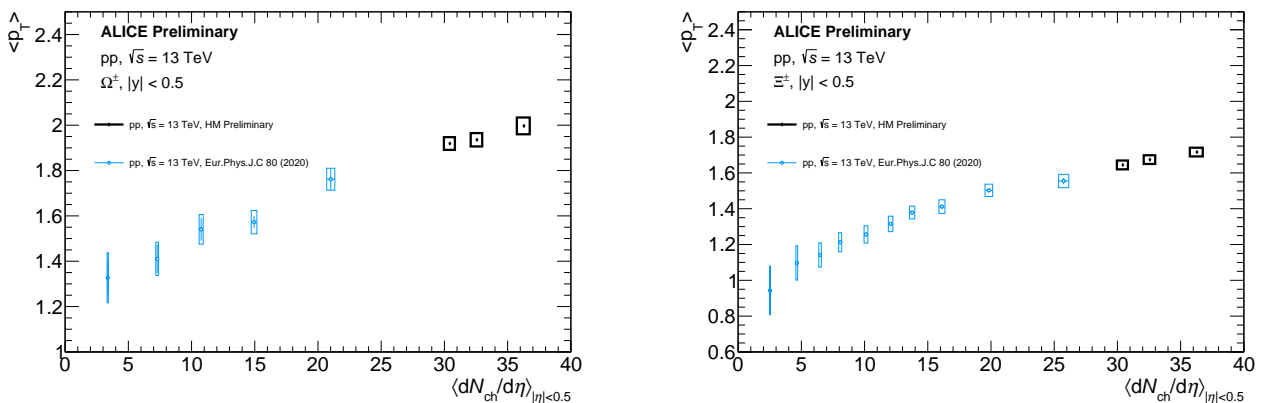
Slika 7.9: Integrirani broj proizvedenih hiperona  $\Omega^- + \bar{\Omega}^+$  i  $\Xi^- + \bar{\Xi}^+$  u ovisnosti o multiplicitetu. Pravokutnici predstavljaju sistemske greške dok su statističke prikazane linijama.

Usporedba je napravljena i s rezultatima dobivenim iz sudara proton-olovo i olovo-olovo, uz različite početne energije (slika 7.10). Vidljivo je slaganje između rezultata dobivenih ovom analizom, unutar jedne sistematske greške s rezultatima iz pPb, i rezultata za različite sustave. Može se zaključiti kako broj proizvedenih hiperona ne ovisi o početnoj energiji sudara ili tipu čestica koje sudaramo, već o konačnom multiplicitetu događaja.



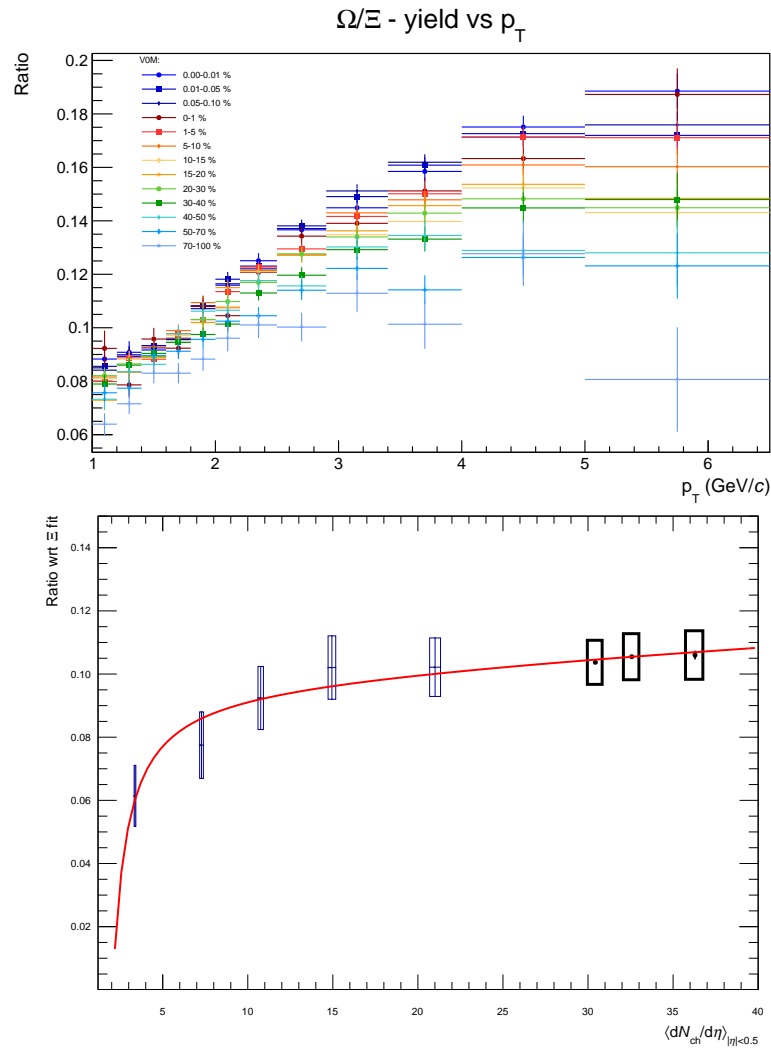
Slika 7.10: Integrirani broj proizvedenih hiperona  $\Omega^- + \bar{\Omega}^+$  i  $\Xi^- + \bar{\Xi}^+$  u ovisnosti o multiplicitetu za različite sustave: pp, pPb and PbPb.

Prosječna transverzalna količina gibanja je prikazana na slici 7.11. Pri sudarima viših multipliciteta, prosječna transverzalna količina gibanja čestica raste. Rezultati prate rastući trend dobivenih u prijašnjim istraživanjima, te su korisni pri razvoju i testiranju MC modela, koje koristimo za simulaciju sudara.



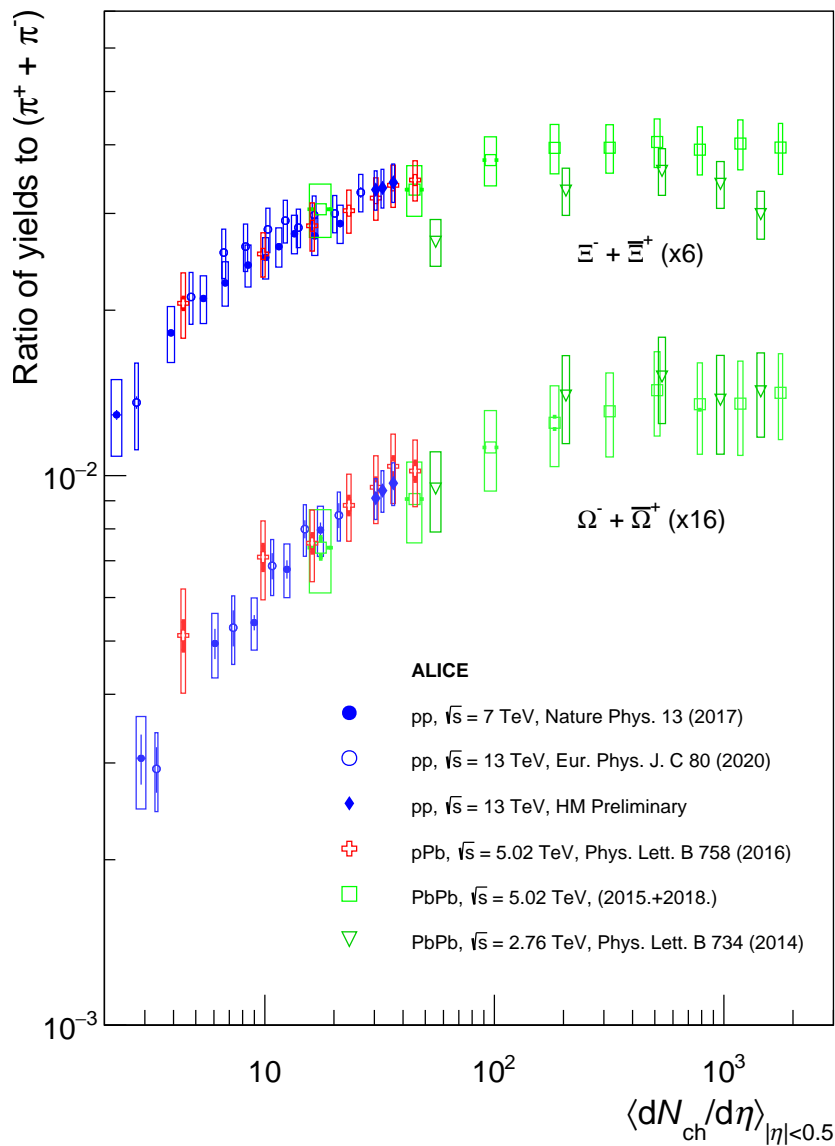
Slika 7.11: Prosječna transverzalna količina gibanja za  $\Omega^- + \bar{\Omega}^+$  i  $\Xi^- + \bar{\Xi}^+$ . Pravokutnici su sistematske greške.

Kako bi se istražio fenomen povećanja stranosti, razmatra se omjer između rezultata dobivenih za Omega i Ksi čestice. Prvo je napravljen omjer njihovih spektara transversalne količine gibanja, te nakon toga omjer integriranog broja proizvedenih čestica (slika 7.12). Vidljivo je da s porastom multipliciteta, omjer spektara raste s porastom multipliciteta. No, vrijednost omjera vrlo polako raste, uz veliku sistematsku grešku te nije moguće donijeti siguran zaključak. Također, iz omjera integriranog broja proizvedenih čestica se vidi kako taj omjer ne raste više strmo kao za manje multiplicitete već usporava, uz mogućnost zasićenja. Trenutni rezultati imaju prevelike greške, ali je ovo nešto vrijedno daljnjeg istraživanja.



Slika 7.12: Omjer spektara transversalnih količina gibanja za  $\Omega$  i  $\Xi$  (gore) za različite vrijednosti multipliciteta. Omjer integriranog broja proizvedenih čestica za  $\Omega$  i  $\Xi$  (dolje) u ovisnosti o multiplicitetu.

Omjer proizvedenih hiperona i piona je prikazan na slici 7.13. Vidljivo je slaganje između rezultata dobivenih ovom analizom i ostalih objavljenih rezultata, dobivenih pri različitim energijama i različitim tipovima sudara. Slaganje rezultata potvrđuje da povećanje stranosti ne ovisi o energiji sudara i o tipu čestica koje sudaramo već o konačnom multiplicitetu sudara. Time se indicira da je za proizvodnju stranosti odgovoran isti mehanizam. Predviđanje moguće saturacije za sudare protona nije vidljivo za područje multipliciteta promatrano u ovom radu, ali nije u potpunosti isključeno za sudare većih multipliciteta.



Slika 7.13: Omjer proizvedenih  $\Xi$  i  $\Omega$  naspram piona za različite tipove sudara.

## Zaključak

Ovim istraživanjem određeno je koliko se Omega i Ksi hiperona proizvodi u proton-proton sudarima na energijama centra mase 13 TeV-a s obzirom na multiplicitet događaja i transverzalnu količinu gibanja hiperona. Analiza je izvršena na još neobrađenim podacima s ALICE detektora prikupljenima kroz period od tri godine 2016.- 2018. Istraživanje se nastavlja na prijašnja istraživanja na nižim multiplicitetima te su rezultati na visokim multiplicitetima usporedivi s proton-olovo i perifernim olovo-olovo sudarima.

Rezultati dobiveni za spektre transverzalne količine gibanja su u skladu s očekivanjima: za viši multiplicitet, proizveden je veći broj hiperona, uz povećanje relativnog broja proizvedenih hiperona s većom transverzalnom količinom gibanja.

Nakon prilagodbe Levy-Tsallis funkcije na spektre, određen je integrirani broj proizvedenih hiperona u ovisnosti o multiplicitetu. Rezultati prate rastući trend s povećanjem multipliciteta, koji je u slaganju s rezultatima iz drugih tipova sudara. Rast broja proizvedenih hiperona je bolje opisan polinomom drugog stupnja, nego linearnom funkcijom, što ukazuje na nelinearnu ovisnost proizvodnje hiperona o multiplicitetu. Usporedbom s drugim tipovima sudara, kao što su proton-olovo i olovo-olovo, vidljivo je slaganje unutar jedne sistematske greške. Ovaj rezultat upućuje na to da je proizvodnja hiperona neovisna o početnoj energiji i tipu sudara, već ovisi o konačnom multiplicitetu sudara.

Prosječna transverzalna količina gibanja prati rastući trend s povećanjem multipliciteta. Viši multiplicitet odgovara centralnijim sudarima, u kojima dolazi do većeg broja tvrdih procesa u kojima nastaju visoko energetske čestice. Dobiveni rezultati će pomoći pri razvitku boljih simulacijskih modela koji koriste perturbativnu kromodinamiku za simulaciju tvrdih procesa i fenomenološke metode za meke procese. Modeli s godinama napreduju, ali su još daleko od stvarnosti, te će ovi rezultati za Omega i Ksi hiperone pridonijeti njihovu razvitku.

Usporedbom rezultata dobivenih za Omega i Ksi hiperone vidljiva je ovisnost njihove proizvodnje o multiplicitetu. S porastom multipliciteta, omjer proizvedenih Omega i Ksi hiperona polagano raste, što je u skladu s fenomenom povećanja stranosti. Zbog velikih grešaka pri rađanju omjera, ne može se donijeti siguran zaključak. Omjerom integriranog broja proizvedenih Omega i Ksi hiperona se vidi da se nagib rastućeg trenda s nižih multipliciteta smanjuje na višim multiplicitetima. Vidi se i moguće zasićenje, što nije predviđeno s fenomenom povećanja stranosti. I u ovom slučaju su greške omjera prevelike za donijeti zaključak, ali ovo je sigurno nešto vrijedno promatranja u budućim istraživanjima.

Omjeri proizvedenih hiperona i nabijenih piona jasno ukazuju na povećanu proizvodnju hiperona naspram čestica koje ne sadrže strani kvark. Pri nižim multiplicitetima, ovaj fenomen je



izraženiji dok za područje olovo-olovo sudara dolazi do saturacije. Rezultati iz ovog istraživanja ukazuju na to da proizvodnja hiperona ovisi o konačnom multiplicitetu, a ne o energiji sudara i česticama koje sudaramo. Za proton-proton sudare u području visokog multipliciteta trend povećanja stranosti se nastavlja kao i za ostale tipove sudara. Time se opovrgnula pretpostavka da će doći do saturacije u proizvodnji zbog male veličine sustava u ovom području multipliciteta. Rezultati potvrđuju pretpostavku da je za proizvodnju hiperona u sudarima različitih tipova čestica odgovaran isti mehanizam. Dobiveni rezultati nisu dovoljni da bi se potvrdila ili opovrgnula teorija postojanja kvarkovsko-gluonske plazme u proton-proton sudarima, ali nas dovodi korak bliže konačnom odgovoru.

# References

- [1] The ALICE Collaboration. “Multiplicity dependence of (multi-)strange hadron production in proton-proton collisions at  $\sqrt{s} = 13$  TeV”. In: *Eur. Phys. J. C* (2020). DOI: 10.1140/epjc/s10052-020-7673-8.
- [2] The ALICE Collaboration. “Enhanced production of multi-strange hadrons in high-multiplicity proton-proton collisions”. In: *Nature Physics* (2017). DOI: 10.1038/nphys4111.
- [3] URL: [https://en.wikipedia.org/wiki/File:Standard\\_Model\\_of\\_Elementary\\_Particles.svg](https://en.wikipedia.org/wiki/File:Standard_Model_of_Elementary_Particles.svg).
- [4] *The Nobel Prize in Physics 1965*. URL: <https://www.nobelprize.org/prizes/physics/1965/summary/>.
- [5] *The Nobel Prize in Physics 1979*. URL: <https://www.nobelprize.org/prizes/physics/1979/summary/>.
- [6] *The Nobel Prize in Physics 1984*. URL: <https://www.nobelprize.org/prizes/physics/1984/summary/>.
- [7] M. Gell-Mann. “A schematic model of baryons and mesons”. In: *Physics Letters* (1964). DOI: 10.1016/S0031-9163(64)92001-3.
- [8] G. Zweig. *An SU(3) Model for Strong Interaction Symmetry and its Breaking*. URL: CERNReportNo.8182/TH.401.
- [9] *The Nobel Prize in Physics 2004*. URL: <https://www.nobelprize.org/prizes/physics/2004/summary/>.
- [10] Adrian Cho. “Higgs Boson Makes Its Debut After Decades-Long Search”. In: *Science* (2012).
- [11] M. Y. Han and Y. Nambu. “Three-Triplet Model with Double SU(3) Symmetry”. In: *Phys. Rev.* (1965). DOI: 10.1103/PhysRev.139.B1006.
- [12] O. W. Greenberg. “Spin and Unitary-Spin Independence in a Paraquark Model of Baryons and Mesons”. In: *Phys. Rev. Lett.* (1964). DOI: 10.1103/PhysRevLett.13.598.
- [13] Particle Data Group. “Review of Particle Physics”. In: *PTEP* (2022). DOI: 10.1093/ptep/ptac097.
- [14] Antonin Maire and Julien Charles Hamon. “Phase transition to QGP matter : confined vs deconfined matter”. 2015. URL: <https://cds.cern.ch/record/2026889>.

- [15] Ulrich Heinz and Maurice Jacob. *Evidence for a New State of Matter: An Assessment of the Results from the CERN Lead Beam Programme*. 2000. arXiv: nucl-th/0002042 [nucl-th].
- [16] Antonin Maire. “Two views on the Bjorken scenario for ultra-relativistic heavy-ion collisions”. 2011. URL: <https://cds.cern.ch/record/2030270>.
- [17] Antonin Maire. “Phase diagram of QCD matter : Quark-Gluon Plasma”. General Photo. 2015. URL: <https://cds.cern.ch/record/2025215>.
- [18] Takafumi Niida and Yasuo Miake. *Signatures of QGP at RHIC and the LHC*. 2021. arXiv: 2104.11406 [nucl-ex].
- [19] The LHCb Collaboration. “Centrality determination in heavy-ion collisions with the LHCb detector”. In: *JINST* (2022). DOI: 10.1088/1748-0221/17/05/P05009.
- [20] *The Nobel Prize in Physics 1969*. URL: <https://www.nobelprize.org/prizes/physics/1969/summary/>.
- [21] E. D. Bloom et al. “High-Energy Inelastic e-p Scattering at 6° and 10°”. In: *Phys. Rev. Lett.* (1969). DOI: 10.1103/PhysRevLett.23.930.
- [22] M. Breidenbach et al. “Observed Behavior of Highly Inelastic Electron-Proton Scattering”. In: *Phys. Rev. Lett.* (1969). DOI: 10.1103/PhysRevLett.23.935.
- [23] URL: <https://commons.wikimedia.org/w/index.php?curid=3245752>.
- [24] Antonin Maire. “Production des baryons multi-étranges au LHC dans les collisions proton-proton avec l’expérience ALICE”. 2011. URL: <https://cds.cern.ch/record/1490315>.
- [25] Johann Rafelski and Berndt Müller. “Strangeness Production in the Quark-Gluon Plasma”. In: *Phys. Rev. Lett.* (1982). DOI: 10.1103/PhysRevLett.48.1066.
- [26] P Koch, B Müller, and J Rafelski. “Strangeness in relativistic heavy ion collisions”. In: *Physics Reports* (1986). DOI: [https://doi.org/10.1016/0370-1573\(86\)90096-7](https://doi.org/10.1016/0370-1573(86)90096-7).
- [27] C. Blume and C. Markert. “Strange hadron production in heavy ion collisions from SPS to RHIC”. In: *Progress in Particle and Nuclear Physics* (2011). DOI: 10.1016/j.pnpnp.2011.05.001.
- [28] E. Andersen et al. “Enhancement of central Lambda, Xi and Omega yields in Pb - Pb collisions at 158 A-GeV/c”. In: *Phys. Lett. B* (1998). DOI: 10.1016/S0370-2693(98)00689-3.
- [29] Peter Koch, Berndt Müller, and Johann Rafelski. “From strangeness enhancement to quark-gluon plasma discovery”. In: *IJMPA* (2017). DOI: 10.1142/s0217751x17300241.
- [30] The ALICE Collaboration. “Multi-strange baryon production at mid-rapidity in Pb-Pb collisions at  $\sqrt{s_{NN}} = 2.76$  TeV”. In: *Phys. Lett. B* (2014). DOI: 10.1016/j.physletb.2013.11.048.
- [31] The ALICE Collaboration. “Multiplicity dependence of pion, kaon, proton and lambda production in p-Pb collisions at  $\sqrt{s_{NN}} = 5.02$  TeV”. In: *Phys. Lett. B* (2014). DOI: 10.1016/j.physletb.2013.11.020.

- [32] The ALICE Collaboration. *Multi-strange baryon production in p-Pb collisions at  $\sqrt{s_{NN}} = 5.02 \text{ TeV}$* . 2016. arXiv: 1512.07227 [nucl-ex].
- [33] J. Cleymans et al. “Statistical model predictions for particle ratios at  $\sqrt{s_{NN}} = 5.5 \text{ TeV}$ ”. In: *Phys. Rev. C* (2006). DOI: 10.1103/physrevc.74.034903.
- [34] A. Andronic, P. Braun-Munzinger, and J. Stachel. “Thermal hadron production in relativistic nuclear collisions: the hadron mass spectrum, the horn, and the QCD phase transition”. In: *Phys. Lett. B* (2009). DOI: 10.48550/arXiv.0812.1186.
- [35] R. Hagedorn and J. Ranft. “Statistical thermodynamics of strong interactions at high-energies. 2. Momentum spectra of particles produced in pp-collisions”. In: *Nuovo Cim. Suppl.* (1968).
- [36] F. Becattini and U. Heinz. “Thermal hadron production in pp and p anit-p collisions”. In: *Zeitschrift for Physik C Particles and Fields* (1997). DOI: 10.1007/s002880050551.
- [37] K. Redlich and A. Tounsi. “Strangeness enhancement and energy dependence in heavy ion collisions”. In: *Eur. Phys. J. C* (2002). DOI: 10.1007/s10052-002-0983-1.
- [38] F Becattini and J Manninen. “Strangeness production from SPS to LHC”. In: *J. Phys. G: Nucl. Part. Phys.* (2008). DOI: 10.1088/0954-3899/35/10/104013.
- [39] URL: <https://home.cern/resources/image/cern/views-cern-images-gallery>.
- [40] Esma Mobs. “The CERN accelerator complex - August 2018. Complexe des accélérateurs du CERN - Août 2018”. In: (2018). URL: <https://cds.cern.ch/record/2636343>.
- [41] AC Team. “Diagram of an LHC dipole magnet. Schéma d’un aimant dipôle du LHC”. 1999. URL: <https://cds.cern.ch/record/40524>.
- [42] Arturo Tauro. “ALICE Schematics”. 2017. URL: <https://cds.cern.ch/record/2263642>.
- [43] The ALICE Collaboration. *The ALICE experiment – A journey through QCD*. 2022. arXiv: 2211.04384 [nucl-ex].
- [44] Antonin Maire. “ALICE TPC sectors and pad rows”. 2011. URL: <https://cds.cern.ch/record/2030274>.
- [45] Christian Lippmann. “Particle identification”. In: *Nucl. Instrum. Methods Phys. Res., A* (2011). DOI: 10.1016/j.nima.2011.03.009.
- [46] F. Carena et al. “The ALICE data acquisition system”. In: *Nucl. Instrum. Methods Phys. Res., A* (2014). DOI: <https://doi.org/10.1016/j.nima.2013.12.015>.
- [47] The ALICE Collaboration. In: *Journal of Instrumentation* (2008). DOI: 10.1088/1748-0221/3/08/S08002.
- [48] Antonin Maire. “Track reconstruction principle in ALICE for LHC run I and run II. Principes de reconstruction de traces dans ALICE pour les runs I et II du LHC”. 2011. URL: <https://cds.cern.ch/record/1984041>.

- [49] R. Schotter and G. Skorodumovs. “Testing CPT theorem via the mass differences between anti-hyperons and hyperons with pp data of LHC run II”. URL: <https://alice-notes.web.cern.ch/node/1331>.
- [50] Antonin Maire. “Four types of cascade decays for multi-strange baryons (charged Xi and Omega)”. 2011. URL: <https://cds.cern.ch/record/2030269>.
- [51] L. Bianchi, D Chinellato, and R. Derradi de Souza. “Strangeness production as a function of the charged particle multiplicity in pp collisions at  $\sqrt{s} = 7 \text{ TeV}$ ”. URL: <https://alice-notes.web.cern.ch/node/429>.
- [52] F. Fionda. “Study of strangeness production as a function of the charged particle multiplicity in pp collisions at  $\sqrt{s} = 13 \text{ TeV}$ ”. URL: <https://alice-notes.web.cern.ch/node/478>.
- [53] Antonin Maire. “Topological selections for V0 (K0s, Lambda) and Cascade (Xi, Omega) reconstruction in ALICE”. 2011. URL: <https://cds.cern.ch/record/2030272>.
- [54] Roger Barlow. *Systematic Errors: facts and fictions*. 2002. arXiv: hep-ex/0207026 [hep-ex].
- [55] Prabhakar Palni and Paolo Bartalini. “Updated results of minimum bias pseudorapidity density distribution in pp collisions at  $\sqrt{s} = 13 \text{ TeV}$ ”. URL: <https://alice-notes.web.cern.ch/node/823>.
- [56] The ALICE Collaboration. “Multiplicity dependence of  $\pi$ , K, and p production in pp collisions at 13 TeV”. In: *Eur. Phys. J. C* (2020). DOI: <https://doi.org/10.1140/epjc/s10052-020-8125-1>.
- [57] Navneet Kumar. “ $\pi$ , K and p production in high multiplicity pp collisions at  $\sqrt{s} = 13 \text{ TeV}$  using TPC and TOF”. URL: <https://alice-notes.web.cern.ch/node/1477>.
- [58] The ALICE Collaboration. “Multi-strange baryon production in pPb collisions at  $\sqrt{s_{NN}} = 5.02 \text{ TeV}$ ”. In: *Phys. Lett. B* (2016). DOI: <https://doi.org/10.1016/j.physletb.2016.05.027>.
- [59] The ALICE Collaboration. “Multi-strange baryon production at mid-rapidity in Pb–Pb collisions at  $\sqrt{s_{NN}} = 2.76 \text{ TeV}$ ”. In: *Phys. Lett. B* (2014). DOI: <https://doi.org/10.1016/j.physletb.2013.11.048>.
- [60] L. Bianchi, A. Balbino, and M. Barlou. “Strange and multi-strange hadron production in Pb-Pb collisions 5.02 TeV”. URL: <https://alice-notes.web.cern.ch/node/1384>.

## Supervisor information

Mirko Planinić is a full Professor at the Physics department of the Faculty of Science University of Zagreb. His main research interests comprise experimental particle and nuclear physics. He is a member of the ALICE collaboration at CERN. He is a co-author of more than 700 publications (WoSCC), with more than 30000 citations, H-index 105. He has mentored 3 defended Ph.D. theses, with 1 additional underway, as well as more than 15 diploma theses. He lead 3 grants: „Demystifying Two Particle Correlations in pp collisions with the upgraded Time Projection Chamber”, funded by the Croatian National Science Foundation 2018, „Study of the momentum correlations in high energy collisions using event structure criteria and ALICE detector at LHC”, funded by the Unity through Knowledge Fund 2013 and „Study of hadronic systems using relativistic projectiles” by the Ministry of Science in Croatia 2011, and participated in others. He is the co-founder of a spin-off company (Picologic) for the production of multi-channel floating picoammeters that is selling precise current measuring devices all around the world. In 2013, he was awarded the „Brdo” award by the students for the best lecturer at the Department of Physics of the University of Zagreb. He is now a Dean of the Faculty of Science University of Zagreb.

# Curriculum vitae

Born on January 19th, 1996 in Vinkovci, David Karatović lived for 18 years in Stari Jankovci. In that time, he attended elementary school Stari Jankovci and after that M. A. Reljkovića high school in Vinkovci. In 2014, he enrolled in physics studies at the Physics Department of the Faculty of Science at the University of Zagreb, which he graduated in 2019. His master thesis was done under the guidance of assist. prof. Nikola Poljak and titled: Development of a test setup for the upgrade of the Time Projection Chamber. The master thesis conducted a research of GEMs for allowed distanced between the foils and the rest of the construction in order to avoid sparking when high voltage is applied. He began his work in 2019, as an assistant at the Department of Physics and enrolled in a postgraduate course in Elementary Particle Physics. During his employment, 2019-2024, he was working on data analysis as a part of a PhD thesis topic in the ALICE Collaboration and as a teaching assistant at different courses: General Physics 1-4 (Mechanics, Electrodynamics, Waves and oscillations, Thermodynamics), Fundamentals of Physics 3-4, Physics 1-2, Electronics lab, Physics lab. From 2022, he is a committee member in physics state competitions, where he is grading and examining experimental elementary school student projects. In the time of writing this thesis, he has published 178 scientific papers as an author or co-author.